

UNIVERSITE DU QUEBEC EN ABITIBI-TEMISCAMINGUE

IMAGERIE INTÉGRÉE PAR INVERSION GÉOPHYSIQUE 3D, EXTRACTION  
DE CARACTÉRISTIQUE MULTIVARIÉE ET SÉLECTION DE  
CARACTÉRISTIQUE SPECTRALE

THESE  
PRESENTEE  
COMME EXIGENCE PARTIELLE  
DU DOCTORAT EN SCIENCES DE L'ENVIRONNEMENT

PAR  
BAHMAN ABBASSI

OCTOBRE 2018



# BIBLIOTHÈQUE

Cégep de l'Abitibi-Témiscamingue  
Université du Québec en Abitibi-Témiscamingue

## **Mise en garde**

La bibliothèque du Cégep de l'Abitibi-Témiscamingue et de l'Université du Québec en Abitibi-Témiscamingue a obtenu l'autorisation de l'auteur de ce document afin de diffuser, dans un but non lucratif, une copie de son œuvre dans Depositum, site d'archives numériques, gratuit et accessible à tous.

L'auteur conserve néanmoins ses droits de propriété intellectuelle, dont son droit d'auteur, sur cette œuvre. Il est donc interdit de reproduire ou de publier en totalité ou en partie ce document sans l'autorisation de l'auteur.

## **Warning**

The library of the Cégep de l'Abitibi-Témiscamingue and the Université du Québec en Abitibi-Témiscamingue obtained the permission of the author to use a copy of this document for non-profit purposes in order to put it in the open archives Depositum, which is free and accessible to all.

The author retains ownership of the copyright on this document. Neither the whole document, nor substantial extracts from it, may be printed or otherwise reproduced without the author's permission.

UNIVERSITE DU QUEBEC EN ABITIBI-TEMISCAMINGUE

INTEGRATED IMAGING THROUGH 3D GEOPHYSICAL INVERSION,  
MULTIVARIATE FEATURE EXTRACTION, AND SPECTRAL FEATURE  
SELECTION

THESIS PRESENTED IN PARTIAL FULFILLMENT OF THE REQUIREMENTS  
FOR THE DEGREE OF DOCTOR OF PHILOSOPHY IN ENVIRONMENTAL  
SCIENCES

BY  
BAHMAN ABBASSI

OCTOBER 2018

To my parents,  
Freydun Abbassi and Rouhangiz Rouhnavaz,  
And all my family and friends,  
Without whom none of my success would be possible



## ACKNOWLEDGMENTS

I would like to express my sincere gratitude to my supervisor Prof. Li Zhen Cheng for her patience, motivation, immense knowledge and her constant technical and financial support during this program. Besides my advisor, I would like to thank the rest of my thesis committee: Prof. Jean-Claude Mareschal, Prof. Claude Jaupart, Prof. Michel Jébrak, for their comments, encouragement, and also their insightful questions which incited me to widen my research from various angles.

This project was a collaboration between the Université du Québec en Abitibi-Témiscamingue and the University of Alberta, with industry partners Amarc Resources Ltd., Geotech Ltd., Gerald G. Carlson, and John A. Chapman. This study would not have been possible without the financial support from NSERC (Natural Sciences and Engineering Research Council of Canada) and FRQNT (Fonds de recherche, Nature et technologies du Québec).

Chapters II, III, IV and V of this doctoral thesis are research articles submitted or in preparation to be submitted to peer-reviewed journals. I was principally responsible for the content of these chapters, including data processing, modeling, and coding of algorithms.

Reviews significantly improved chapters II, III from following co-authors: Jeremy P. Richards, Juliane Hübert, Jean M. Legault, Mark Rebagliati and Ken Witherly. My sincere thanks also go to Prof. Jeremy P. Richards, Juliane Hübert, and Ken Witherly for their insightful teamwork, comments, and revisions of my papers. Mark Rebagliati from Amarc Resources Ltd. is particularly thanked for providing access to drillcore and geophysical data and reports; Jean M. Legault from Geotech Ltd. is acknowledged for the collection of the aeromagnetic data as well valuable discussions throughout the

project. I also coded and tested a variant of statistical and artificial intelligence algorithms in chapters IV and V under the supervision of Prof. Li Zhen Cheng.

I would like to express my deepest gratitude to all my family for supporting me and for their patience throughout all these years of academic research.

## TABLE OF CONTENTS

ACKNOWLEDGMENTS .....	iv
LIST OF FIGURES .....	x
LIST OF TABLES .....	xix
LIST OF SYMBOLS .....	xx
RÉSUMÉ .....	xxiii
ABSTRACT .....	xxv
CHAPTER I GENERAL INTRODUCTION .....	1
1.1 Motivation.....	1
1.2 Problem statement .....	2
1.3 Geophysical 3D modeling .....	4
1.4 Feature analysis .....	6
1.5 Research outline.....	7
CHAPTER II 3D COOPERATIVE INVERSION OF MAGNETIC AND DC/IP DATA OVER NEWTON EPITHERMAL AU-AG DEPOSIT IN BRITISH COLUMBIA, CANADA .....	8
Résumé.....	9
Abstract .....	11
2.1 Introduction.....	12
2.2 Geological setting .....	15
2.3 Physical properties.....	18

2.4	Geophysical data.....	21
2.5	3D Magnetization vector inversion .....	24
2.6	3D DC/IP inversion .....	27
2.7	3D cooperative inversion of magnetic and DC/IP data .....	30
2.8	Conclusion.....	42
2.9	Acknowledgments .....	44
CHAPTER III GEOPHYSICAL PROPERTIES OF AN EPITHERMAL AU-AG DEPOSIT IN BRITISH COLUMBIA, CANADA.....		45
	Résumé.....	46
	Abstract .....	47
3.1	Introduction.....	48
3.2	Geological setting .....	50
	3.2.1 Regional geology.....	50
	3.2.2 Deposit scale bedrock geology.....	52
3.3	Borehole geology and petrophysics.....	52
	3.3.1 3D lithology and hydrothermal alteration model .....	52
	3.3.2 Drillcores magnetic susceptibility and $\gamma$ -ray concentration .....	56
3.4	Geophysical datasets.....	58
3.5	Methods .....	61
	3.5.1 $\gamma$ -ray data interpretation .....	61
	3.5.2 3D unconstrained magnetization vector inversion.....	61
	3.5.3 3D IP-DC resistivity inversion.....	62
	3.5.4 3D cooperative magnetic-IP-DC resistivity inversion .....	63
3.6	Results .....	65

3.6.1 Regional unconstrained interpretation .....	65
3.6.2 Prospect scale unconstrained interpretation .....	67
3.6.3 Deposit scale constrained interpretation .....	71
3.7 Conclusion .....	77
3.8 Acknowledgments .....	79
CHAPTER IV FEATURES EXTRACTION FOR 3D INTERPRETATION OF MULTIPLE GEOPHYSICAL DATA THROUGH INDEPENDENT COMPONENT ANALYSIS .....	80
Résumé.....	81
Abstract .....	82
4.1 Introduction.....	83
4.2 Feature Extraction Methodology.....	85
4.3 Petrophysical Model: A Mixing System.....	90
4.4 Petrophysical Feature Extraction.....	95
4.5 Simulation of Geophysical System.....	98
4.5.1 3D Forward Modeling .....	98
4.5.2 3D Inversion .....	101
4.6 Post-Inversion Feature Extraction .....	103
4.7 Conclusion.....	105
4.8 Acknowledgments .....	106
CHAPTER V 3D SUPERVISED SPECTRAL FEATURE SUBSET SELECTION.....	107
Résumé.....	108
Abstract .....	110

5.1	Introduction.....	111
5.2	Theory and methods .....	113
5.2.1	Wavelet-ICA feature extraction .....	116
5.2.2	Supervised artificial neural networks (ANN).....	117
5.2.3	Spectral FSS optimization through GA optimization .....	122
5.3	Results .....	125
5.4	Conclusion .....	140
5.5	Acknowledgments .....	141
	CHAPTER VI GENERAL CONCLUSION.....	142
	APPENDIX A MATLAB PROGRAMS FOR 2D SFSS.....	145
	APPENDIX B 2D SPECTRAL FEATURE SELECTION: MATLAB CODE EVALUATION.....	185
	GENERAL REFERENCES .....	191

## LIST OF FIGURES

Figure	Page
2.1	Several large porphyry and epithermal deposits located in Stikinia terrain (ST) in central British Columbia. Other terranes are: Alexander terrane (AX); Bridge River terrane (BR); Caribo terrane (CAC); Cache Creek terrane (CC); Cadwallader terrane (CD); Coast Complex terrane (CX); Harrison terrane (HA); Kootenay Terrane (KO); Monashee (MO); Cratonal North America terrane (NA); Nisling terrane (NI); Post Accretionary Plutons (PAP); Quesnellia terrane (QN); Shuksan terrane (SH); Slide Mountain Terrane (SM); Wrangellia (WR). Modified from Massey et al. (2005). .... 15
2.2	Bedrock geology map at the deposit scale. Colored dots indicate drillhole locations with various total lengths (Pressacco, 2012; McClenaghan, 2013). The light gray parts are undefined regions due to the lack of borehole information in the periphery of the deposit. Contours indicate topography. .... 17
2.3	Boxplot demonstration of measured magnetic susceptibilities of different lithologies from the Newton deposit. Susceptibility axis is logarithmic. The lithologies with average susceptibility values are: monzonite (M, 0.00012 SI); quartz feldspar porphyry (QFP, 0.00012 SI); felsic volcanic rocks (FVR, 0.00017); sedimentary rocks (SR; 0.00017); diorite (D, 0.014 SI); mafic volcanic rocks (MVR, 0.009). .... 18
2.4	3D borehole models. (a) Borehole susceptibility model. (b) Au concentration model (b). Both models are sliced horizontally at the elevation of 1000 m. Bedrock geology is overlaid on both models. Black dots indicate the location of boreholes. .... 19
2.5	Magnetic data-sets. (a) Total magnetic field intensities on a regional scale. Data are draped on a shaded relief digital elevation model of the region. (b) Total magnetic field intensities on Newton deposit scale. Black lines outline the bedrock geology contacts. .... 22

2.6	DC/IP data-set. Plan maps are showing the locations of DC/IP electrodes covering the halo of hydrothermal alteration over the Newton area. (a) Measured apparent resistivities. (b) Measured apparent chargeabilities. Data are shown for the dipolar length of 100 m and dipolar separation of $n = 4$ .	23
2.7	MVI models sliced at the elevation of 1000m. (a) First sharpening round. (b) Second sharpening round. (c) Third sharpening round. (d) Fourth sharpening round. Outline of Au mineralization is shown in the white contour. Bedrock geology is overlaid on all slices.	26
2.8	Preliminary inversion of DC/IP data over the Newton deposit. (a) Resistivity model sliced at elevation 1000 m. (b) Chargeability model sliced at elevation 1000 m. Outline of Au mineralization is shown in the white contour. Bedrock geology is overlaid on both slices.	29
2.9	Deposit scale DC/IP inversion sliced at the elevation of 1000 m. (a) Electrical resistivity model (contours indicate topography). (b) IP chargeability model compared to the borehole magnetic-highs (black contour). Outline of Au mineralization is shown in the white contour.	31
2.10	Susceptibilities of rock samples versus inverted chargeabilities and Au concentrations. (a) Anticorrelation between the susceptibilities and Au concentrations. (b) Correlation between the chargeabilities and susceptibilities. Low susceptibility/chargeability porphyritic intrusions (FIP) and felsic volcanic rocks (FVR) are divided from high susceptibility/chargeability mafic volcanic rocks (MVR) and dioritic intrusions (D). <i>CC</i> indicates correlation coefficient.	32
2.11	Indirect evidence of a link between the underlying physical properties of rocks. (a) Forward magnetic response of the IP-driven susceptibility model. (b) Forward magnetic response of the MVI susceptibility model (contours) overlaid on the observed residual magnetic field. (c) Forward magnetic response of the borehole susceptibility model. All magnetic field responses are reduced to the magnetic pole for centralization of the anomaly picks.	34
2.12	Cooperative magnetic-DC/IP inversion workflow.	35



2.13	A horizontal slice of the calculated weight model. ....	37
2.14	Cooperative inversion results with different weighting scenarios. (a, b and c) Cooperative susceptibilities with uniform weighting. (d, e and f) Cooperative susceptibilities with non-uniform weighting. The global weight ( $w$ ) is reduced from 0.1 to 0.001 in each scenario. Outline of Au mineralization is shown in the white contour. Bedrock geology is overlaid on both slices. ....	39
2.15	Evaluation of inverted susceptibilities. (a) Unconstrained MVI susceptibilities versus borehole susceptibilities. (b) Susceptibility model from non-uniform cooperative inversion ( $w = 0.01$ ) versus borehole susceptibilities. CC indicates correlation coefficient. ....	40
2.16	The 3D view of cooperative inversion results. The red wireframe indicates the high magnetic zone which confines a low magnetic mineralized zone within itself. The NHF cross-cuts the eastern portion of the low magnetic zone. ....	41
3.1	Several large porphyry and epithermal deposits located in Stikinia terrain (ST) in central British Columbia. Other terranes are: Alexander terrane (AX); Bridge River terrane (BR); Caribo terrane (CAC); Cache Creek terrane (CC); Cadwallader terrane (CD); Coast Complex terrane (CX); Harrison terrane (HA); Kootenay Terrane (KO); Monashee (MO); Cratonal North America terrane (NA); Nisling terrane (NI); Post Accretionary Plutons (PAP); Quesnellia terrane (QN); Shuksan terrane (SH); Slide Mountain Terrane (SM); Wrangellia (WR). Modified from Massey et al. (2005). ....	50
3.2	Regional geological features of Newton area modified after British Columbia Geological Survey Geoscience Map (mapplace.ca). Geology is draped on shaded relief topography. ....	51
3.3	Bedrock geology map at the deposit scale. Colored dots indicate drillhole locations with various total lengths. The light gray parts are undefined regions due to the lack of borehole information in the periphery of the deposit. Contours indicate topography. ....	53
3.4	Lithology and alteration models based on borehole data: (a) A cross-section of 3D lithology model along profile AA' in Figure 3.3 (5738800m N). (b) A cross-section of 3D alteration model along the same profile. The Newton Hill Fault (NHF) has	

	disrupted the continuity of all lithological units and offsets the mineralized zone. The gold mineralization correlates strongly with quartz-sericite alteration, predominantly in the felsic volcanic unit. ....	55
3.5	Magnetic susceptibilities of drillcores on profile AA'. High magnetic mafic volcanic rocks and dioritic intrusions are separated from other low magnetic rocks (felsic volcanic rocks and porphyritic intrusions). ....	56
3.6	Boxplot demonstration of measured magnetic susceptibilities and $\gamma$ -ray potassium (K) concentrations of different lithologies and alteration assemblages. Susceptibility axis is logarithmic. ....	58
3.7	Magnetic and IP-DC-resistivity datasets. All data are draped on a shaded relief digital elevation model (DEM) of the region: (a) Airborne total magnetic field intensities (TF) on a regional scale (GSC database). (b) Helicopter-borne total magnetic field intensities (TF) on deposit scale (Amarc dataset) together with locations of IP-DC-resistivity profiles. ....	60
3.8	Ternary images of airborne radiometric datasets (GSC): (a) Deposit scale RGB image of K-eTh-eU channels. White regions indicate the overlaps of all three elemental RGB channels. (b) Deposit scale RGB image of K/eTh-eTh/eU-eU/K channels. ....	61
3.9	Sharp regional MVI model after four IRI focused on the high and low magnetic susceptibility zones: (a) The 3D MVI susceptibility model on a plan view (draped on shaded relief topography). (b) The 3D MVI susceptibility model cross-cut on the profiles AA' 5738800m N. Directions of magnetization vectors are overlain on the cross-section AA'. Outlines of the hydrothermal zone and Newton deposit area are shown in the rectangles. ....	66
3.10	Prospect scale unconstrained MVI model after four IRI on Amarc datasets: (a) The 3D MVI susceptibility model on a plan view draped on shaded relief topography (Outline of Au-Ag-Cu mineralization is shown in the black contour). (b) The 3D MVI susceptibility model sliced at the elevations of 1000 m (the bedrock geology is overlapped). (c) The 3D MVI susceptibility model cross-cut on the profiles AA' at 5738800m N. Directions of magnetization vectors are overlain on the cross-section AA'. ....	68

- 3.11 Prospect scale inversion of IP-DC resistivity data over Newton area: (a) Plan view of the recovered resistivity model draped on a shaded relief topography model (Outline of Au-Ag-Cu mineralization is shown in the black contour). (b) Resistivity model sliced at elevation 1000 m (the bedrock geology is overlapped). (c) Resistivity model cross-cut on the profile AA' at 5738800m N (Outline of Au mineralization is shown in the black contour). ..... 69
- 3.12 Prospect scale inversion of IP-DC resistivity data over Newton area: (a) Plan view of the recovered chargeability model draped on a shaded relief topography model (Outline of Au-Ag-Cu mineralization is shown in the black contour). (b) Chargeability model sliced at elevation 1000 m (the bedrock geology is overlaid on the model). (c) Chargeability model cross-cut on the profile AA' at 5738800m N (Outline of Au mineralization is shown in the black contour). ..... 70
- 3.13 Deposit scale cooperative magnetic-IP-DC resistivity inversions sliced at the elevation of 1000 m: (a) Electrical resistivity model. (b) IP chargeability model. (c) Magnetic susceptibility model. The bedrock geology is overlaid on all models. The gray shaded zone is the outline of Au-Ag-Cu mineralization. .... 72
- 3.14 Petrophysical domains inferred from the integration of cooperatively inverted physical properties on the three physical properties' cross-plots. (a) A susceptibility-resistivity cross-plot with two distinct domains related to the high and low chargeability values. (b) A susceptibility-chargeability cross-plot with two distinct domains related to the high and low resistivity values. (c) A resistivity-chargeability cross-plot with two distinct domains related to the high and low susceptibility values. .... 74
- 3.15 Results of cooperative modeling compared with borehole information cross-cut on the profile AA' at 5738800m N in Figures 3.3: (a) Electrical resistivity model. (b) IP chargeability model. (c) Magnetic susceptibility model. (d) Integrated geological interpretation. .... 76
- 4.1 Workflow of geological model construction. The background geology consists of a three-layer stratum ( $L_{1a}$ ,  $L_{1b}$ ,  $L_{1c}$ ) intruded by a dyke ( $L_{1d}$ ). After several faulting and shear deformation, two

	alteration events ( $L_2$ and $L_3$ ) along with further deformations overprint the host geology. Noddy 3D geological and geophysical modeling package is used to build the geological model (Encom Technology Pty Ltd, 2009). .....	91
4.2	3D geological model: (a) 3D block view of all the background geological features. (b, c, d, and e) Background geological features ( $L1a$ , $L1b$ , $L1c$ ). (f) Two successive alteration events overlapped on the background geology ( $L2$ and $L3$ ). .....	92
4.3	Latent geological features (a) compared to physical properties produced in the petrophysical mixing system ( $\rho$ , $m$ , and $\chi$ in b, c, and d). Each physical property model provides partial information about the latent geological features. ....	94
4.4	Histograms of simulated physical properties with added non-gaussian geological noise: (a) Electrical Resistivity distribution. (b) IP chargeability distribution. (c) Magnetic susceptibility distribution. The solid curve indicates the cumulative distribution function. ....	95
4.5	Assessment of different source separation methods. (a, b and c) Principal component analysis. (d, e, f) Fast independent components by kurtosis maximization. (g, h, l) Fast independent components by negentropy maximization. All principal components (PCs) and independent components (kICs and nICs) are normalized from zero to one for consistency of visualization. ....	97
4.6	The geophysical responses of the mixed physical properties. (a) Total magnetic field intensities after reduction to the magnetic pole. (b) Apparent resistivities. (c) Apparent chargeabilities. DC/IP responses are presented on two NS and EW pseudo-sections as well as a horizontal slice corresponding to the dipolar separation of $n = 4$ . The arrows (black) indicate the location of simulated DC/IP electrodes. ....	100
4.7	Geophysical inversion results. (a), (b) and (c) are smooth inversion results. (d), (e) and (f) are sharper inversion results. (g), (h), (i) represent sharpest inversion results. ....	102
4.8	Post-inversion feature extraction through negentropy maximization (nICA) on different inversion scenarios. (a), (b) and (c) are independent components of smoothest physical properties.	

	(d), (e) and (f) are independent components of sharper physical properties. (g), (h), and (i) are independent components of sharpest physical properties. ....	104
5.1	Workflow of feature selection algorithm designed for geological interpretation. ....	115
5.2	2D Isotropic Mexican Hat mother wavelet. The left figure is the plan view of the right figure. ....	117
5.3	A simple perceptron maps a set of inputs ( $X_R$ ) onto a specific output ( $y$ ). ....	119
5.4	A multilayer perceptron (seven inputs and five neurons in the hidden layer) maps a set of inputs ( $X_R$ ) onto an appropriate output ( $y$ ). Defining a performance function ( $F$ ) during the back-propagation process updates the synaptic weights to make output closer to the specified target. ....	120
5.5	Linearly (left) and nonlinearly (right) separable two-object classification problems. ....	121
5.6	A general GA flowchart. Random change includes crossover and mutation that produces new population better fitted to the environmental landscape. ....	123
5.7	Location of boreholes in Newton epithermal system (a), versus density of borehole data points in 3D (b). Borehole data are available in places with densities more than one. In places without data points, conventional interpolations methods do not work properly. ....	126
5.8	Interpolation of geological targets with conventional methods. (a) Lithotype data (mafic/felsic). (b) Nearest-neighbor interpolation of lithotypes. (c) Kriging of lithotypes. (d) Au grade data. (e) Nearest-neighbor interpolation of Au grades. (f) Kriging of Au grades. ....	127
5.9	Three inverted physical property models used as inputs of the SFSS algorithm. ....	128
5.10	Three independent components (ICs) of the physical properties calculated through negentropy maximization. ....	129

5.11	Raw 3D spectral features produce by CWT with 5 scales in 24 directions ( $0^\circ, 15^\circ, 30^\circ, 45^\circ, 60^\circ, 75^\circ, 90^\circ, 105^\circ, 120^\circ, 135^\circ, 150^\circ, 165^\circ, 180^\circ, 195^\circ, 210^\circ, 225^\circ, 240^\circ, 255^\circ, 270^\circ, 285^\circ, 300^\circ, 315^\circ, 330^\circ, 345^\circ$ ). The extracted features are sliced at the elevation of 1000 m.....	130
5.12	Total 120 number of separated 3D spectral features after Fast-ICA dimensionality reduction for lithological feature selection. The extracted features are sliced at the elevation of 1000 m. ....	132
5.13	Evaluation of lithotype prediction for ANN and FSS algorithms. R-sq denotes the R-squared values. ....	133
5.14	The bi-objective error landscape of SFSS algorithm during lithotype estimation.....	134
5.15	Lithotype predictions: Results of 3D ANN predictiond (a) versus 3D SFSS predictions (b). SFSS resulted in the better reconstruction of lithotypes with less number of input spectral features ( $N_f = 78$ ). Results are sliced horizontally at the elevation of 1000 m. ....	134
5.16	Total 78 number of 3D selected features used for lithotype prediction. The selected features are sliced at the elevation of 1000 m.....	135
5.17	Total 108 number of separated 3D spectral features after Fast-ICA dimensionality reduction for Au grade feature selection. The extracted features are sliced at the elevation of 1000 m. ....	136
5.18	Evaluation of Au grade prediction for ANN and FSS algorithms. R-sq denotes the R-squared values. ....	137
5.19	The bi-objective error landscape of SFSS algorithm during Au grade estimation. ....	138
5.20	Au grade predictions: Results of 3D ANN predictions (a) versus 3D SFSS predictions (b). SFSS resulted in better reconstruction of Au grade distributions with less number of input spectral features ( $N_f$ ). Results are sliced horizontally at the elevation of 1000 m. The gray shaded zone is the outline of mineralization.....	138

5.21	Total 96 number of 3D selected features used for lithotype prediction. The selected features are sliced at the elevation of 1000 m.....	139
B.1	Simulation of a 2D imaging system containing several latent features (faces). The red traverse lines are indicating the sampled pixels that form the targets of the SFSS algorithm. ....	186
B.2	Three independent components (ICs) of the mixed image calculated from negentropy maximization of input mixed images. ....	186
B.3	240 raw spectral features produce by CWT with 20 scales in four directions ( $0^\circ$ , $90^\circ$ , $180^\circ$ , $270^\circ$ ). ....	187
B.4	120 separated spectral features after Fast-ICA dimensionality reduction.....	188
B.5	Evaluation of ANN and spectral learning algorithms in target prediction.....	189
B.6	The bi-objective error landscape of SFSS algorithm. ....	190

## LIST OF TABLES

Table	Page
3.1 Classified petrophysical domains based on inverted physical properties and their integrated interpretation. ....	75



## LIST OF SYMBOLS

$S_c$	calculated geophysical response
$P_j$	physical properties of subsurface
$f$	forward problem operator
$P_j^*$	approximated physical properties
$S_d$	measured signals (data)
$f^{-1}$	inverse problem operator
$\overset{\mathbf{1}}{J}_{Rem}$	remanent magnetization vector
$\overset{\mathbf{1}}{J}_{Ind}$	inductive magnetization vector
$\overset{\mathbf{1}}{H}_0$	earth's magnetic field vector
$\chi$	magnetic susceptibility
$\overset{\mathbf{1}}{J}_{Total}$	total magnetization vector
$\chi_{Total}$	total magnetic susceptibility
$m$	induced polarization chargeability
$\sigma_{DC}$	reference direct current electrical conductivity
$\sigma_{IP}$	perturbed subsurface induced polarization chargeability
$\phi$	electrical potential
$\rho$	electrical resistivity

$0 < k_1 < 1$	data constraint factor in robust inversion
$0 < k_2 < 1$	model constraint factor in robust inversion
CC	correlation coefficient
$\chi_{BH}$	borehole susceptibilities
$\chi_{MVI}$	modeled susceptibilities from magnetization vector inversion
$0 < w < 1$	global weight in cooperative magnetic inversion
$R_f$	vertical to horizontal flatness filter ratio in DC/IP inversion
$L_i$	latent geological features
$P_{Noise}$	non-gaussian geological noise on physical properties
$A = a_{ij}$	mixing matrix
$w_{ij}$	separation matrix
$D$	principle component analysis weight matrix
$Y_{PC}$	centered physical properties
$\tilde{L}^*$	least Gaussian independent components (approximated lithotypes)
$R$	ICA rotation matrix
$kurt$	kurtosis operator
$E(.)$	expected value
$H$	entropy
$p$	probability density

$neg$	negentropy operator
$G$	non-quadratic exponential function in negentropy maximization
$C_s$	2D continuous wavelet transform coefficients
$\psi(x, y)$	2D mother wavelet
$x_j$	neural network input vector
$w_j$	neural network weights
$y$	neural network output
$t$	neural network target
$E_{ANN}$	least mean square neural network objective function
$N$	number of neural network output samples (instance size)
$R$	number of neural network inputs.
$E_{Global}$	genetic algorithm global bi-objective cost function
$n_f$	number of features

## RÉSUMÉ

Il existe plusieurs défis techniques liés à la collecte de données, à la modélisation inverse et la fusion de modèles ainsi qu'aux interprétations intégrées en géophysique d'exploration minière. Dans cette étude de doctorat, de nouvelles méthodologies sont testées et évaluées pour l'interprétation intégrée 3D de plusieurs images géophysiques ciblant les gisements minéraux. La modélisation 3D inverse de multiples données géophysiques, de statistiques multivariées et de méthodes d'apprentissage automatique est utilisée pour développer une méthodologie robuste d'interprétation intégrée 3D. Une inversion coopérative de plusieurs données géophysiques est proposée pour l'imagerie 3D d'un gisement épithermal Au-Ag en Colombie-Britannique (Canada). Les données géophysiques multiples sont interprétées et évaluées par des observations pétrophysiques, géochimiques et géologiques de forage afin d'améliorer notre compréhension du système épithermal de Newton en termes de signatures géophysiques. L'interprétation intégrée a identifié quatre domaines pétrophysiques basés sur les trois propriétés physiques inversées en coopération, y compris la résistivité électrique, la chargeabilité PP et la susceptibilité magnétique. Nous avons également développé un outil statistique 3D pour extraire des informations géologiques à partir de modèles de propriétés physiques inversés basés sur l'analyse de composants indépendants à travers la maximisation de la néguentropie. Une interprétation automatisée de plusieurs images géophysiques 3D est également présentée par un algorithme de sélection de sous-ensembles spectraux hybrides (SSSH), basé sur un algorithme d'intelligence artificielle supervisée généralisée qui cherche à reconstruire des cibles géologiques limitées à partir d'images géophysiques 3D. Le présent algorithme SSSH prend les caractéristiques spectrales extraites de la décomposition en ondelettes des composants indépendants des propriétés physiques et essaye simultanément de minimiser la fonction de coûts du réseau neuronal et le nombre de caractéristiques spectrales d'entrée grâce à une optimisation algorithmique multi-objectif. Par rapport aux méthodes d'interpolation 3D conventionnelles, telles que le

maillage direct 3D et le krigeage, les modèles géologiques 3D récupérés avec SFSS ajoutent une valeur prédictive à nos connaissances géologiques dans des endroits sans information de forage.

## ABSTRACT

There are several technical challenges related to data gathering, inverse modeling, model fusion and integrated interpretations in mineral exploration geophysics. In this study, new methodologies are tested and evaluated for 3D integrated interpretation of multiple geophysical images targeting mineral deposits. 3D inverse modeling of multiple geophysical data, multivariate statistics, and machine learning methods are used to develop a robust 3D integrated interpretation methodology. A cooperative inversion of multiple geophysical data is proposed for 3D imaging of an epithermal Au-Ag deposit in British Columbia (Canada). The preliminary integrated interpretation identified four petrophysical domains based on the three cooperatively inverted physical properties, including electrical resistivity, IP chargeability, and magnetic susceptibility. A 3D statistical tool is also developed to extract geological information from inverted physical property models based on independent component analysis through negentropy maximization. An automated interpretation of multiple 3D geophysical images is presented through a hybrid spectral feature subset selection (SFSS) algorithm, which is based on a generalized supervised neural network algorithm to rebuild limited geological targets from 3D geophysical images. The SFSS algorithm automatically selects the optimum combination of spectral features produced from independent components of the physical properties. Compared to conventional 3D interpolation methods such as 3D direct gridding and kriging, the 3D geological models recovered with SFSS add predictive value to our geological knowledge in places without borehole information.

Keywords: Exploration Geophysics, 3D Inversion, Gold-Silver Deposit, Feature Extraction, Feature Selection, Wavelet, Neural Networks, Genetic Algorithm

## CHAPTER I

### GENERAL INTRODUCTION

#### 1.1 Motivation

Mineral deposits are the primary source of the metals and minerals that feed our modern civilization. Despite the significant developments in the mining industry, as well as growing demand for base and precious metals, mineral exploration still faces crucial challenges. Global trends show that the number of major mineral discoveries is drastically declined during the last 25 years due to the fact that the most outcropping mineralization systems are mapped and already excavated (Barnett and Williams, 2006). Therefore, a major challenge for mineral exploration in future will be ‘deep’ targeting of hidden resources. The ‘deep’ targets are usually considered as resources as deep as hundreds of meters to thousand meters of the depth. However, occurrences of ‘deep’ targets are not limited to the third dimension, and they can be seen as complex obscured mineralization systems barely detectable within a large amount of hyper-dimensional geoscientific data. Therefore, advanced data mining methods are needed to extract useful information from large amount of data sets (Barnett and Williams, 2006). Specific strategies and methodologies are needed to decipher the interrelationship between different types of data, extracting model parameters from raw measurements and reconciling all the geoscientific patterns in an integrated modeling system. Responding to these challenges of integrating multidisciplinary information is the motivation of this Ph.D. research.

## 1.2 Problem statement

Disseminated sulfide deposits are low- to medium-grade deposits in large tonnage related to felsic to intermediate porphyritic intrusions (Simmons et al., 2005; Pirajno, 2009). They supply about 75%, 50%, and 20% of the world's Cu, Mo, and Au, respectively, as well as almost 100% of its Re (Sillitoe, 2010). They are therefore important exploration targets for the mining industries. A typical disseminated sulfide system is the result of hydrothermal fluids activities during the cooling process of magma at convergent plate tectonic boundaries (Bliss, 1992, Sillitoe, 2010). All of these interactions result in significant geochemical alterations that are important signatures of the mineral deposit occurrences. Therefore, it is essential to have a robust image of the alteration zones as geochemical attributes of mineralization systems. This is important not only in term of exploration goals (reducing the economic and environmental risk of explorations) but also on upcoming exploitations since the presence of certain geochemical alterations are likely to produce extremely acidic drainage water releasing in groundwater.

As the depth of the average discovery increases, geophysics plays an increasingly important role in the exploration of new mineral deposits for several reasons. Most geophysical surveys cover relatively large areas in a short period before the drilling programs. This large coverage expands our field of view to have a better understanding of regional geological features in connection with deposit scale footprints. Geophysical methods are mostly non-invasive and provide continuous information in space compared to punctual drilling and sampling methods. Compared to expensive and time-consuming direct assessments, geophysical methods are fast and cost-effective. Different geophysical data provide different images of the subsurface based on the underlying physical property of rocks. Inverse modeling of geophysical data results in physical property images of the subsurface. Each inverted physical property image



provides a specific amount of information about particular geological features. Incorporating multiple inverted physical property images in interpretations could provide a way to add value to our wholesome geological understanding. For example, magnetic and radiometric surveys are important methods for detection of magnetite and potassium radioelement in alteration zones (Dentith and Mudge, 2014). Electrical and Induced Polarization methods are sensitive to electrically conductive zones (conductive alterations as well as Cu/Au occurrences), and high levels of chargeability may indicate disseminated sulfide mineralization (Sumner, 1976; Dentith and Mudge, 2014).

Today, with increasing economic and environmental concerns on mineral deposit explorations, it is important to extract relevant geological features from geophysical images in an integrated methodology, in order to increase the depth of exploration. Researches in this Ph.D. thesis are therefore focused on the integrated interpretation of geophysical data targeting mineral deposits to provide a robust 3D image of the subsurface that reconciles observations. Multivariate statistics and artificial intelligence (AI) techniques are used in this study to explore the relationship between geophysical images and hidden geological features to construct a 3D geological model from geophysical data sets.

### 1.3 Geophysical 3D modeling

Simulation of a geophysical system consists of a well-posed set of equations that calculates the geophysical responses ( $S_c$ ) on the Earth surface from 3D subsurface physical property ( $P_j$ ) distributions (forward modeling):

$$S_c = f(P_j) \quad (\text{I.1})$$

Where  $f$  represents a forward problem operator in general case that simulates the target geophysical responses (signals), and  $c = 1, 2, 3, \dots, p$ , which denotes the number of  $p$  data points. In this study, finite element method is used to calculate the geophysical responses. The imaging system approximates the physical properties ( $P_j^*$ ) through inverse modeling:

$$P_j^* = f^{-1}(S_d) \quad (\text{I.2})$$

Where  $f^{-1}$  is the inverse problem operator and  $S_d$  denotes the measured signals. The task of retrieving complete information about the earth model (model space) from a certain set of geophysical data (data space) is inversion.

3D voxel inversion is used in this study to retrieve physical properties ( $P_j^*$ ) through discretization of the subsurface into rectangular cells in a 3D finite elementary mesh, where physical property values in each cell are estimated based on Equation I.1. In each iteration of inversion, a Gauss-Newton least-squares optimization tries to reduce the gap between measured and calculated geophysical responses by modifying the model parameters (physical properties,  $P_j^*$ ).

The inversion of potential field data is highly non-unique, which means the output of a magnetic inversion does not usually lead to a unique model, and many equivalent

models are producible that can be matched to the observations. Constrained inverse modeling provides a way to eliminate the unreliable equivalent models to get the most reliable 3D models of subsurface (Fullagar et al., 2000; Wisen and Christiansen, 2005; Lelièvre, 2009; Lelièvre et al., 2009). The a priori knowledge for constraining inversions could come from different sources like borehole geological observations, petrophysical measurements, and justifications from interpretations of other geophysical methods. The latter is well-known as cooperative inversion. Cooperative inversion algorithms seek to reconcile two or multiple physical property models by incorporating the inversion output from one data set as a priori knowledge for another data set (Lines et al., 1988; Paasche and Tronicke, 2007). Another approach is joint inversion, where multiple data sets are inverted simultaneously to reconcile all physical property models (Haber and Oldenburg, 1997; Doetsch et al., 2010; Chen and Hoversten, 2012; Gallardo et al., 2012; Haber and Gazit, 2013).

In this study, a cooperative inversion of multiple geophysical data is used to image 3D physical property models to refine a consistent magnetic susceptibility model by information derived from inversion of direct current (DC) electrical resistivity and induced polarization (IP) data. We also explore the effect of the smoothness and sharpness of the imaging system on the output of interpretation. This gives us a valuable view about how the sharpness of the imaging system could influence the recovered geological features, i.e., to determine which parts of the spatial domain of the original geology are vulnerable to the geophysical imaging. We explore the two end-points of the imaging scenarios (sharp versus smooth) in DC/IP inversion as well as magnetic inversion. We used a blocky inversion method for the inversion of electrical resistivity and chargeability data (Claerbout, 1973; Loke et al., 2003; Loke, 2015), and an iterative reweighting inversion (Portniaguine and Zhdanov, 2002; Geosoft Inc., 2012) for modeling the magnetic susceptibility.

#### 1.4 Feature analysis

No matter how accurate the geophysical data inversions are, each inverted physical property model is only sensitive to a limited number of geological features. Therefore, different parts of the subsurface geology can be reconstructed from various physical property models. The key question is how we can put together the interpreted jigsaw puzzles inside a high-dimensional space to rebuild a relevant geological model. This has led us to the topics of feature extraction and feature selection in the treatment of large data sets. In other word, the fundamental problem in integrated geophysical interpretation is the proper geological understanding of multiple inverted physical property images, which demands high dimensional techniques for extraction of geological information from modeled physical property images. Several methods are available for feature extraction in the high dimensional space, and this can be seen as a dimensionality increase problem (Murtaugh et al., 2000). The problem is that the increased dimensionality due to feature extraction leads to an overload of information that creates difficulties for human visual interpretation as well as machine learning optimization (Murtaugh et al., 2000). That is to say, latent patterns are lost in high space as we go to higher dimensions.

Spectral decomposing of geophysical images provide a way for feature extraction in the frequency domain (Sinha et al., 2005; Castagna and Sun, 2006). However, the underlying patterns inside the high dimensional images are just related to specific frequencies, and sometimes most of the decomposed spectra are redundant. The question is that which frequency or frequency ranges are geologically relevant. This can be seen as a dimensionality reduction problem, in which one tries to extract the best representative components of high dimensional images to facilitate the visual interpretations and machine learning optimization. Feature subset selection (FSS) provides a powerful tool for intelligent dimensionality reduction and AI feature

learning (Liu and Motoda, 2012). FSS reduces the size of a large set of the input features to a new set of relatively small and representative input features that improve the accuracy of neural network prediction (Huang and Wang, 2006). Therefore, unlike conventional statistical dimensionality reduction methods that are blind source separation algorithms, there is a criterion for selection of the best features that can be expressed as optimization of the neural learning process, in the light of both neural weights and number of selected input features (Zhao and Liu, 2011).

Within the frame of this Ph.D. study, we present a spectral ICA algorithm for dimensionality reduction as well as separation of high dimensional spectral overlapped features. We also propose a method that automatically selects the best representative spectral components based on multi-objective machine learning optimization.

### 1.5 Research outline

In this study, a systemic approach is used to understand the whole process of interpretation that links the underlying geological features (lithology and alteration) to physical properties and measured signals on the surface. The integrated interpretation is presented in three stages:

- Integrated Modeling (Chapters II, III): responding to challenges related to 3D inverse modeling of multiple geophysical data and the interrelationship between physical properties and geological features;
- Feature extraction (Chapters IV): higher order statistical algorithms are applied for geological source separation;
- Spectral feature selection (Chapter V): a hybrid machine learning algorithm is provided for semi-automatic interpretation of multiple geophysical images.

## CHAPTER II

### 3D COOPERATIVE INVERSION OF MAGNETIC AND DC/IP DATA OVER NEWTON EPITHERMAL AU-AG DEPOSIT IN BRITISH COLUMBIA, CANADA

Bahman Abbassi, Li Zhen Cheng, Jeremy P. Richards, Juliane Hübert, Jean M.  
Legault, Mark Rebagliati and Ken Witherly

This paper was submitted to Geophysics in March 2018 (under review)



## Résumé

Une inversion coopérative de données géophysiques multiples est utilisée pour l'imagerie 3D du gisement d'Au-Ag épithermal de Newton en Colombie-Britannique (Canada). Les données de résistivité électrique et de polarisation provoquée (PP) à courant continu (CC), et aéromagnétiques ont été inversées séparément pour récupérer des distributions de propriétés physiques 3D approximatives. Une inversion de vecteur d'aimantation (IVA) non contrainte a été utilisée pour modéliser la distribution 3D des vecteurs d'aimantation. Cependant, la profondeur des caractéristiques magnétiques dans le IVA était incertaine en raison de la non-spécificité inhérente de l'inversion non contrainte. Le modèle de résistivité à l'échelle du dépôt montre une zone modérément résistive avec une faible chargeabilité dans une large zone conductrice / chargeable NW-SE, confirmant l'hypothèse qu'une zone localisée de haute résistivité / faible chargeabilité est associée au processus de dévitrification et aux espaces poreux remplis de quartz, la zone riche en Au. Le succès de l'inversion PP / CC dans la localisation de cette zone riche en Au modérément résistive / faible chargeable a fourni une contrainte précieuse sur l'inversion magnétique sur l'échelle de dépôt, pour une meilleure localisation de la zone de faible susceptibilité associée à la minéralisation. Une inversion magnétique- PP / CC coopérative est utilisée pour affiner un modèle de susceptibilité géologiquement cohérent en incorporant des informations dérivées de l'inversion PP / CC. Nous avons remarqué que l'influence de l'inversion PP / CC sur l'inversion coopérative n'était pas uniforme sur le plan horizontal, ce qui nous a conduit à utiliser une pondération non uniforme de la contrainte de chargeabilité lors de l'inversion coopérative. La procédure a permis aux parties utiles de l'inversion PP / CC de participer à la reconstruction de la susceptibilité. Les évaluations à l'échelle du gisement montrent que le modèle de susceptibilité coopérative est compatible avec les informations géologiques et pétrophysiques antérieures. Le modèle magnétique récupéré montre une zone magnétique basse correspondant à des intrusions

porphyriques et des roches volcaniques felsiques (hôte d'Au) qui sont mises en place dans une large zone magnétique de forme ovale NW-SE liée à l'altération hydrothermale.



## Abstract

A cooperative inversion of multiple geophysical data is used for 3D imaging of the Newton epithermal Au-Ag deposit in British Columbia (Canada). Aeromagnetic, direct current (DC) electrical resistivity and induced polarization (IP) data were separately inverted to recover approximate 3D physical property distributions. An unconstrained magnetization vector inversion (MVI) was used to model the 3D distribution of magnetization vectors. However, the depth of the magnetic features in the MVI was uncertain due to the inherent non-uniqueness of the unconstrained inversion. The deposit-scale resistivity model showed a moderately resistive zone with low chargeability inside a broad NW-SE conductive/chargeable zone, which confirmed the hypothesis that a localized high resistivity/low chargeability zone is associated with devitrification process and pore spaces filled with quartz in the Au-rich zone. The success of DC/IP inversion in the localization of this moderately resistive/low chargeable Au-rich zone provided a valuable constraint on the magnetic inversion on deposit scale, for better localization of the low susceptibility zone associated with Au mineralization. A cooperative magnetic-DC/IP inversion is used to refine a geologically consistent susceptibility model by incorporating information derived from DC/IP inversion. We noticed that the influence of the DC/IP inversion on the cooperative inversion was not uniform on the horizontal plane, and this led us to use a non-uniform weighting of the chargeability constraint during the cooperative inversion. The procedure allowed the useful parts of the DC/IP inversion to participate in the reconstruction of the susceptibility model. Evaluations at the deposit scale show that the cooperative susceptibility model is compatible with prior geological and petrophysical information. The recovered magnetic model shows a low magnetic zone corresponds to porphyritic intrusions and felsic volcanic rocks (host of Au), which is emplaced within a broad NW-SE oval-shape high magnetic zone related to the hydrothermal alteration.

## 2.1 Introduction

Multidisciplinary geoscientific data integration enables interpreters to better understand and identify physical processes within the Earth. The integrated interpretations provide a framework for reconciling rock physical properties with geological observation and helps interpreters explore the 3D interrelationship between existing geological features and the imaged physical properties of rocks (Lelièvre et al., 2009; Moorkamp et al., 2016).

Epithermal deposits precipitate by circulation of hydrothermal fluids and subsequent changes in their physicochemical conditions. The host rocks undergo varying degrees of overprints of hydrothermal alteration because the mineral assemblages in the wall rocks tend to geochemically re-equilibrate during the hydrothermal activity (Taylor, 2007, Pirajno, 2009). Hydrothermal fluids during replacement processes concentrate precious and base metals in pore spaces and structurally controlled fracture zones (Sillitoe and Hedenquist, 2003; Sillitoe 2015).

Geophysical characteristics of several epithermal systems have been discussed in a handful of case studies (Allis, 1990; Irvine and Smith, 1990; Feebreyf et al., 1998; Murakami, 2008; Morrell et al., 2011; Clark, 2014; Hübner et al., 2016; Legault et al., 2016). Many of the intrusive complexes responsible for hydrothermal mineralization are to some extent magnetized in contrast to the country rocks (Clark, 2014). Nevertheless, in epithermal systems, destructive magnetite alteration could produce low magnetic anomalies accompanied by mineralization (Pirajno, 2009; Clark, 2014). Magnetic surveys can usually identify this mineralization signature exhibiting as localized magnetic-lows surrounded by high magnetic zones (Allis, 1990; Irvine and Smith, 1990; Murakami, 2008; Morrell et al., 2011).

Electrical resistivity-highs in the epithermal systems (locally exceeding 1000 Ohm-m) are reported being associated with silicification, compaction, and felsic to intermediate intrusions (Allis, 1990). Low resistivities from sulfidation (3-30 Ohm-m; Allis, 1990), which are most favorable to hydrothermal exploration, are often mixed with resistivity-lows of pore fluid and pervasive clay alteration (Nelson and Van Voorhis, 1983; Allis, 1990; Irvine and Smith, 1990). Strong IP chargeabilities due to the hydrothermal alteration are typically associated with the presence of sulfidation (Sumner, 1976; Allis, 1990). Nelson and Van Voorhis (1983) have shown that the polarization response in disseminated mineralization increases somewhat linearly with an elevation of sulfide contents up to 10 percent.

Geophysical inverse modeling is a valuable tool in geophysical interpretation because it produces physical property models that are used for imaging geological features in 3D (Oldenburg and Li, 1994; Li and Oldenburg, 1997, 2000; Loke et al., 2003; Lelièvre and Oldenburg, 2009; Loke, 2015). However, because of the inherent uncertainty of the geophysical inversion, the solution of the inverse problem may produce multiple 3D physical property models that are equally valid when there is no prior information about the underground. One way to solve this non-uniqueness problem is constraining the model with prior information from geological setting, borehole records, and other geophysical models. The latter can be addressed through cooperative inversion, in which information from one geophysical data set are used in the inversion of another dataset (Oldenburg et al., 1997; McMillan and Oldenburg, 2014; Moorkamp et al., 2016). Oldenburg et al. (1997) incorporated a cooperative strategy to constrain a DC/IP inversion with information from a standard susceptibility inversion from Mt. Milligan Cu-Au porphyry deposit. They followed the hypothesis of an anti-correlation between IP chargeabilities and magnetic susceptibilities and performed a cooperative DC/IP inversion with a proper weighting model that encourages the DC/IP inversion to place higher chargeabilities away from higher susceptibilities.

This study aims to characterize Newton epithermal deposit by exploring the relationships between geological, petrophysical and multiple geophysical data-sets. A cooperative magnetic-DC/IP inversion is used to image 3D physical property distributions in the Newton area, to refine a consistent magnetic susceptibility model by information derived from DC/IP inversion.

The Newton deposit consists of dissemination of Au and Ag as inclusions in pyrite with variable amounts of Cu mineralization. The deposit is located in central British Columbia, Canada and is classified as an intermediate sulfidation epithermal deposit (Pressacco, 2012; McClenaghan, 2013; Liu et al., 2015). Explorations in the area have been conducted since the 1970s and comprise geological and geochemical observations and geophysical measurements (Pressacco, 2012). The most recent study (Hübert et al., 2016) has modeled regional electrical resistivity structure of the Newton deposit using magnetotelluric (MT) and airborne z-axis tipper electromagnetic (ZTEM) data. The area of hydrothermal mineralization exhibits a modest electrical response relative to the country rocks, mainly due to the presence of phyllosilicate minerals (sericite) and minor disseminated sulfides (Hübert et al., 2016). However, the ZTEM-MT resistivities do not possess the resolution of the deposit scale geological features (Hübert et al., 2016).

In this study, multiple geophysical data sets are inverted on larger scales to localize the physical properties of the Newton Au-rich zone. At prospect scale, each geophysical data set is inverted individually to produce separate physical property models in 3D. The prospect scale modeling covers an area of highly altered rocks encompassing the Newton deposit and is accompanied by MVI and DC/IP inversion that retrieve the 3D magnetization vectors, electrical resistivities and IP chargeabilities of the hydrothermal zone. The cooperative magnetic-DC/IP inversion is performed on a deposit scale and has produced consistent physical property models that are evaluated

by geological and petrophysical observations. We show that the cooperative inversion uncovers hidden geological features inside the retrieved physical property models, without incorporating any prior borehole geological constraint.

## 2.2 Geological setting

Newton Au-Ag deposit is a Late Cretaceous ( $72.1 \pm 0.3$  Ma; McClenaghan, 2013) epithermal deposit in association with arc magmatism in the accreted Stikinia terrane of western Canada, along with several significant porphyry and epithermal deposits (McMillan et al., 1995; Nelson and Colpron, 2007), such as Capoose epithermal Au deposit, Blackwater epithermal Au-Ag deposit and Prosperity porphyry Cu-Au deposit (Figure 2.1).

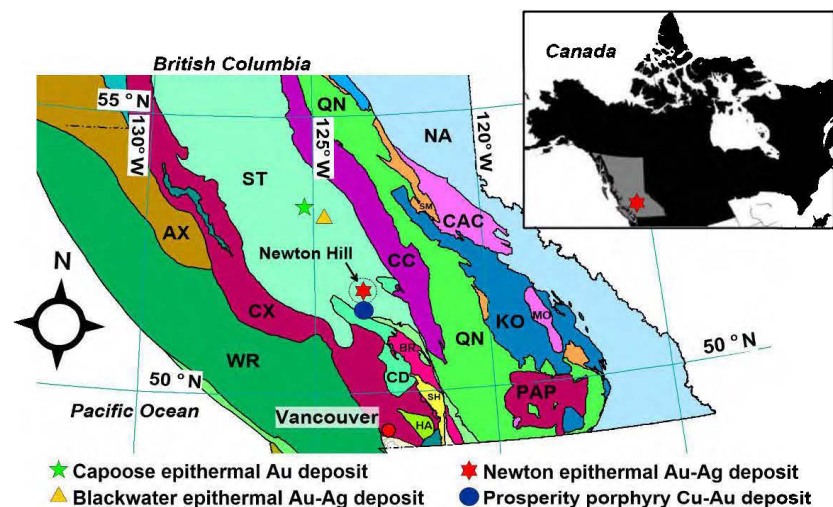


**Figure 2.1** Several large porphyry and epithermal deposits located in Stikinia terrain (ST) in central British Columbia. Other terranes are: Alexander terrane (AX); Bridge River terrane (BR); Caribo terrane (CAC); Cache Creek terrane (CC); Cadwallader terrane (CD); Coast Complex terrane (CX); Harrison terrane (HA); Kootenay Terrane (KO); Monashee (MO); Cratonal North America terrane (NA); Nisling terrane (NI); Post Accretionary Plutons (PAP); Quesnellia terrane (QN); Shuksan terrane (SH); Slide Mountain Terrane (SM); Wrangellia (WR). Modified from Massey et al. (2005).

Regionally, the Late Cretaceous volcanic sequence is overlain by Miocene-Pliocene Chilcotin Group flood basalts, and Quaternary glacial deposits, which are variably eroded to expose the older rocks. In deposit scale, quaternary glacial tills cover most of the Newton property. Consequently, deposit scale geological information has primarily been obtained from borehole samples (Pressacco, 2012). A bedrock geology map of the property is compiled from the mapping of limited outcrops, drill cores and cross-section interpretations (Figure 2.2). Three layered volcano-sedimentary sequences overlain on each other from bottom to top are mafic volcanic rocks, sedimentary rocks and felsic volcanic rocks ( $72.1 \pm 0.6$  Ma; McClenaghan, 2013). The layered rocks are intruded by felsic to intermediate porphyritic intrusions, including the monzonite ( $72.1 \pm 0.3$  Ma; McClenaghan, 2013), quartz feldspar porphyry (QFP;  $70.9 \pm 0.5$  Ma; McClenaghan, 2013), feldspar biotite porphyry (FBP) and the younger dioritic intrusion ( $69.3 \pm 0.4$  Ma; Liu et al., 2015).

Amarc Resources Ltd. acquired the property in 2009 and defined an estimated inferred mineral resource of 111.5 Mt with an average grade of 0.44 g/t Au (cut-off at 0.25 g/t Au; Pressacco 2012). The epithermal mineralization associated with the Newton deposit is at a depth of ~50 m to ~600 m. Au-Ag mineralization is characterized by quartz-sericite alteration, containing disseminated pyrite with Au inclusions in coeval porphyritic intrusive rocks. Au-Ag mineralization is associated with disseminated pyrite, marcasite, and base metal sulfides, and is mainly hosted within the felsic volcanic sequence (McClenaghan, 2013; Liu et al., 2015). The deposit is offset by the Newton Hill Fault (NHF), which displaces the geology and mineralization by ~300 m of normal dip-slip movement.

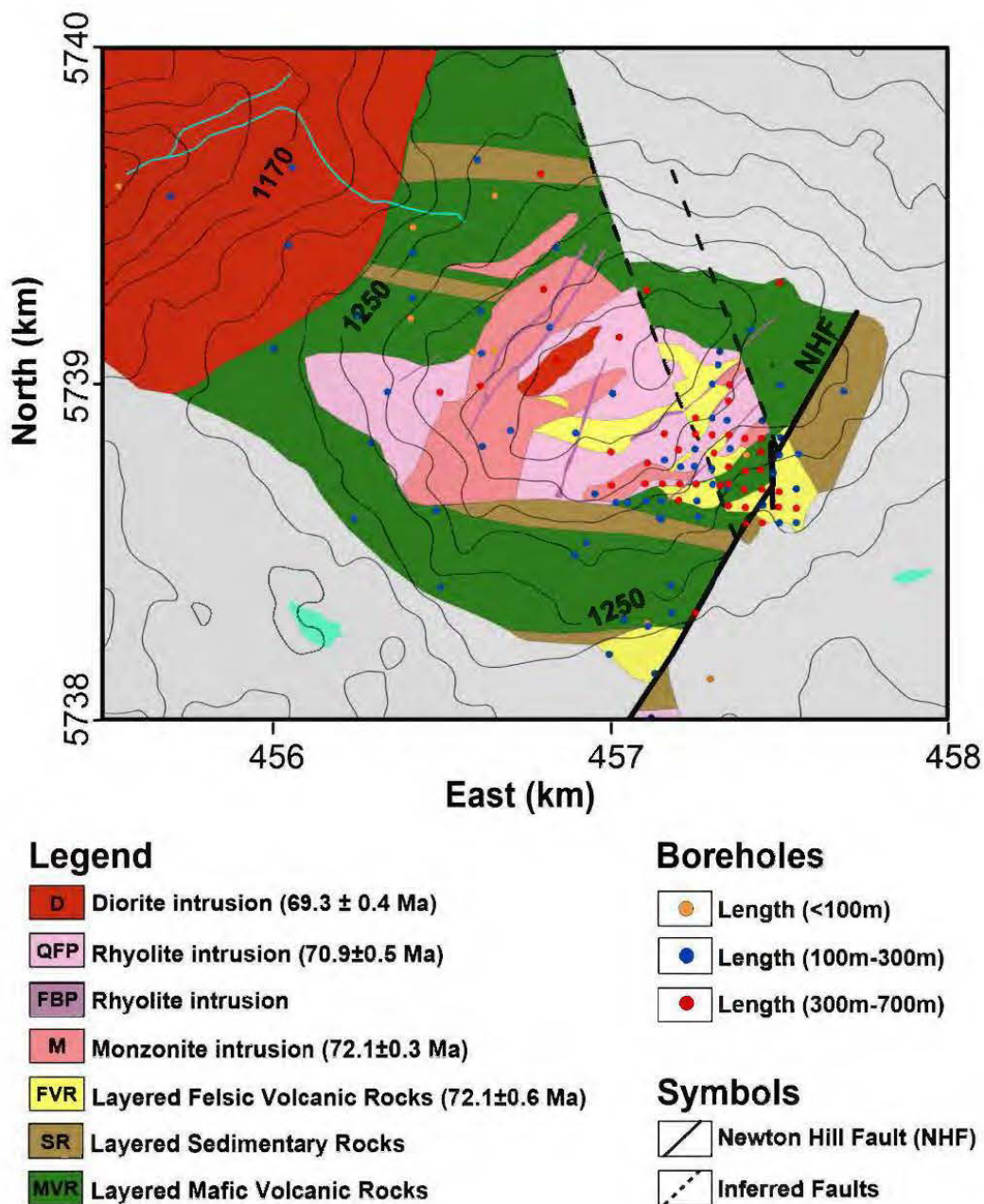


**Figure 2.2** Bedrock geology map at the deposit scale. Colored dots indicate drillhole locations with various total lengths (Pressacco, 2012; McClenaghan, 2013). The light gray parts are undefined regions due to the lack of borehole information in the periphery of the deposit. Contours indicate topography.

### 2.3 Physical properties

More than 9000 magnetic susceptibility readings are measured from core samples from 80 drill holes in the Newton Hill area. Measurements are done using KT-10 S/C meter of Terraplus Inc. and are supported by additional data provided by Amarc Resources Ltd. The retrieved statistics of magnetic susceptibilities of different lithologies are shown as a box plot in Figure 2.3. Felsic volcanic rocks (FVR) and porphyritic intrusions (QFP and M) show lowest magnetic susceptibilities (in average less than 0.0002 SI), and sedimentary rocks (SR) are slightly more magnetic (average 0.0005 SI). The high amplitude susceptibility anomaly (more than 0.01 SI in average) is likely due to a blend of mafic volcanic rocks (MVR) with propylitic alteration and the later developed dioritic intrusion (D). Figure 2.4 shows horizontal slices from the borehole 3D models of susceptibilities and Au concentrations.

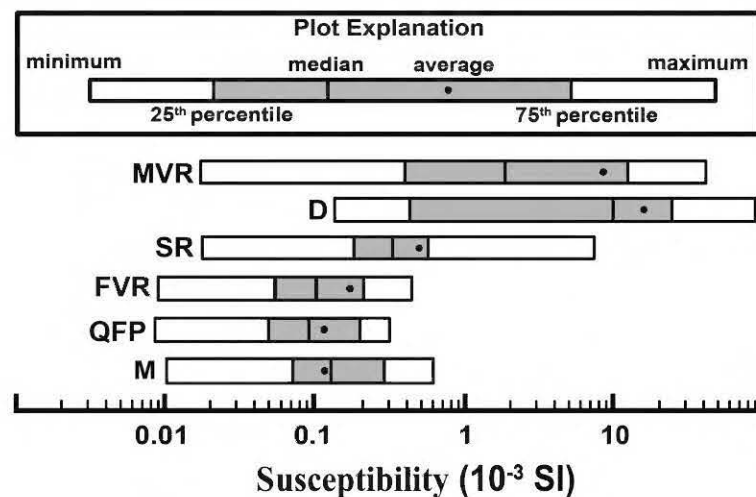


**Figure 2.3** Boxplot demonstration of measured magnetic susceptibilities of different lithologies from the Newton deposit. Susceptibility axis is logarithmic. The lithologies with average susceptibility values are: monzonite (M, 0.00012 SI); quartz feldspar porphyry (QFP, 0.00012 SI); felsic volcanic rocks (FVR, 0.00017); sedimentary rocks (SR; 0.00017); diorite (D, 0.014 SI); mafic volcanic rocks (MVR, 0.009).



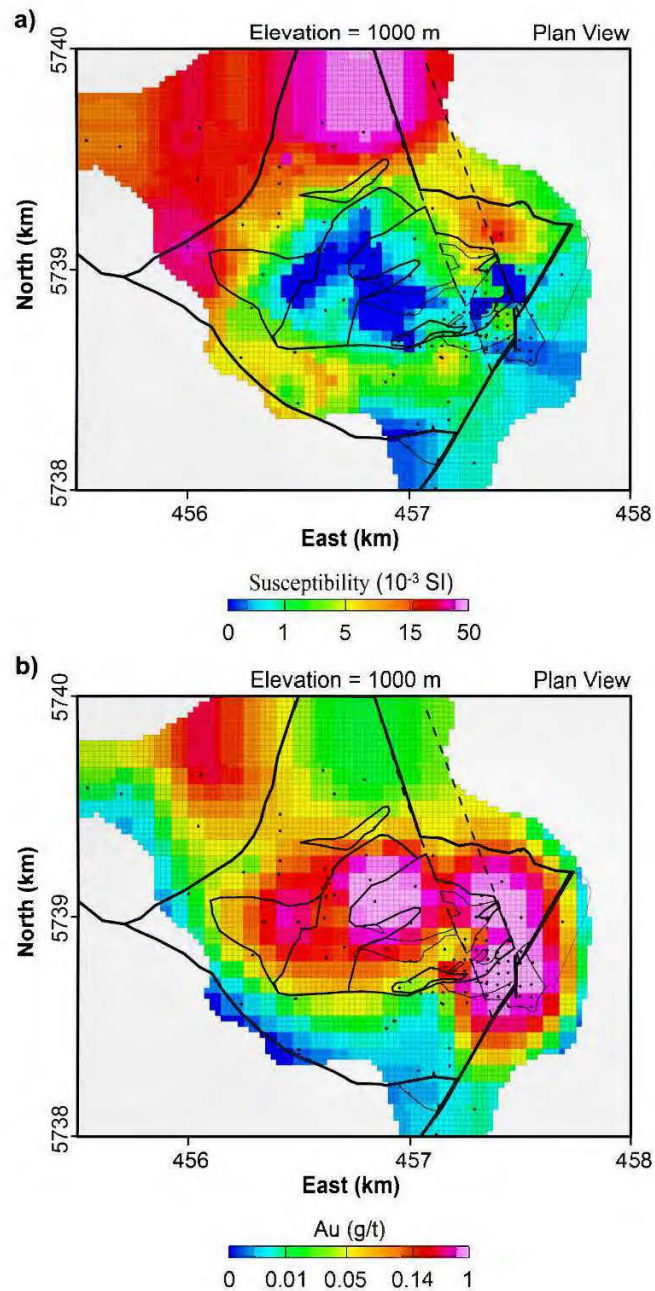


**Figure 2.4** 3D borehole models. (a) Borehole susceptibility model. (b) Au concentration model (b). Both models are sliced horizontally at the elevation of 1000 m. Bedrock geology is overlaid on both models. Black dots indicate the location of boreholes.

There is a correlation between high concentrations of Au and low susceptibilities of the felsic volcanic rocks. The susceptibility of mafic volcanic rocks is amplified due to the precipitation of magnetite-bearing propylitic alteration. In the Au-rich zone, susceptibility-low of the felsic volcanic rocks also becomes weaker due to the further destructive magnetite alteration during the epithermal process. Therefore, the epithermal alteration assemblages increase the susceptibility contrasts of rocks that can be imaged as sharp changes between two principal zones:

1. The high susceptibilities of the mafic volcanic rocks with propylitic assemblage (chlorite-epidote-pyrite-calcite-albite-magnetite), and the later dioritic intrusion in the northwest of Newton Hill.
2. The low susceptibilities of the felsic volcanic rocks with quartz-sericite alteration assemblage and Au enrichments.

The sericitic alteration associated with Au-Ag mineralization suggests the source magmatic fluids of mineralization were slightly acidic and likely caused devitrification of minerals, resulting in the formation of additional pore space for subsequent precipitation of sericite and quartz in the zone of mineralization (McClenaghan, 2013). Since the silicified zone accompanied by mineralization is resistant to weathering (McClenaghan, 2013); the pick of the topography over Newton Hill is an indirect sign of the devitrification. Devitrification (McClenaghan, 2013) can also be accompanied by a local reduction of chargeability and an elevation of resistivity near the mineralization zone, as well as the low susceptibilities of the destructive magnetite alteration linked to the epithermal mineralization. We test this hypothesis in the interpretation of modeled physical properties.

## 2.4 Geophysical data

Geotech Ltd. has acquired the aeromagnetic data as a part of the combined magnetic and ZTEM survey, from January to February 2010 on behalf of Amarc Resources Ltd (Geotech Ltd., 2010). The ZTEM data-sets are described in Hübner et al. (2016). Total magnetic field data were measured from a helicopter flown at a mean height of 155 m above ground. This allowed for a ZTEM sensor terrain clearance of 81 m and a magnetic sensor clearance of 98 m (Geotech Ltd., 2010). The data were collected along N-S flight lines at 200 m spacing and E-W tie lines flown every ~2000 m to 500 m (tighter spacing near the deposit). A total of 7071 line-km of data were collected and cover a 1293 km<sup>2</sup> area. The magnetometer sampling rate was 0.1 second and depending on the speed of the helicopter results in approximately 10 m measurement intervals along each profile. The magnetic anomalies are displayed in Figure 2.5.

A DC/IP survey of 85 line-km over Newton Hill area, using the pole-dipole electrode configuration was conducted in 2010 (Pressacco, 2012). The survey lines were spaced at 200 m intervals in E-W directions within the zone of hydrothermal alteration. The unit electrode spacing (dipole length) was set to 100 m and 200 m, with maximum eight times dipolar separations. The apparent chargeabilities were measured by recording the decaying voltage after the current cut-off in millivolt per volt (mV/V). The measured apparent resistivities and chargeabilities are presented in Figures 2.6a and 2.6b, respectively.

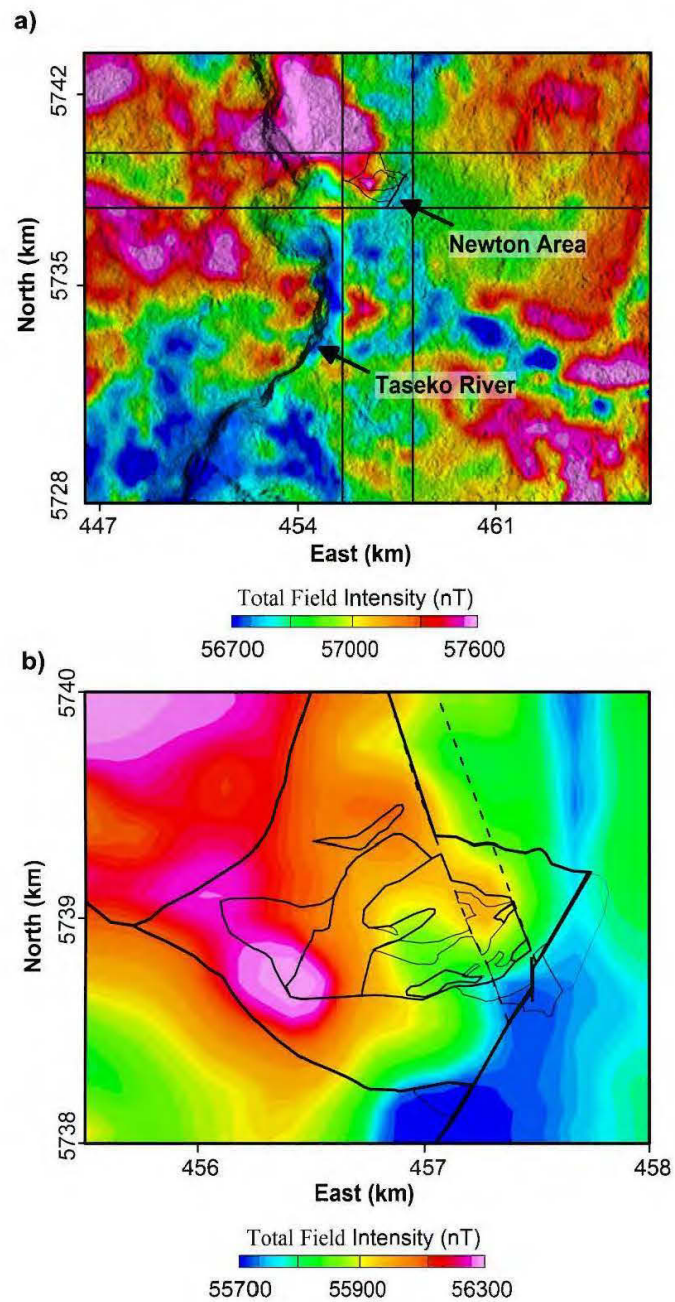


**Figure 2.5** Magnetic data-sets. (a) Total magnetic field intensities on a regional scale. Data are draped on a shaded relief digital elevation model of the region. (b) Total magnetic field intensities on Newton deposit scale. Black lines outline the bedrock geology contacts.

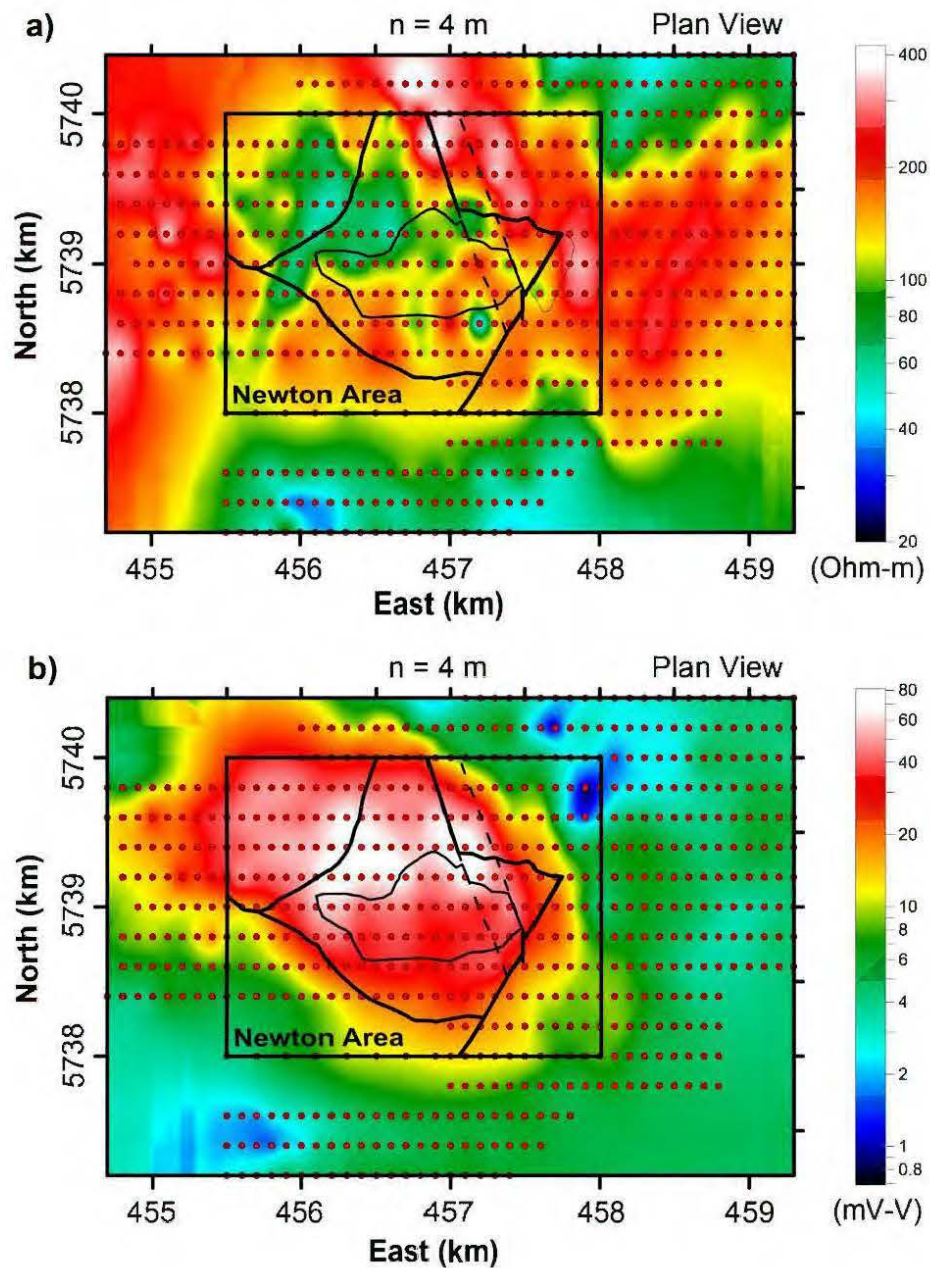


**Figure 2.6** DC/IP data-set. Plan maps are showing the locations of DC/IP electrodes covering the halo of hydrothermal alteration over the Newton area. (a) Measured apparent resistivities. (b) Measured apparent chargeabilities. Data are shown for the dipolar length of 100 m and dipolar separation of  $n = 4$ .

## 2.5 3D Magnetization vector inversion

The fundamental assumption in a conventional magnetic susceptibility inversion (Li and Oldenburg, 1997) supposes that the remanent magnetization vector ( $\vec{J}_{Rem}$ ) is negligible within rocks and the total magnetization comes exclusively from the earth's magnetic induction within rocks. In this case, the total magnetization vector ( $\vec{J}_{Total}$ ) is equal to the inductive magnetization vector ( $\vec{J}_{Ind}$ ) and is parallel to the earth's magnetic field vector ( $\vec{H}_0$ ) direction. Therefore, the estimation of magnetic susceptibility ( $\chi$ ) of rocks gets simplified to a scalar form that can be rewritten as a function of (Lelièvre and Oldenburg, 2009):

$$\chi = \left| \vec{J}_{Ind} \right| / \left| \vec{H}_0 \right| \quad (\text{II.1})$$

However, the existence of remanent magnetization (usually in different directions than the present-day earth's magnetic field) may result in distorted total magnetization depending on the spatial relationship of the inductive magnetization vector ( $\vec{J}_{Ind}$ ) and a remanent magnetization vector ( $\vec{J}_{Rem}$ ) (Lelièvre and Oldenburg, 2009; Ellis et al., 2012). Therefore, the total magnetization vector is expressed as (Lelièvre and Oldenburg, 2009):

$$\vec{J}_{Total} = \vec{J}_{Ind} + \vec{J}_{Rem} \quad (\text{II.2})$$

We used magnetization vector inversion (MVI; Lelièvre and Oldenburg, 2009; Ellis et al., 2012) to extract a 3D model of the total susceptibility distribution in the Newton area. The cell dimensions of the MVI model are 110 m (in X-direction), 80 m (in Y-direction) and 20 m (in Z-direction) that comprise total 112896 cells, covering a surface of 5660 m by 3780 m and down to ~2000 m of depth in the deposit scale.



The MVI algorithm introduces both the amplitude and the magnetization vector direction as separate unknowns in a Tikhonov minimum gradient regularization (Lelièvre and Oldenburg, 2009; Ellis et al., 2012). The ratio of the amplitude of the inverted total magnetization vector, normalized by the Earth's geomagnetic field, yields the total susceptibility (Lelièvre and Oldenburg, 2009):

$$\chi_{Total} = \left| \frac{\mathbf{J}_{Total}}{H_0} \right| = \left| \mathbf{J}_{Ind} + \mathbf{J}_{Rem} \right| / \left| H_0 \right| \quad (II.3)$$

An Iterative Reweighting Inversion (IRI) method is also used in parallel to the MVI modeling in this study (Portniaguine and Zhdanov, 2002; Geosoft Inc., 2012). IRI takes the first iteration susceptibility (or magnetization vector) and uses it as an iterative reweighting constraint when running a new inversion. This process is iterated until a satisfactory model is achieved (Geosoft Inc., 2012). IRI tends to recover sharp magnetic variations, and its results are equivalent to Robust or Blocky Inversion in inverse modeling of DC/IP data (Claerbout, 1973; Loke et al., 2003).

The preliminary MVI results are shown in Figure 2.7 for different rounds of reweighting. The recovered susceptibility model is converged to a stable solution at the fourth iteration (IRI4 in Figure 2.7d). As can be seen, the igneous rocks in the west of the NHF correspond to relatively high susceptibilities with NW-SE trend and an inner low susceptibility zone associated with mineralization. However, the low susceptibility zone is not localized as it was expected from prior geological and petrophysical information (Figure 2.4). This remark motivated us to establish a cooperative method to constrain the magnetic inversion with 3D DC/IP inversion results for more efficient imaging of the low susceptibility feature associated with Au mineralization.

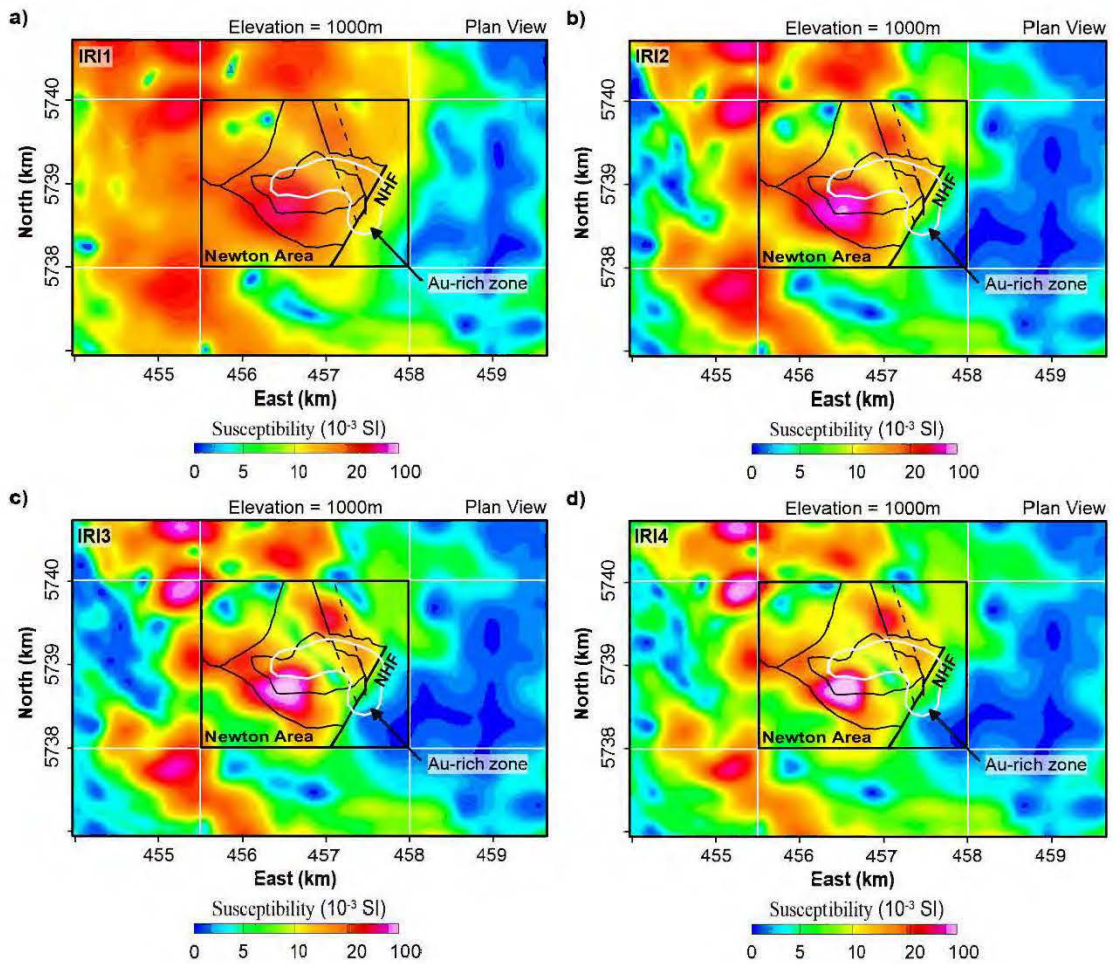


**Figure 2.7** MVI models sliced at the elevation of 1000m. (a) First sharpening round. (b) Second sharpening round. (c) Third sharpening round. (d) Fourth sharpening round. Outline of Au mineralization is shown in the white contour. Bedrock geology is overlaid on all slices.



## 2.6 3D DC/IP inversion

A 3D DC/IP inversion algorithm is employed using a robust inversion method (Loke, 2015) that produces sharp resistivity and chargeability images. In the forward calculation subroutine of the inversion program, the unit electrode spacing in X and Y directions is set to 100 m and 200 m, respectively. Model cells are set to increase exponentially with depth in 20 intervals. Electrodes were distributed on a 50 m by 100 m horizontal plane, and the model mesh consists of 72000 trapezoidal cells.

Inversion of DC/IP data considers the IP chargeability model as a small perturbation of the reference electrical conductivity model (Oldenburg and Li, 1994; Li and Oldenburg, 2000). Normalized chargeability ( $0 \leq m \leq 1$ ) tends to decrease the reference conductivity ( $\sigma_{DC}$ ) in the modeled IP phenomenon and produces a perturbed subsurface conductivity ( $\sigma_{IP}$ ) in the function of (Oldenburg and Li, 1994):

$$\sigma_{IP} = (1 - m)\sigma_{DC} \quad (\text{II.4})$$

The program calculates the forward potential responses of two conductivity models ( $\sigma_{DC}$  &  $\sigma_{IP}$ ) separately. In the presence of sharp resistivity changes, improved initial  $\sigma_{DC}$  &  $\sigma_{IP}$  models can be obtained by using an approximate inverse mapping (Oldenburg and Ellis, 1991). The forward modeling of  $\sigma_{DC}$  gives the apparent conductivity values ( $\sigma_a$ ), and the modeled potentials ( $\phi$ ) can then be used to calculate the apparent chargeabilities based on (Oldenburg and Li, 1994):

$$m_a = [\phi(\sigma_{IP}) - \phi(\sigma_{DC})] / \phi(\sigma_{DC}) \quad (\text{II.5})$$

In each iteration, an Incomplete Gauss-Newton least-squares optimization tries to reduce the gap between measured and calculated properties ( $\sigma_a$  and  $m_a$ ) by changing the  $\sigma_{DC}$  and  $\sigma_{IP}$  values. When the calculation reaches its threshold, the modeled resistivities and chargeabilities are determined by  $\rho = 1 / \sigma_{DC}$  and  $m = 100[1 - (\sigma_{IP} / \sigma_{DC})]$ , respectively.

The robust inversion (Loke et al., 2003), which uses an extension of  $l^2$ -norm and  $l^1$ -norm inversions, incorporates two cut-off factors in the DC/IP inversion: A data constraint cut-off factor ( $0 < k_1 < 1$ ), and a model constraint cut-off factor ( $0 < k_2 < 1$ ). Large cut-off factors result in smooth physical property models equivalent to  $l^2$ -norm results. The robust DC/IP inversion is controlled by different cut-off factors to see which output is more consistent with our prior knowledge of the region. Getting too close to the  $l^2$ -norm criteria (larger cut-off factors) increased the misfit error. Closer to  $l^1$ -norm (smaller cut-off factors) produced too sharp boundaries not consistent with magnetic inversion and prior geological information. The most geologically consistent results obtained with  $k_1 = 0.05$  and  $k_2 = 0.01$ . The  $k_1 = 0.05$  value means the effect of noisy data points (where the difference between the measured and calculated apparent physical properties are greater than five percent) are greatly reduced. The  $k_2 = 0.01$  value means the effect of calculated data points (where the difference between the measured and calculated apparent physical properties are greater than one percent) are significantly reduced. This helped us to better localize the sharp physical property contrasts. The results of the preliminary 3D inversion of DC/IP data are illustrated in Figure 2.8 on the prospect scale. As can be seen in Figure 2.8a, the low resistivity zone with a NW-SE trend is probably related to the low resistive phyllosilicates and sulfide concentrations of the epithermal system that is confined by a high resistivity periphery.

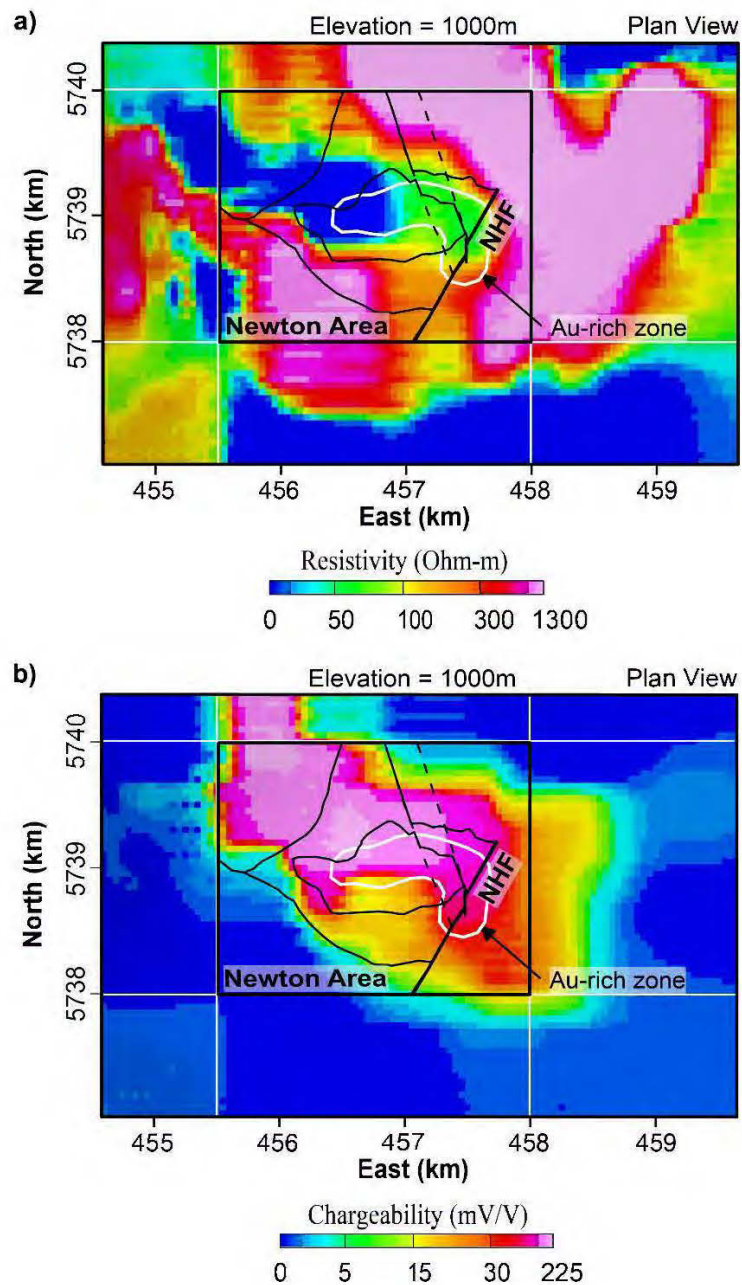


**Figure 2.8** Preliminary inversion of DC/IP data over the Newton deposit. (a) Resistivity model sliced at elevation 1000 m. (b) Chargeability model sliced at elevation 1000 m. Outline of Au mineralization is shown in the white contour. Bedrock geology is overlaid on both slices.

The chargeability high zone (more than 50 mV/V in Figure 2.8b) coincides with low resistivity zone (less than 50 Ohm-m in Figure 2.8a). This physical property structure indicates 2-7% disseminated sulfide concentrations in the area of hydrothermal alteration, including pyrite, marcasite, sphalerite, chalcopyrite, and arsenopyrite.

### 2.7 3D cooperative inversion of magnetic and DC/IP data

Before running the cooperative inversion, we needed to determine the existence of any correlation between the IP chargeability and the magnetic susceptibility models. We observed a link between the chargeabilities and susceptibilities by direct comparison of a deposit-scale DC/IP inversion results to the susceptibility of borehole samples. This physical property coupling led us to use DC/IP inversion results to constrain the magnetic susceptibility model. DC/IP inversion was carried out on deposit scale (boreholes range). The total number of cells in the forward DC/IP calculations is 288000, and each cell has a 25 m by 50 m size in the horizontal plane. Model cells are also set to increase exponentially with depth in 20 intervals down to 600m of depths. The deposit scale DC/IP inversion results are shown in Figure 2.9. The recovered electrical resistivity model shows a moderately high resistive zone inside a NW-SE conductive zone. As it was predicted, the location of this localized high resistivity / low chargeability zone is associated with devitrification process and pore spaces filled with quartz in the Au-rich zone that is right beneath the pick of the Newton Hill topography (Figure 2.9a).

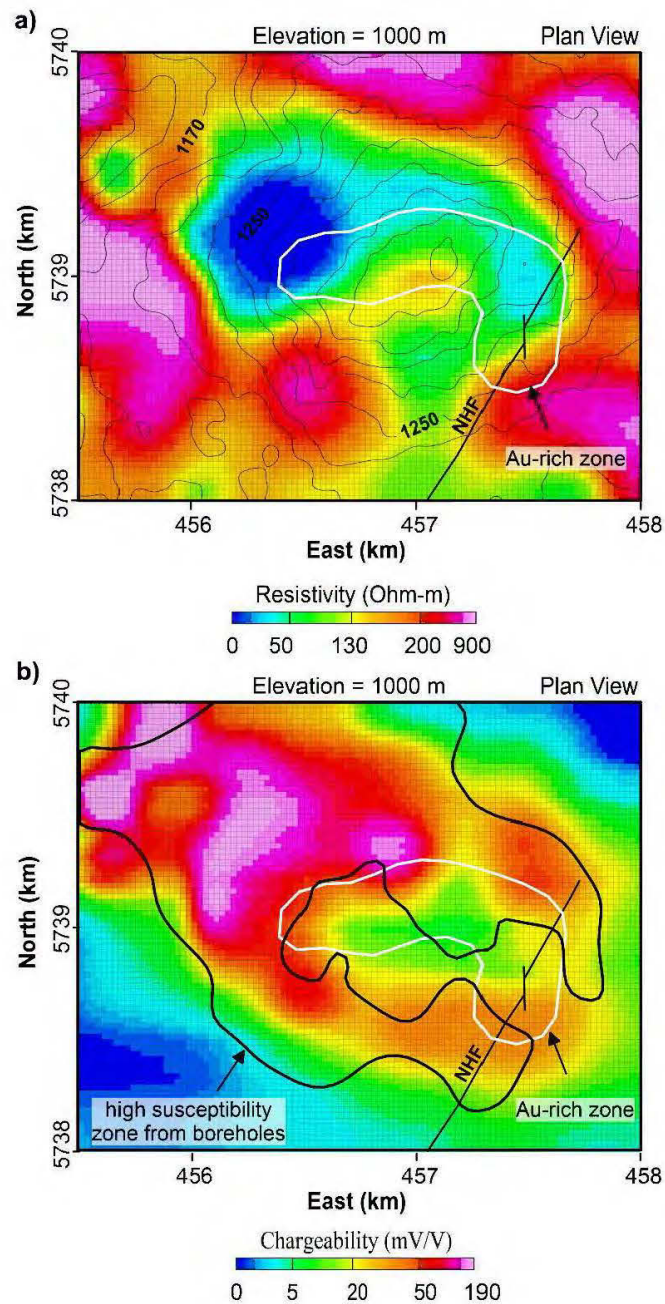


**Figure 2.9** Deposit scale DC/IP inversion sliced at the elevation of 1000 m. (a) Electrical resistivity model (contours indicate topography). (b) IP chargeability model compared to the borehole magnetic-highs (black contour). Outline of Au mineralization is shown in the white contour.

The results also show an anticorrelation between the Au concentrations and magnetic susceptibilities of borehole samples (Figures 2.4 and 2.10a). However, a positive correlation is also observed between the recovered chargeabilities and the susceptibilities measured on borehole samples (Fig 2.10b).

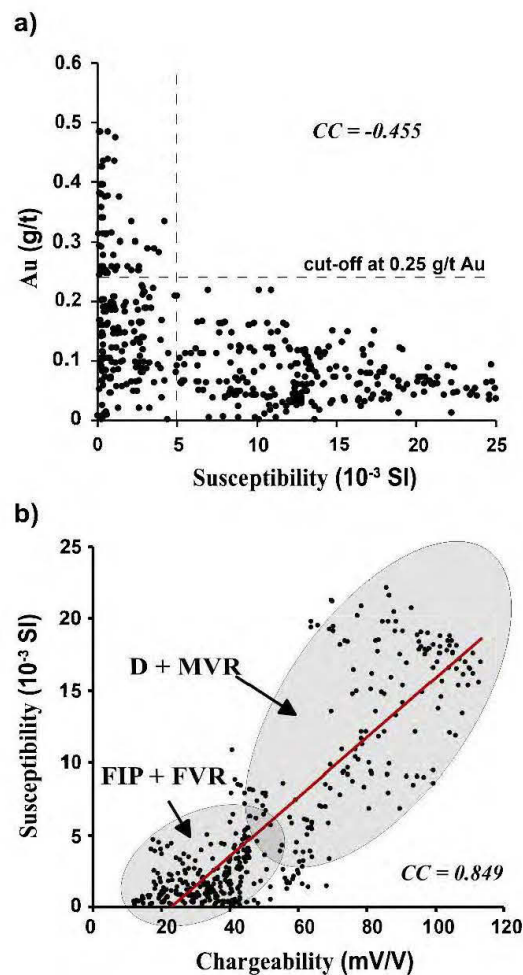


**Figure 2.10** Susceptibilities of rock samples versus inverted chargeabilities and Au concentrations. (a) Anticorrelation between the susceptibilities and Au concentrations. (b) Correlation between the chargeabilities and susceptibilities. Low susceptibility/chargeability porphyritic intrusions (FIP) and felsic volcanic rocks (FVR) are divided from high susceptibility/chargeability mafic volcanic rocks (MVR) and dioritic intrusions (D).  $CC$  indicates correlation coefficient.

Based on the  $\chi_{IP}$  model we calculated its forward magnetic response and compared it to the forward magnetic responses of the borehole samples ( $\chi_{BH}$ ) and susceptibilities of MVI ( $\chi_{MVI}$ ). The forward calculations provide an indirect way to explore the link between the physical properties. The calculated results (Figure 2.11) support an existent underlying relationship between the IP chargeabilities and magnetic susceptibilities. The IP-driven magnetic response after reduction to pole ( $RTP_{IP}$  in Figure 2.11a) shows a NW-SE structure, very similar to the observed magnetic field after reduction to pole (color map in Figure 2.11b). The contours in Figure 2.11b also represents forward response of the MVI. The magnetic field calculated from borehole susceptibility values (in Figure 2.11c) also shows a similar NW-SE pattern.

The cooperative magnetic-DC/IP inversion strategy is presented schematically in Figure 2.12. In the first stage, DC/IP and magnetic total field intensity (TFI) data are inverted separately to obtain a 3D chargeability model in the form of a scalar voxel ( $m$ ), and a magnetization vector voxel that is the output of an unconstrained MVI (after four IRI). Then, an IP-driven susceptibility voxel ( $\chi_{IP}$ ) is prepared by scaling the IP values from zero to 0.1 SI. In parallel, a total susceptibility voxel ( $\chi_{Total}$ ) is also calculated from the magnetization vector voxel (Equation II.3).

The surface magnetic field responses of these 3D susceptibility models are calculated through conventional 3D forward modeling. After reduction to pole ( $RTP$ ) filtering, the two magnetic field responses ( $RTP_{IP}$  and  $RTP_{MVI}$ ) are compared to each other. This comparison aims to determine how much information could come from DC/IP inversion in the cooperative inversion.



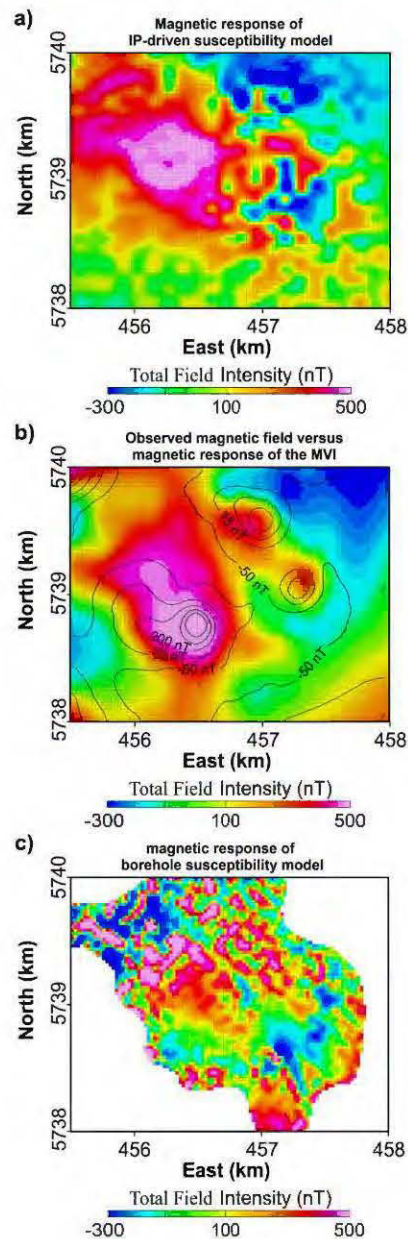


**Figure 2.11** Indirect evidence of a link between the underlying physical properties of rocks. (a) Forward magnetic response of the IP-driven susceptibility model. (b) Forward magnetic response of the MVI susceptibility model (contours) overlaid on the observed residual magnetic field. (c) Forward magnetic response of the borehole susceptibility model. All magnetic field responses are reduced to the magnetic pole for centralization of the anomaly picks.



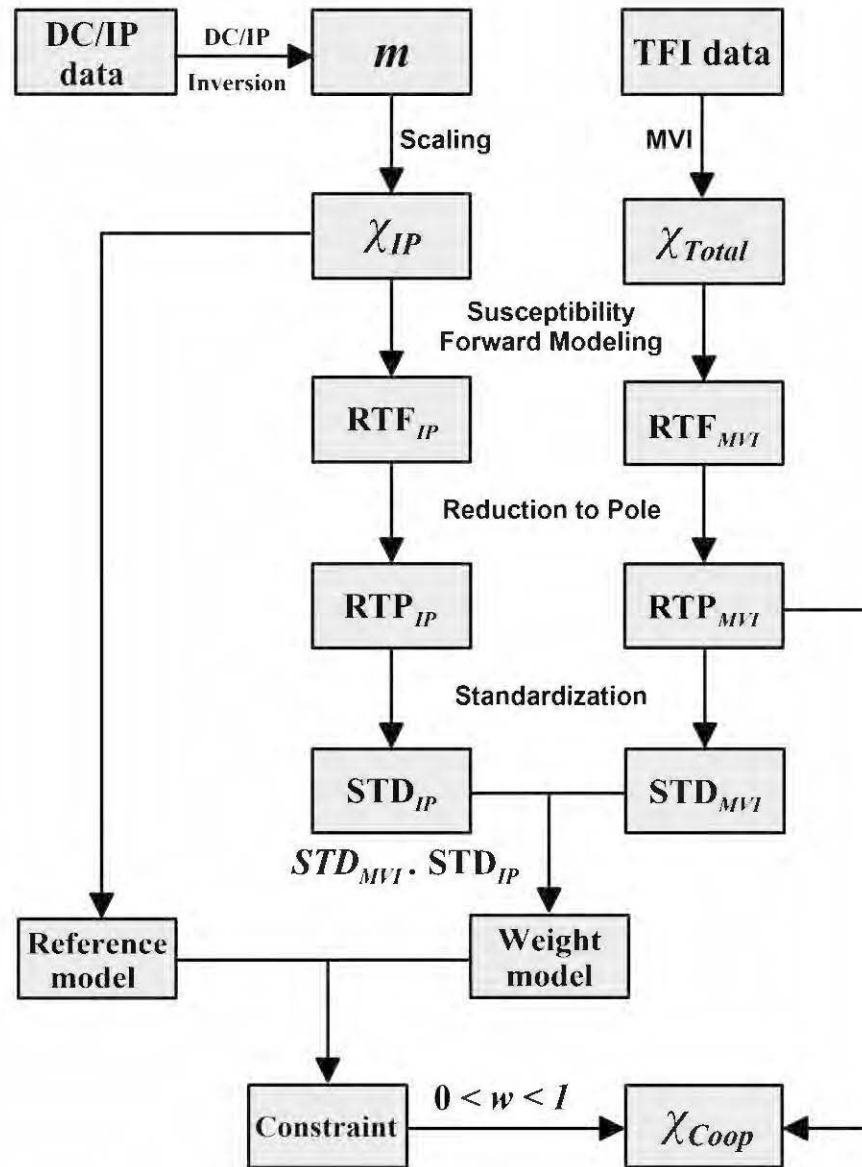


**Figure 2.12** Cooperative magnetic-DC/IP inversion workflow.

The output of this comparison is a weight model that in conjunction with a reference model (IP-driven susceptibility,  $\chi_{IP}$ ), prepare a cooperative constraint on the susceptibility inversion of the  $RTP_{MVI}$  data.

In regions with similar  $RTP_{IP}$  and  $RTP_{MVI}$  responses (Figures 2.11a and 2.11b), the DC/IP inversion has more contribution in the cooperative inversion. We used a similarity measure based on the multiplication of the standardized magnetic responses of the DC/IP chargeabilities ( $STD_{IP}$ ) and MVI susceptibilities ( $STD_{MVI}$ ). Standardization rescales the 2D RTP images to have a mean of zero and a standard deviation of one. When  $STD_{IP}$  is multiplied by the  $STD_{MVI}$ , the result (the inner product) intensify the similar field responses and weakens the dissimilar field responses. The resulting 2D grid values are then normalized from zero to one and are multiplied by a 3D unit voxel of the same size of the inversion project to create a 3D weight model.

We then apply the weight model and the reference model to constrain the inversion of the magnetic response of the MVI ( $STD_{MVI}$ ). To avoid the inversion tends too much toward the IP-driven susceptibility or MVI models, two scenarios are tested in the cooperative inversion:

1) Cooperative magnetic-DC/IP inversion with uniform weight model:

In this case, we merely assume the influence of the IP-driven model on the cooperative inversion is evenly distributed in X and Y directions. In each inversion implementation, a constant global weight ( $0 < w < 1$ ), determines the balance of information flow from the DC/IP inversion to the cooperative inversion. When  $w = 1$ , the IP-driven model and the resulting cooperative susceptibility model ( $\chi_{Coop}$ ) are equivalent, and when  $w = 0$ , the influence of DC/IP inversion is zero, and the cooperative inversion is equivalent to

an unconstrained inversion. We seek an optimum global weight ( $w$ ) that results in a reasonable trade-off between the IP-driven reference model and  $RTP_{MVI}$ .

2) Cooperative magnetic-DC/IP inversion with non-uniform weight model:

In this case, we consider that the influence of the IP-driven model on the cooperative inversion is not evenly distributed in X and Y directions. The weight model is shown in Figure 2.13 as a horizontal slice.

The regions with higher weights (red) indicate that the underlying DC/IP chargeability distributions in those regions produce similar magnetic field responses ( $RTP_{IP}$ ) compared to the magnetic field responses of the MVI susceptibilities ( $RTP_{MVI}$ ).

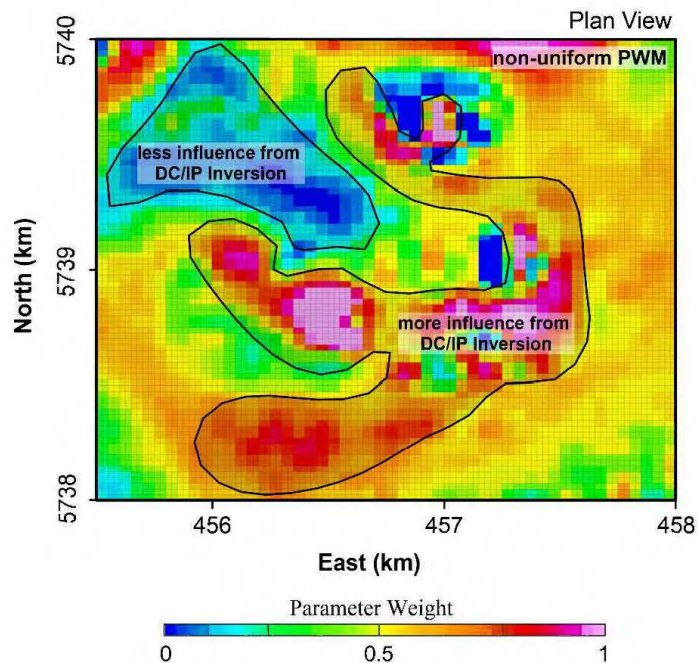


**Figure 2.13** A horizontal slice of the calculated weight model.

Therefore, in regions with higher weights, we expect more reliable susceptibility reconstruction by the cooperative inversion. Smaller weights (blue colors in Figure 2.13) reduce the cooperation of the DC/IP chargeabilities on the susceptibility reconstruction, and inversion is forced to estimate the susceptibility distribution from the calculated surface magnetic anomalies. Again, a constant global weight ( $0 < w < 1$ ), determines the balance of information flow from the non-uniformly weighted DC/IP inversion or the  $RTP_{MVI}$  to the cooperative inversion. When global weight ( $w$ ) is close to zero, the influence of DC/IP results are reduced, and the non-uniform cooperative inversion is equivalent to an unconstrained MVI inversion.

Compared to the unconstrained inversion results (Figure 2.7), introducing a uniformly distributed DC/IP chargeability constraint resulted in an acceptable estimation of the high magnetic mafic volcanic rocks and dioritic intrusions (Figures 2.14a, 2.14b, and 2.14c). However, the low susceptibilities, associated with Au-rich zone are partially imaged and disappear by reducing the global weight to  $w = 0.001$  (Figure 2.14c).

The non-uniform weighting resulted in better localization of the low magnetic Au-rich zone as it was observed in the borehole susceptibility model. The felsic volcanic rocks and porphyritic intrusions at the center of deposit show low susceptibilities that are surrounded by a ring of high magnetic mafic volcanic rocks. The diorite intrusion is also imaged as a large magnetic-high in the northwest. The best results came from  $w = 0.01$ , where the Au-rich zone is localized as a low susceptibility anomaly.

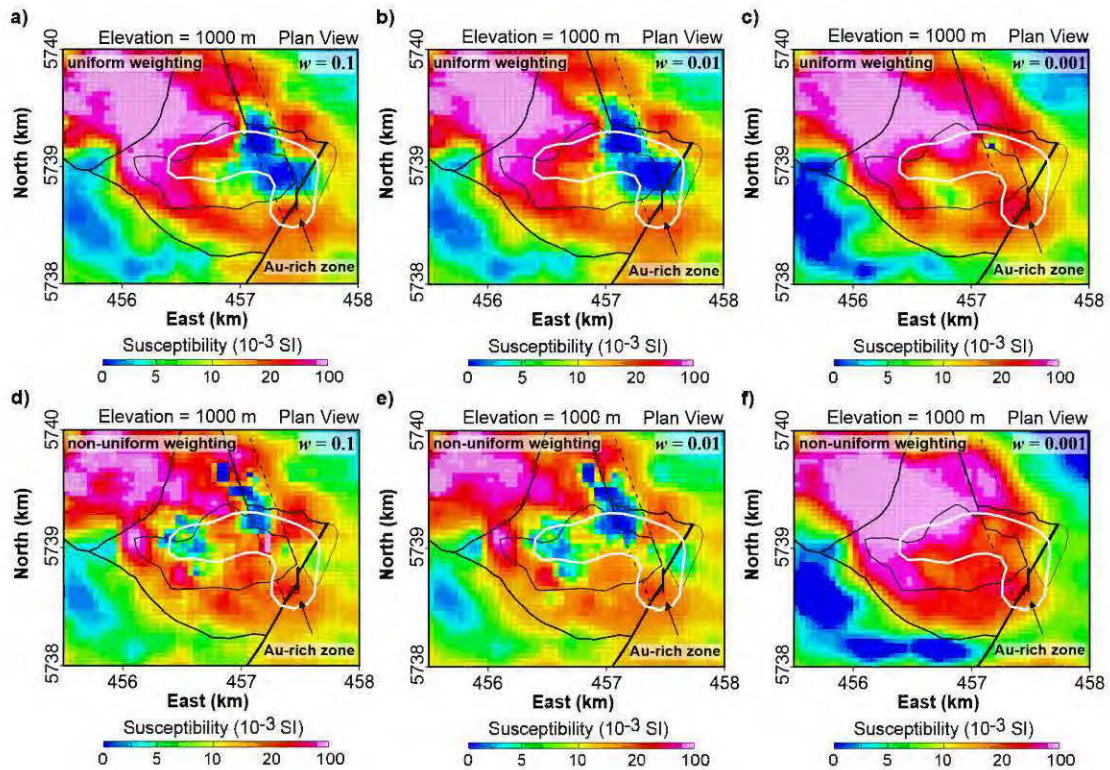


**Figure 2.14** Cooperative inversion results with different weighting scenarios. (a, b and c) Cooperative susceptibilities with uniform weighting. (d, e and f) Cooperative susceptibilities with non-uniform weighting. The global weight ( $w$ ) is reduced from 0.1 to 0.001 in each scenario. Outline of Au mineralization is shown in the white contour. Bedrock geology is overlaid on both slices.

The unconstrained and cooperative susceptibility results are evaluated by measured susceptibilities of borehole samples in Figure 2.15. The cooperative inversion resulted in a much better estimation of susceptibility distribution. The correlation between modeled and borehole susceptibility values is increased from 0.125 in the unconstrained MVI to 0.525 in the cooperative inversion.

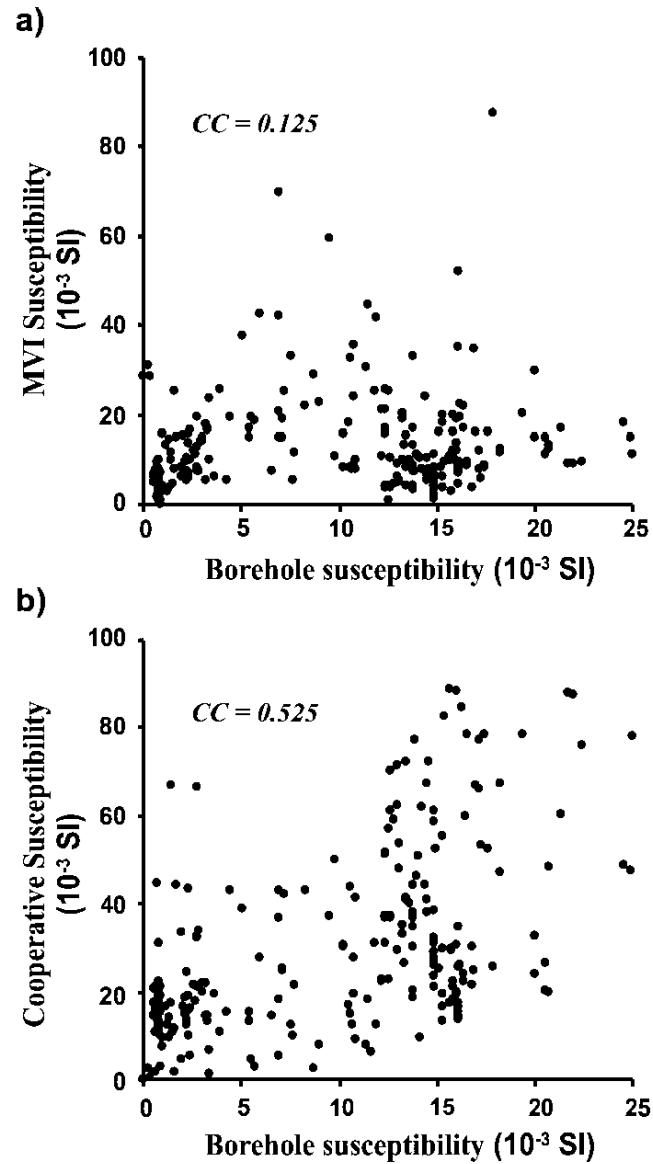


**Figure 2.15** Evaluation of inverted susceptibilities. (a) Unconstrained MVI susceptibilities versus borehole susceptibilities. (b) Susceptibility model from non-uniform cooperative inversion ( $w = 0.01$ ) versus borehole susceptibilities. CC indicates correlation coefficient.



Figure 2.16 presents a 3D view of the non-uniform cooperative inversion result for  $w = 0.01$ . The high magnetic anomaly (wireframed) is related to a larger zone of the hydrothermal alteration mostly associated with mafic volcanic rocks with overprints of propylitic alteration and later developed dioritic intrusions. The confined low magnetic zone within the high magnetic zone is related to the felsic volcanic rocks and porphyritic intrusions and destructive magnetite / quartz-sericitic alteration (host of Au).

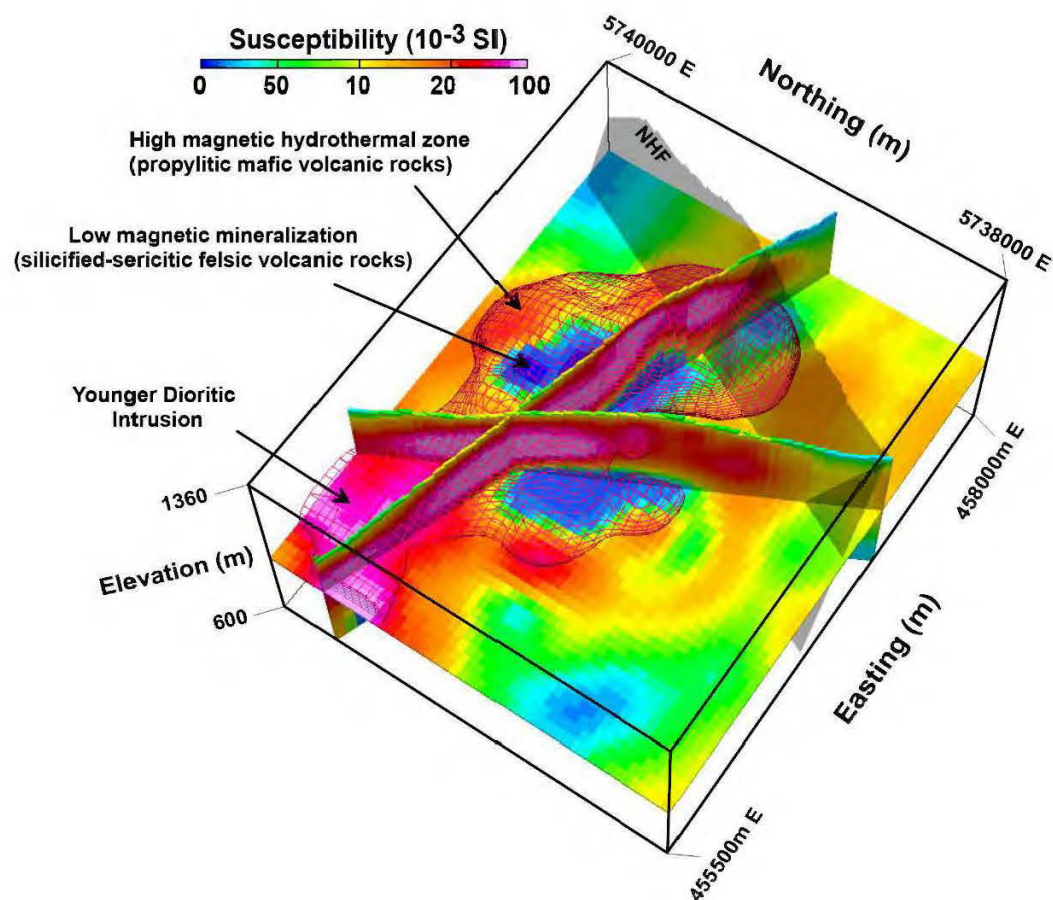


**Figure 2.16** The 3D view of cooperative inversion results. The red wireframe indicates the high magnetic zone which confines a low magnetic mineralized zone within itself. The NHF cross-cuts the eastern portion of the low magnetic zone.

## 2.8 Conclusion

Magnetization vector inversion is used to recover the vector properties of rocks' magnetizations rather than the scalar susceptibility distributions. Utilization of sharp inversion methods in both MVI and DC/IP inversions also recovered the high-contrast variations of the subsurface physical properties. The tuning of the sharpness by modifying the reweighting in MVI, and the trade-off between the  $l^1$ -norm and  $l^2$ -norm in DC/IP modeling implies the importance of inversion parametrization in the recovery of consistent physical property models. The modeled physical properties on the prospect scale showed a hydrothermal structure with a NW-SE trending low resistivity and high chargeability/susceptibility zone.

On deposit scale, the recovered resistivity model showed a moderately resistive zone inside the NW-SE conductive zone with low chargeabilities, and this confirmed the hypothesis that a localized high resistivity / low chargeability zone is associated with devitrification process and pore spaces filled with quartz in the Au-rich zone. The accuracy of DC/IP inversion in the localization of this Au-rich zone provided a valuable constraint on the magnetic inversion on the deposit scale, for better localization of the low susceptibility zone associated with mineralization.

The interrelationship between physical properties made it possible to run cooperative inversion of multiple data sets. The chargeability results in this study were used to constrain the magnetic inversion. The recovered cooperative susceptibilities successfully located the magnetite destructive zone associated with the Au enrichments. The value of this methodology is that it does not necessarily need any prior information for physical property coupling. The coupling between susceptibilities and chargeabilities (or any other types of physical properties) can be tested through calculation of forward responses of them. We emphasize that the way we incorporate



the cooperative constraint has crucial importance to the final reconstruction of the cooperative physical property. The fact that the influence of the DC/IP inversion on the cooperative inversion was not evenly distributed in X and Y directions led us to recover a more consistent susceptibility image through non-uniform weighting of the chargeability constraint. Places with more similarities between the magnetic responses of IP and MVI were forced to get susceptibility information from DC/IP inversion rather than MVI forward response. The procedure allowed the useful parts of the DC/IP inversion to participate in the reconstruction of the cooperative susceptibility. This methodology is potentially reproducible in cooperative inversion between other geophysical methods with slight modifications. The value of this procedure is that the entire spatial domain of incorporated physical properties does not need to have perfect coupling. The non-uniform weighting process will let the useful parts of each physical property model to participate in the reconstruction of the other physical property model.

## 2.9 Acknowledgments

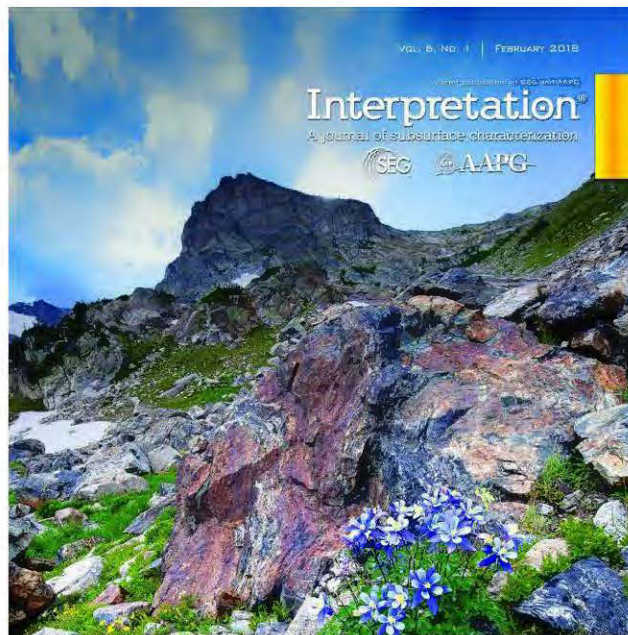
This work is funded by a Strategic Projects Grant from the Natural Sciences and Engineering Research Council of Canada with industry partners Amarc Resources Ltd., Geotech Ltd., Gerald G. Carlson, and John A. Chapman. Amarc Resources Ltd. is particularly thanked for providing access to drillcore and geophysical data; Geotech Ltd. is acknowledged for the collection of the aeromagnetic data as well as valuable discussions with us through the project. We also thank Walcott Geoscience for collecting IP-DC resistivity data and in-field assistance.

## CHAPTER III

### GEOPHYSICAL PROPERTIES OF AN EPITHERMAL AU-AG DEPOSIT IN BRITISH COLUMBIA, CANADA

Bahman Abbassi, Li Zhen Cheng, Jeremy P. Richards, Juliane Hübert, Jean M.  
Legault, Mark Rebagliati and Ken Witherly

This paper appears in *Interpretation*, Volume 6, Issue 4, T907-T918



<https://library.seg.org/doi/abs/10.1190/int-2017-0232.1>

## Résumé

Le gisement Newton Au-Ag est un système épithermal de sulfuration intermédiaire en Colombie-Britannique (Canada). Les données géophysiques multiples sont interprétées et évaluées par des observations pétrophysiques, géochimiques et géologiques de forage afin d'améliorer notre compréhension du système épithermal de Newton en termes de signatures géophysiques. Les jeux de données de rayons  $\gamma$  aéroportés ont montré des comptes d'émission élevés de K, eTh et eU sur le dépôt de Newton, en raison de l'altération hydrothermale. Les mesures de rayons  $\gamma$  de forage montrent également des concentrations élevées de potassium liées aux phyllosilicates riches en K sous la forme d'assemblages d'altération argileux et de quartz-séricite. L'inversion de vecteur d'aimantation (IVA) est utilisée pour récupérer un modèle de vecteur d'aimantation 3D non contrainte du système sur des échelles régionales et de dépôts. Le IVA régional a découvert une zone magnétique basse concentrique profonde qui peut être interprétée comme un système porphyrique sous-jacent sous le dépôt épithermal. À l'échelle du dépôt, l'inversion de résistivité PP / CC et la IVA non contrainte ont révélé plus de détails sur le système épithermal. L'inversion de résistivité magnétique PP / CC coopérative à l'échelle du dépôt a contraint le modèle de susceptibilité magnétique à récupérer une image de susceptibilité plus précise du système épithermal qui est bien adaptée à la géologie du forage. L'interprétation intégrée a identifié quatre domaines pétrophysiques basés sur les trois propriétés physiques inversées en coopération, y compris la résistivité électrique, la chargeabilité PP et la susceptibilité magnétique.

## Abstract

Newton Au-Ag deposit is an intermediate sulfidation epithermal system in British Columbia, Canada. Multiple geophysical data are interpreted and evaluated by drillcore petrophysical, geochemical and geological observations to increase our understanding of the Newton epithermal system in terms of its geophysical signatures. Airborne  $\gamma$ -ray datasets showed elevated emission counts of K, eTh, and eU over the Newton deposit due to hydrothermal alteration. Drillcore  $\gamma$ -ray measurements also show high potassium concentrations related to the K-rich phyllosilicates in the form of argillic and quartz-sericite alteration assemblages. Magnetization vector inversion (MVI) is used to recover an unconstrained 3D magnetization vector model of the system on regional and deposit scales. The regional MVI has uncovered a deep concentric low magnetic zone that can be interpreted as an underlying porphyry system beneath the epithermal deposit. At deposit scale, 3D IP (induced polarization)-DC resistivity inversion and unconstrained MVI revealed more details of the epithermal system. Cooperative magnetic-IP-DC resistivity inversion at deposit scale constrained the magnetic susceptibility model and recovered a more precise susceptibility image of the epithermal system that is well-matched with borehole geology. The integrated interpretation identified four petrophysical domains based on the three cooperatively inverted physical properties, including electrical resistivity, IP chargeability, and magnetic susceptibility.

### 3.1 Introduction

Shallow (< 1.5 km) hydrothermal deposits formed at depths below boiling hot springs (< 300 °C) are commonly referred to as epithermal deposits (Simmons et al., 2005; Pirajno, 2009). The Newton epithermal system consists of hydrothermal disseminations of Au and Ag as inclusions in pyrite with variable amounts of Cu mineralization in British Columbia, Canada (Figure 3.1). Based on sulfidation states, the Newton epithermal deposit is characterized as an intermediate sulfidation type in which sulfur and oxygen fugacities are gradational between low sulfidation and high sulfidation regime (Pressacco, 2012; McClenaghan, 2013). The epithermal system is hidden within a very complex geological context covered under quaternary sediments and vegetations. In this study, we present a 3D integrated geophysical model of the Newton epithermal deposit that reconciles all geophysical, petrophysical and geological observations from regional to deposit scales.

Similar epithermal types of mineralization around the world are commonly accompanied either by (1) quartz veins, or (2) disseminated sulfides, which cause significant contrasts in physical properties between the mineralization and the background rocks (Allis, 1990; Irvine and Smith, 1990; Feebreyf et al., 1998; Murakami, 2008; Morrell et al., 2011; Clark, 2014; Hübner et al., 2016; Legault et al., 2016). Relatively cool CO<sub>2</sub>-bearing hydrothermal fluids in epithermal systems usually destroy magnetite and cause demagnetization anomalies (Allis, 1990; Murakami, 2008; Clark, 2014). The late-stage volcanic flows after the epithermal mineralization may obscure the deeper demagnetization zones (Allis, 1990), and in some cases, like on Olkaria system in the rift valleys of Kenya, the demagnetization is extending to 4 km depth (Allis, 1990). Electrical resistivity-highs (locally exceeding 1000 Ohm-m) are associated with silicification, compaction, and intermediate-to-felsic intrusions (Allis, 1990). Low resistivities, from sulfidation, which are most favorable to hydrothermal

exploration, are often mixed with resistivity-lows of pore fluid and pervasive clay alteration (Allis, 1990). Strong IP chargeabilities due to hydrothermal alteration are typically associated with the presence of disseminated sulfidation (Sumner, 1976). Alteration haloes over epithermal Au-Ag deposits are also detected through  $\gamma$ -ray surveys by Irvine and Smith (1990); Feebrey et al. (1998) and Morrell et al., (2011). Radiometric data from the Waihi-Waitekauri epithermal Au-Ag deposit in New Zealand shows widespread potassium enrichment related to K-rich phyllosilicates in the core of the epithermal alteration zones (Morrell et al., 2011).

Explorations in the Newton area have been conducted since the 1970s and comprise geological and geochemical observations and geophysical measurements (Pressacco, 2012). The most recent study (Hübert et al., 2016) has modeled regional electrical resistivity structure of the Newton deposit using magnetotelluric (MT) and airborne z-axis tipper electromagnetic (ZTEM) data. The area of hydrothermal mineralization exhibits a modest electrical response relative to the country rocks, mainly due to the presence of phyllosilicate minerals (sericite) and minor epithermal sulfides (Hübert et al., 2016). However, the ZTEM-MT resistivities do not possess the resolution of the deposit scale electrical features. A cooperative inversion method is also introduced earlier by Abbassi et al. (2018a), to produce an enhanced magnetic susceptibility model which is proved to be compatible with the known deposit scale geological information (Abbassi et al., 2018a).

In this study, results of multiple geophysical measurements and inversions are presented in two subsequent scales over the Newton deposit to increase the understanding of the epithermal system. Our objective was to cover the 3D volume of the hydrothermal system from near surface to 5 km depth and to integrate all available geophysical, petrophysical and geological information in a multi-layer/multi-scale 3D integrated interpretation.

### 3.2 Geological setting

#### 3.2.1 Regional geology

Radiometric dating of molybdenite within the Newton epithermal Au-Ag deposit yielded a Late Cretaceous age of  $72.1 \pm 0.3$  Ma (McClenaghan, 2013) in association with arc magmatism in the accreted Stikinia terrane of western Canada (Figure 3.1). Amarc Resources Ltd. acquired the property in 2009, and after an extensive drilling campaign defined an estimated inferred mineral resource of 111.5 Mt with an average grade of 0.44 g/t Au (cut-off at 0.25 g/t Au; Pressacco 2012).

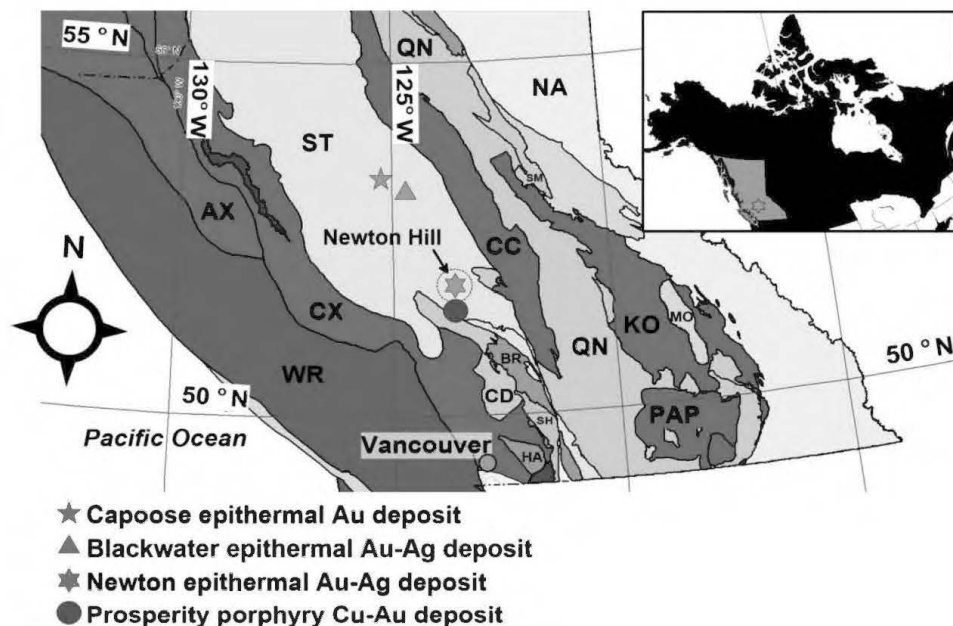


**Figure 3.1** Several large porphyry and epithermal deposits located in Stikinia terrain (ST) in central British Columbia. Other terranes are: Alexander terrane (AX); Bridge River terrane (BR); Caribo terrane (CAC); Cache Creek terrane (CC); Cadwallader terrane (CD); Coast Complex terrane (CX); Harrison terrane (HA); Kootenay Terrane (KO); Monashee (MO); Cratonal North America terrane (NA); Nisling terrane (NI); Post Accretionary Plutons (PAP); Quesnellia terrane (QN); Shuksan terrane (SH); Slide Mountain Terrane (SM); Wrangellia (WR). Modified from Massey et al. (2005).



Regionally (Figure 3.2), the Late Cretaceous volcanic sequence is overlain by Miocene-Pliocene Chilcotin Group flood basalts, and Quaternary glacial deposits, which are variably eroded to expose the older rocks. The epithermal mineralization associated with the Newton deposit is at a depth of ~50 m to ~600 m and is characterized by pervasive sericitic (phyllic) alteration containing disseminated pyrite with Au inclusions in coeval intermediate composition porphyritic volcanic and subvolcanic intrusive rocks. Au-Ag mineralization is associated with disseminated pyrite, marcasite, and base metal sulfides (McClenaghan, 2013; Liu et al., 2015).

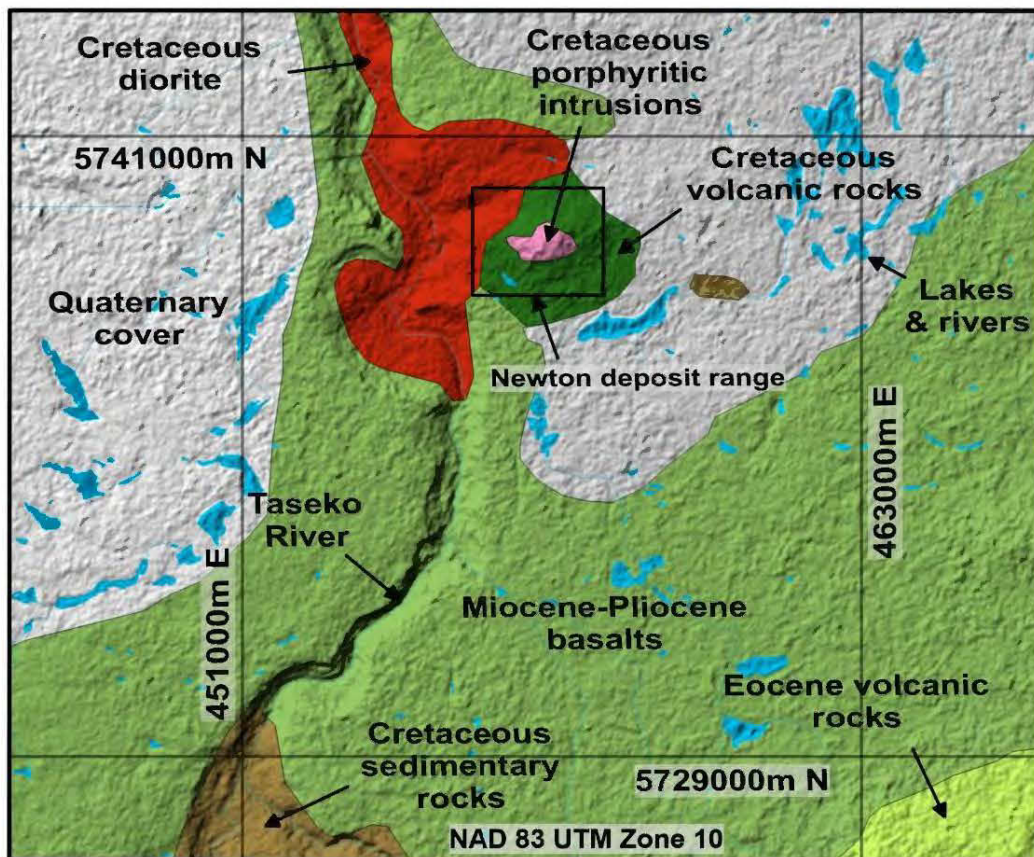


**Figure 3.2** Regional geological features of Newton area modified after British Columbia Geological Survey Geoscience Map (mapplace.ca). Geology is draped on shaded relief topography.

### 3.2.2 Deposit scale bedrock geology

Quaternary glacial tills cover most of the Newton property. Consequently, deposit scale geological information has primarily been obtained from drill cores (Pressacco, 2012). A bedrock geology map of the property is compiled from the mapping of limited outcrops, drill cores and cross-section interpretations (Figure 3.3). Three layered volcano-sedimentary sequences overlain on each other from bottom to top are mafic volcanic rocks, sedimentary rocks and felsic volcanic rocks ( $72.1 \pm 0.6$  Ma; McClenaghan, 2013). The layered rocks are intruded by intermediate-to-felsic porphyritic intrusions, including the monzonite ( $72.1 \pm 0.3$  Ma; McClenaghan, 2013), quartz feldspar porphyry (QFP;  $70.9 \pm 0.5$  Ma; McClenaghan, 2013), feldspar biotite porphyry (FBP) and diorite ( $69.3 \pm 0.4$  Ma; Liu et al., 2015).

### 3.3 Borehole geology and petrophysics

#### 3.3.1 3D lithology and hydrothermal alteration model

Based on a database of 130 boreholes comprising a total of 1537 samples (Amarc written communications; Pressacco, 2012), a 3D lithological model is constructed for the Newton property. A cross-section of the 3D model is shown in Figure 3.4a. As can be seen, the laterally discontinuous volcanic sequences are intruded by several phases of intermediate-to-felsic intrusions. The deposit is offset by the Newton Hill Fault (NHF), which displaces the geology and mineralization by  $\sim 300$  m of normal dip-slip movement.

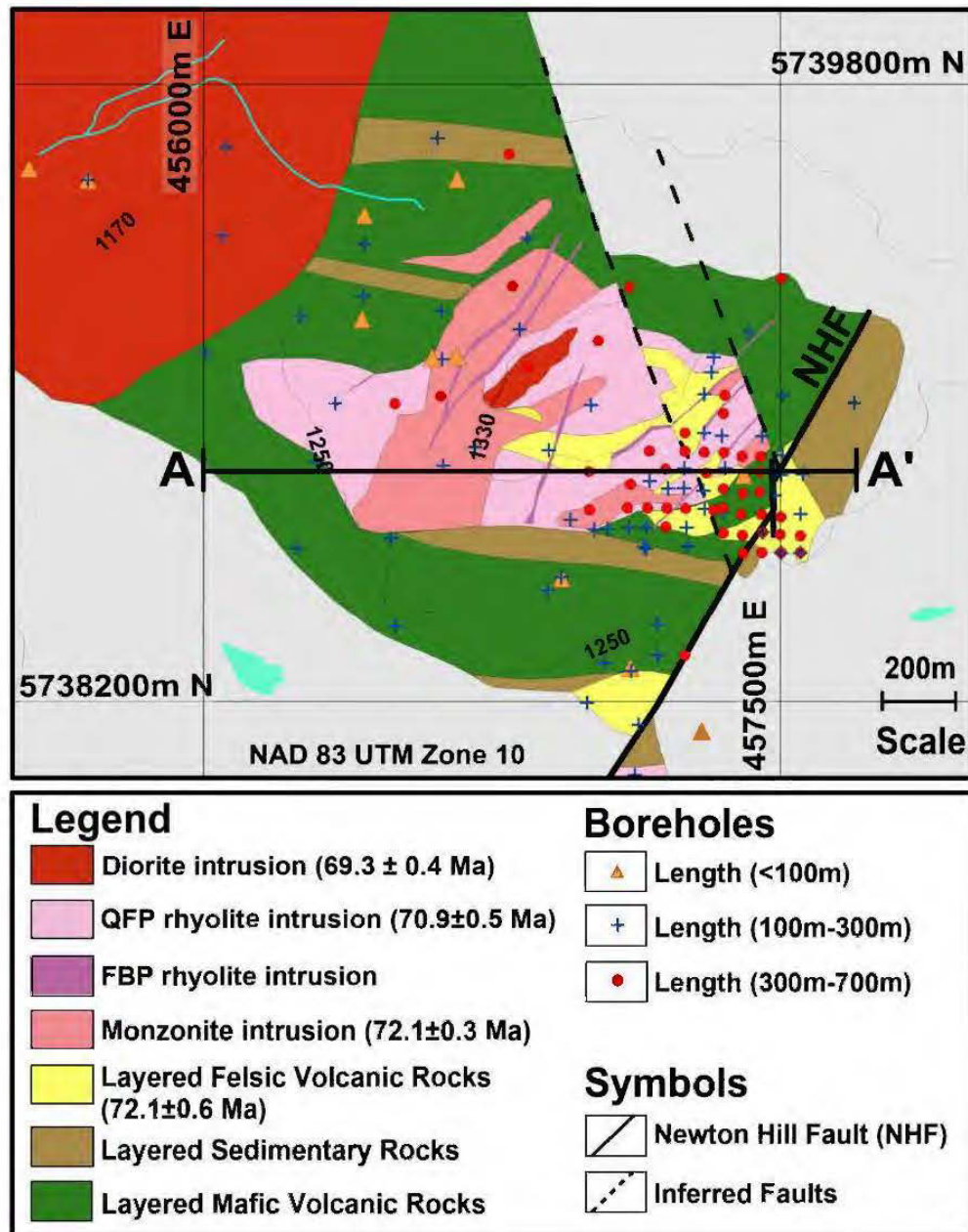


**Figure 3.3** Bedrock geology map at the deposit scale. Colored dots indicate drillhole locations with various total lengths. The light gray parts are undefined regions due to the lack of borehole information in the periphery of the deposit. Contours indicate topography.

Based on the geochemical assessment from the database of Amarc and previous works of McClenaghan (2013) and Liu et al. (2015), a 3D model of hydrothermal alteration is also generated. The cross-sections of the 3D models (Figures 3.4a and 3.4b) show the highest gold contents occur mainly within the felsic volcanic sequence and in association with quartz-sericite-pyrite alteration. Propylitic alteration occurs mostly in the mafic volcanic rocks and epiclastic sedimentary units, which consists of a chlorite-epidote-calcite-albite-magnetite assemblage (Pressacco, 2012; McClenaghan, 2013). Minor potassic alteration, characterized by secondary biotite and pyrite, occurs in the diorite intrusion (Liu et al., 2015). Silicification and albitic alteration are spatially associated and are interpreted to comprise a single quartz-albite assemblage. The quartz-albite assemblage is mostly seen in QFP intrusions (Pressacco, 2012; McClenaghan, 2013). Localized argillic alteration (kaolinite-sericite-calcite) is of late stage or surficial (supergene) origin.

The Au-Ag mineralization is mainly hosted within the felsic volcanic sequence and coeval intermediate-to-felsic intrusions (monzonites, FBP and QFP). The first stage of gold mineralization with disseminated pyrite-arsenopyrite is strongly associated with a pervasive quartz-sericite alteration (Pressacco, 2012; McClenaghan, 2013). Later, the gold mineralization is associated with a quartz-sericite-marcasite alteration (McClenaghan, 2013; Liu et al., 2015). The latest mineralization consists of polymetallic sulfide veins containing pyrite, chalcopyrite, arsenopyrite, and sphalerite, but lacking gold (Liu et al., 2015).



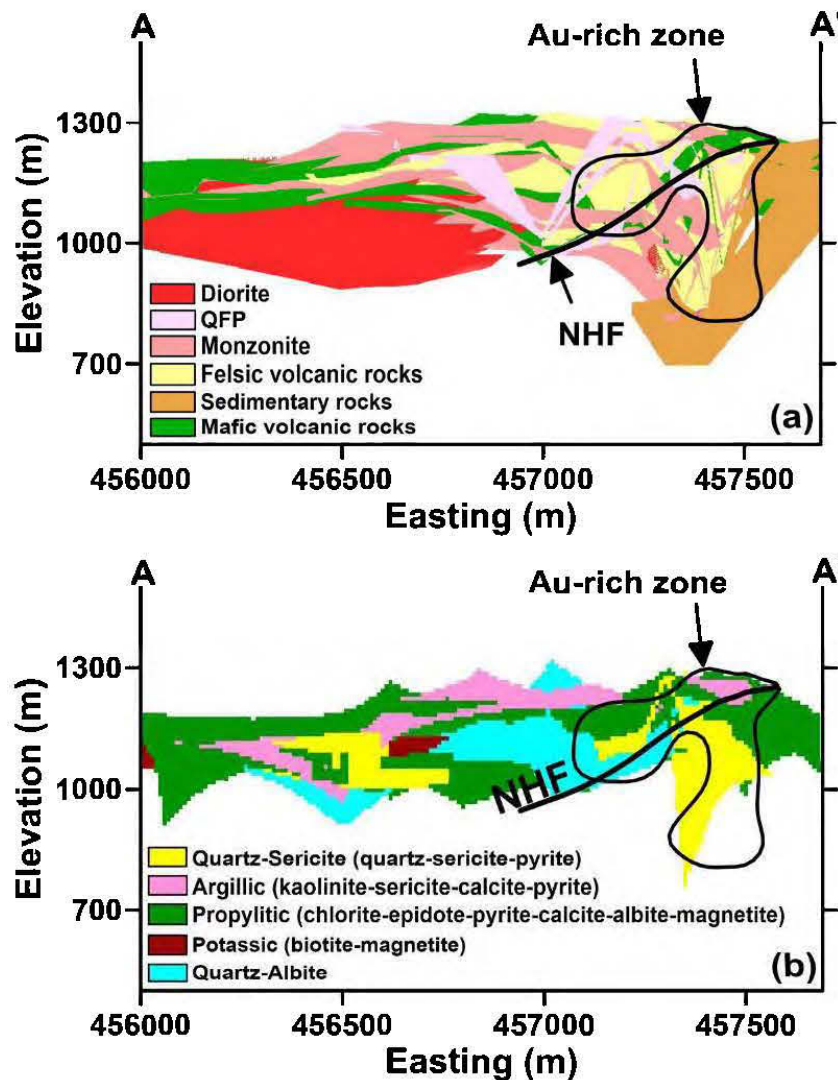


**Figure 3.4** Lithology and alteration models based on borehole data: (a) A cross-section of 3D lithology model along profile AA' in Figure 3.3 (5738800m N). (b) A cross-section of 3D alteration model along the same profile. The Newton Hill Fault (NHF) has disrupted the continuity of all lithological units and offsets the mineralized zone. The gold mineralization correlates strongly with quartz-sericite alteration, predominantly in the felsic volcanic unit.

### 3.3.2 Drillcores magnetic susceptibility and $\gamma$ -ray concentration

More than 9000 magnetic susceptibility readings are measured from core samples from 80 drillholes in the Newton Hill area. Samples are measured by KT-10 S/C meter of Terraplus Inc. and are supported by additional data provided by Amarc (Figure 3.5). The  $\gamma$ -ray spectra of 12 borehole samples (514 drillcores) are also measured using Radiation Solutions RS-125 that measures  $\gamma$ -ray emission counts in 1024 energy windows.

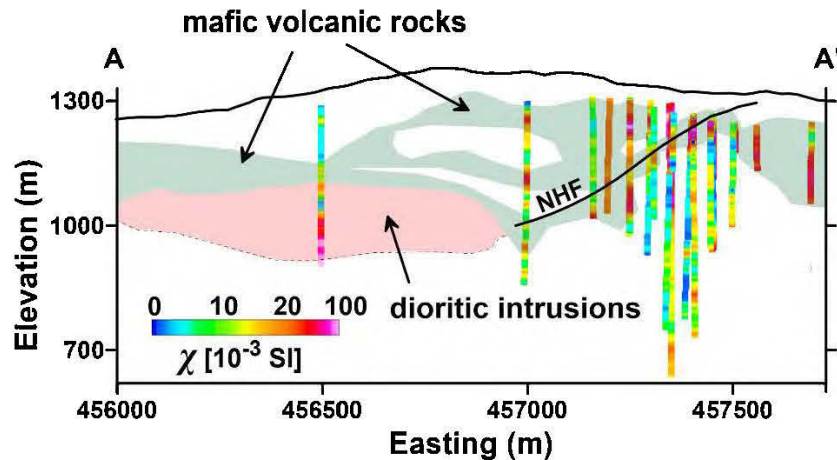


**Figure 3.5** Magnetic susceptibilities of drillcores on profile AA'. High magnetic mafic volcanic rocks and dioritic intrusions are separated from other low magnetic rocks (felsic volcanic rocks and porphyritic intrusions).

To establish a direct link between the magnetic susceptibilities,  $\gamma$ -ray concentrations, and the geology, the measured properties are classified according to lithological types and accompanying alteration assemblages. A 3D nearest-neighbor interpolation (Trauth, 2015) is used to regularize all data sets. The nearest-neighbor operation assigns susceptibility/ $\gamma$ -ray K values or lithology/alteration codes to nearest cells in the vicinity of the available data points. The advantage of this approach is that the statistical range (minimum, maximum) of the original susceptibility measurements remain intact.

However, a number of outlier samples resulted in apparently wide ranges of susceptibility/K variations (wide statistical dispersion). Therefore, a better way to rank rocks' properties is to look for the inter-quartile ranges of the data values (the interval between 25th and 75th percentiles). The retrieved statistics of measured magnetic susceptibilities and potassium radionuclide concentration of different lithologies and alteration assemblages are shown as box plots in Figures 3.6a and 3.6b.

The drillcore susceptibility measurements illustrate that there are diverse geological sources giving rise to the observed magnetic-highs. They can be listed from oldest to youngest as mafic volcanic rocks, potassic/propylitic alteration assemblages, and dioritic intrusions (Figure 3.6a). The high amplitude magnetic anomaly is likely due to a blend of mafic volcanic rocks, overprinted by magnetite bearing alterations and the later developed dioritic intrusion. However, low susceptibility sources are limited to porphyritic intrusions and the felsic volcanic rocks overprinted by quartz-sericite alteration assemblage in Au mineralization zone (Figure 3.6a).

Concentrations of all three  $\gamma$ -ray radioelements increase over the Newton epithermal system. The distribution of  $\gamma$ -ray potassium is dispersed in all lithologies due to severe chemical alteration (Figure 3.6b). Generally, K concentration reduces with an elevation of magnetic susceptibility, because of the presence of K-rich phyllosilicates in form argillic and quartz-sericite alteration assemblages in the low-magnetic epithermal mineralization zone.

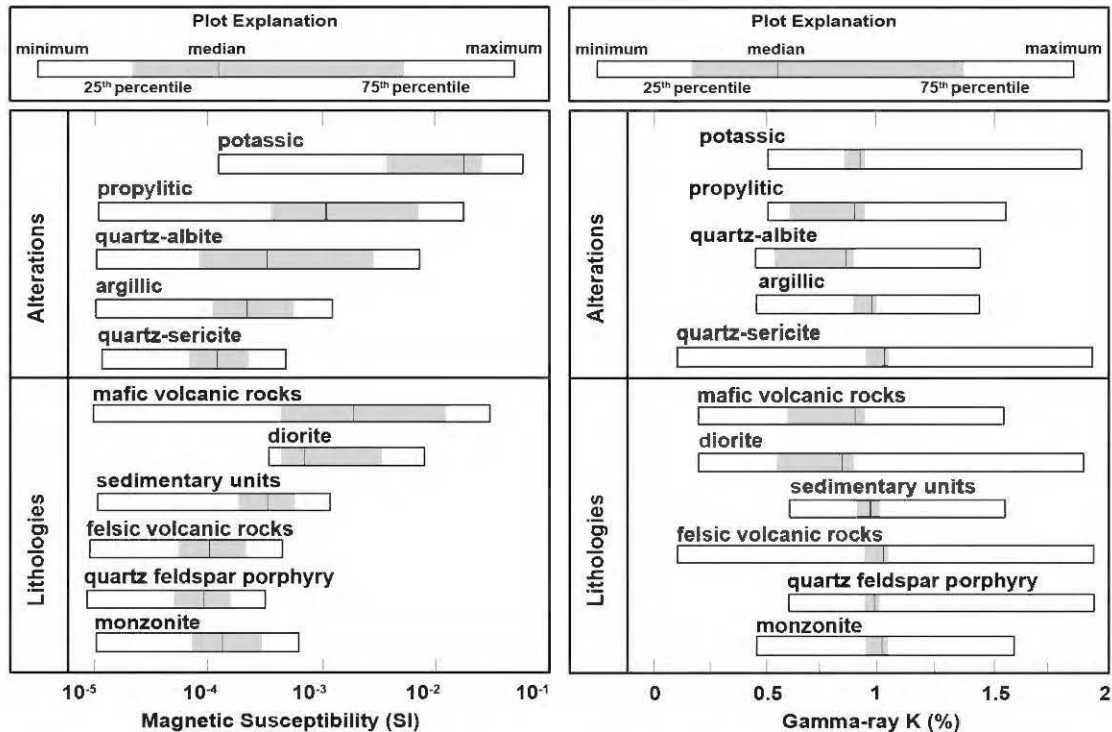


**Figure 3.6** Boxplot demonstration of measured magnetic susceptibilities and  $\gamma$ -ray potassium (K) concentrations of different lithologies and alteration assemblages. Susceptibility axis is logarithmic.

### 3.4 Geophysical datasets

Geotech Ltd. has acquired the aeromagnetic data as a part of the combined magnetic and ZTEM survey, carried out between January to February 2010, on behalf of Amarc (Geotech Ltd, 2010). The ZTEM datasets are described in Hübner et al. (2016). Total magnetic field data were measured from a helicopter flown at a mean height of 155 m above ground. The data were collected along N–S flight lines at 200 m spacing and E–W tie lines flown every ~2000 m to 500 m (tighter spacing near the deposit). A total of 7071 line-km of data were collected and cover a 1293 km<sup>2</sup> area. The magnetometer sampling rate was 0.1 second and depending on the speed of the helicopter results in approximately 10 m measurement intervals along each profile.



A previous airborne magnetic survey that covers an area of  $\sim 1100 \text{ km}^2$ , was flown in July 1993 by Geological Survey of Canada (GSC; Shives et al., 1995), using a fixed-wing aircraft at a mean height of 120 m above the ground, with E-W lines spaced  $\sim 500$  m apart, provides a regional context and are used to better characterize longer wavelengths related to the deeper magnetic sources beneath the epithermal system. The measured magnetic datasets of GSC and Amarc are shown in Figure 3.7.

The GSC dataset also contains airborne  $\gamma$ -ray measurements in the form of K-eTh-eU radionuclide concentrations. In the Figure 3.8a, the absolute values of radionuclide concentrations are displayed as red (K), green (Th) and blue (U). Figure 3.8b also present the ratios of radionuclide elements in form of ternary red (K/eTh), green (eTh/eU) and blue (eU/K) images.

An IP-DC resistivity survey of 85 line-km over Newton Hill area, using the “pole-dipole” electrode configuration was conducted in 2010 (Pressacco, 2012). The survey lines were spaced at 200 m intervals in E–W directions within the zone of hydrothermal alteration (Figure 3.7b). The dipole length was set to 100 m and 200 m, with a maximum ten times dipolar separations. The apparent chargeabilities (in mV/V) were measured by recording the decaying voltage after the current cut-off.

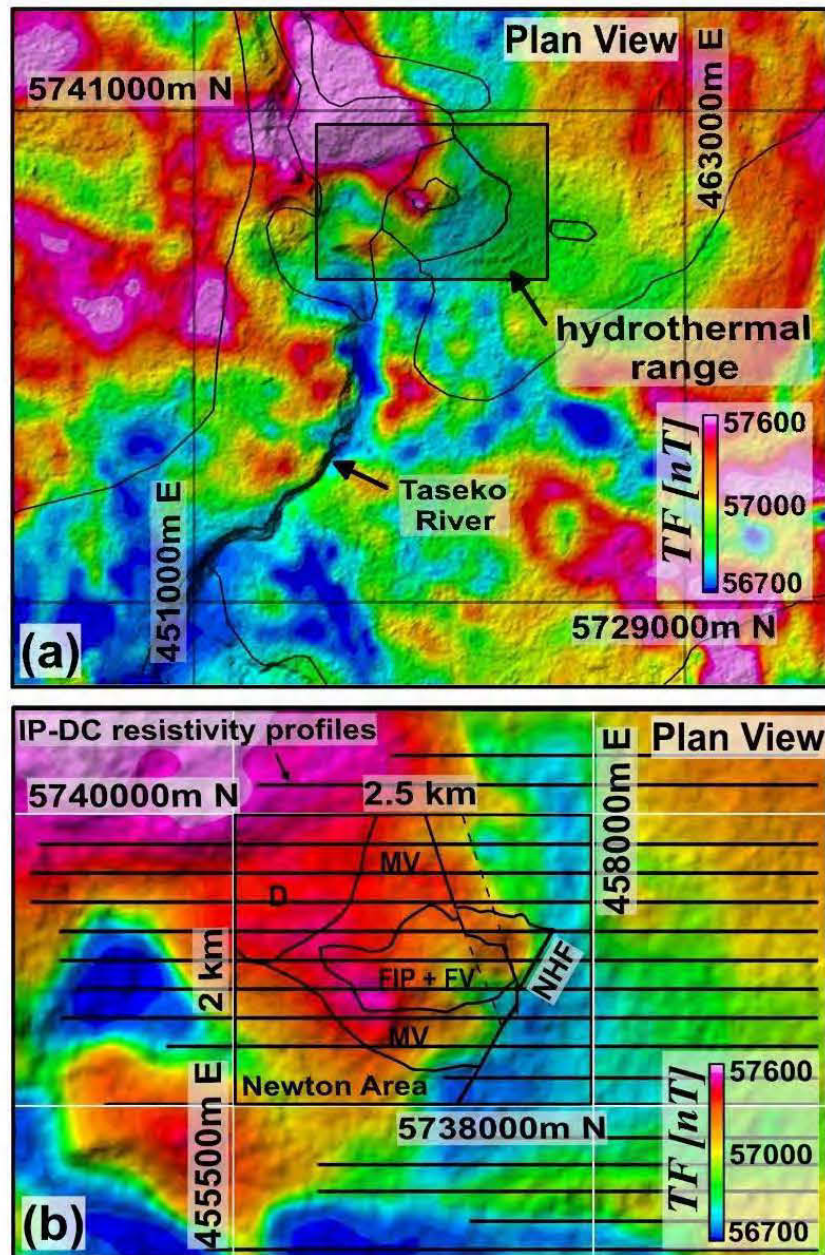


**Figure 3.7** Magnetic and IP-DC-resistivity datasets. All data are draped on a shaded relief digital elevation model (DEM) of the region: (a) Airborne total magnetic field intensities (TF) on a regional scale (GSC database). (b) Helicopter-borne total magnetic field intensities (TF) on deposit scale (Amarc dataset) together with locations of IP-DC-resistivity profiles.

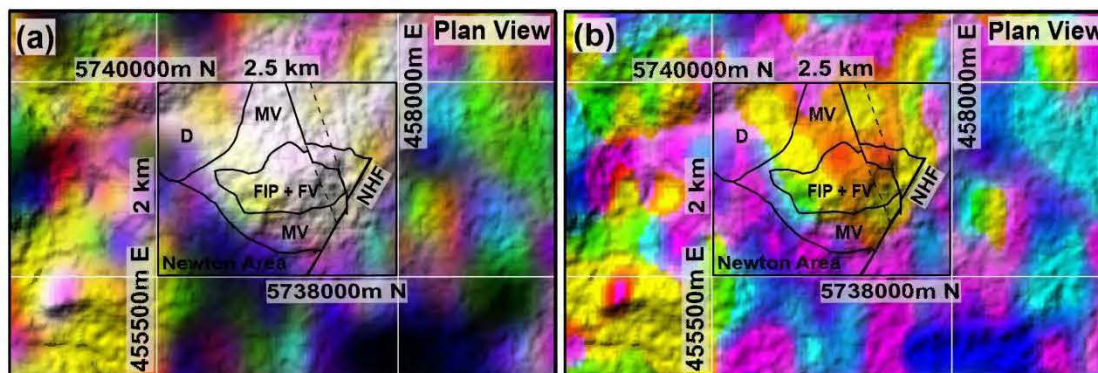


**Figure 3.8** Ternary images of airborne radiometric datasets (GSC): (a) Deposit scale RGB image of K-eTh-eU channels. White regions indicate the overlaps of all three elemental RGB channels. (b) Deposit scale RGB image of K/eTh-eTh/eU-eU/K channels.

### 3.5 Methods

#### 3.5.1 $\gamma$ -ray data interpretation

Investigation of all ratios and combination of K, eTh, and eU is a useful tool to detect the anomalous hydrothermal zones. A ternary image combination is used to produce RGB (red-green-blue) images of the radionuclides and their ratios. When all three radionuclides are abundant, the display tends towards white; otherwise, it tends towards black (Dentith and Mudge, 2014). In this study, the three radiometric channels (K, eTh, and eU) are normalized, and their histograms are equalized for enhanced RGB visualization (Figure 3.8).

#### 3.5.2 3D unconstrained magnetization vector inversion

Igneous rocks of the Newton Hill area have experienced a complicated geological history, including different phases of magmatism, hydrothermal alteration, and tectonic disruptions from the late Cretaceous to Pliocene. To consider the effect of the magnetic remanence in the Newton area, an accurate approximation proposes a vector notion of

magnetic response (total magnetization vector) as a vector summation of two vector components, including the inductive magnetization vector ( $\mathbf{J}_{Ind}^1$ ) and a remanent magnetization vector ( $\mathbf{J}_{Rem}^1$ ). Moreover, the total susceptibility of rocks in the presence of remanence will be a function of (Lelièvre and Oldenburg, 2009; Ellis et al., 2012):

$$\chi_{Total} = \left| \mathbf{J}_{Total}^1 \right| / \left| \mathbf{H}_0^1 \right| = \left| \mathbf{J}_{Ind}^1 + \mathbf{J}_{Rem}^1 \right| / \left| \mathbf{H}_0^1 \right| \quad (III.1)$$

A 3D magnetization vector inversion (MVI) is executed on the regional and deposit scales. The cell dimensions of the inversion model at the regional scale are 100 m (in X-direction), 100 m (in Y-direction) and 20 m (in Z-direction) that comprise total 2646000 cells. In the deposit scale, the cell dimensions of the inversion model are 25 m (in X-direction), 25 m (in Y-direction) and 10 m (in Z-direction) that comprise total 3148308 cells, covering the hydrothermal zone.

The MVI algorithm introduces both the amplitude and the vector direction as separate unknowns in a Tikhonov minimum gradient regularization (Lelièvre and Oldenburg, 2009; Ellis et al., 2012). An Iterative Reweighting Inversion (IRI; Geosoft Inc., 2012) method is used in parallel to the MVI modeling in this study. IRI tends to recover sharp magnetic variations, and its results are equivalent to Robust or Blocky Inversion in inverse modeling of electrical resistivity data (Claerbout, 1973; Loke et al., 2003).

### 3.5.3 3D IP-DC resistivity inversion

A 3D cooperative inversion algorithm (Loke, 2015) is employed using a modified L1-norm optimization to produce sharpened resistivity and chargeability images. Electrodes distributed initially on each node in 50 by 18 horizontal grids in X and Y direction respectively. For more accurate calculations, each cell is divided into two

parts toward East and North directions so that instead of a single cell, two cells covered the space between two adjacent electrodes in each EW-NS direction. Therefore, each cell has a 50 m by 100 m size in a horizontal plane, and they shape a large model mesh consisting of 72000 trapezoidal cells.

The IP-DC resistivity inversion considers the IP chargeability model as a small perturbation of the reference electrical conductivity model (Oldenburg and Li 1994; Li and Oldenburg, 2000). The program calculates the forward potential responses of two conductivity models separately. The forward modeling of the reference and perturbed conductivities gives the reference and perturbed potential values, from which the apparent conductivities and chargeabilities are obtainable. In each iteration, an Incomplete Gauss-Newton least-squares optimization tries to reduce the gap between measured and calculated properties by modifying the reference and perturbed conductivity values. When the calculation reaches its threshold, the modeled resistivities and chargeabilities are determined respectively.

The robust inversion in this study, which uses an extension of L2-norm and L1-norm inversions (Loke et al., 2003), incorporates two cut-off factors in the resistivity-chargeability inversion ( $k_1$  and  $k_2$ ). Larger  $k_1$  values produce smoother apparent resistivities and chargeabilities. The second cut-off factor ( $k_2$ ) shapes the modeled resistivity and chargeability outputs. The larger  $k_2$ , the smoother the predicted resistivity and chargeability values.

#### 3.5.4 3D cooperative magnetic-IP-DC resistivity inversion

Without any constraint, the inversion of magnetic data is vulnerable to the lack of depth resolution. One way to reduce the MVI uncertainty is to provide auxiliary information about the susceptibility distribution from other geophysical methods. Since the sulfide

mineralization in the area is predominantly occurred in the Cretaceous volcanic sequences, comprising interbeds of mafic rocks with a minor amount of felsic and sedimentary rocks, we expected an underlying relationship between the magnetic susceptibility of volcanic sources and IP chargeability of sulfide disseminations. Therefore, the results of the IP-DC resistivity inversion were used to constrain the subsequent magnetic susceptibility inversion. It was noticed that when the magnetization vectors of the MVI were rotated to the present geomagnetic field direction, the magnetic response of the rotated model is very similar to the magnetic response of the IP-driven susceptibilities (Abbassi et al., 2018a). Considering this underlying connection between the 3D magnetic susceptibility and IP chargeability models, the conventional susceptibility inversion (Li and Oldenburg, 1997) is constrained by the initial susceptibility information derived from IP chargeabilities.

In the cooperative inversion, four nodes between adjacent electrodes are used, so that the number of cells in the forward calculations has effectively increased to 288000 cells, and each cell, therefore, has a 25 m by 50 m size in the horizontal plane. The unit cell size for the cooperative susceptibility inversion is set to  $X = 25$  m,  $Y = 25$ , and  $Z = 10$  m, with a total number of 613800 cells, covering a smaller area limited to the mineralization zone (boreholes range). The constrained inversion set aside the less consistent equivalent solutions and narrowed down to a final solution that is well matched with the IP-DC resistivity inversion results.

### 3.6 Results

The interpretation results are presented as 3D physical property distributions, including 3D electrical resistivities ( $\rho$ ), IP chargeabilities ( $m$ ) and magnetic susceptibilities ( $\chi$ ), in three sections:

1. Regional unconstrained interpretation, comprising 3D magnetic susceptibilities of MVI.
2. Deposit scale unconstrained interpretation, covering the hydrothermal zone with elevated radioelement concentrations, with deposit scale 3D models of resistivities, chargeabilities, and MVI susceptibilities.
3. Deposit scale constrained interpretation, comprising a 3D cooperative resistivity-chargeability-susceptibility model on the Newton deposit scale, in addition to borehole geological and petrophysical observations.

#### 3.6.1 Regional unconstrained interpretation

Unconstrained MVI recovered susceptibility distributions down to 5km using GSC dataset, which helped to predict the regional magnetic field trend in the subsequent deposit scale MVI. A deep high susceptibility zone with distinct magnetization vector orientation is derived from this inversion (Figure 3.9). As can be seen in the cross-section A-A', the high susceptibility zone has a very deep root down to at least 3 km below sea level and encompasses a low magnetic zone (LMZ) within itself, with different magnetization vector orientations. The concentric shape of this LMZ might imply a hydrothermal alteration pattern related to a deeper porphyry system.



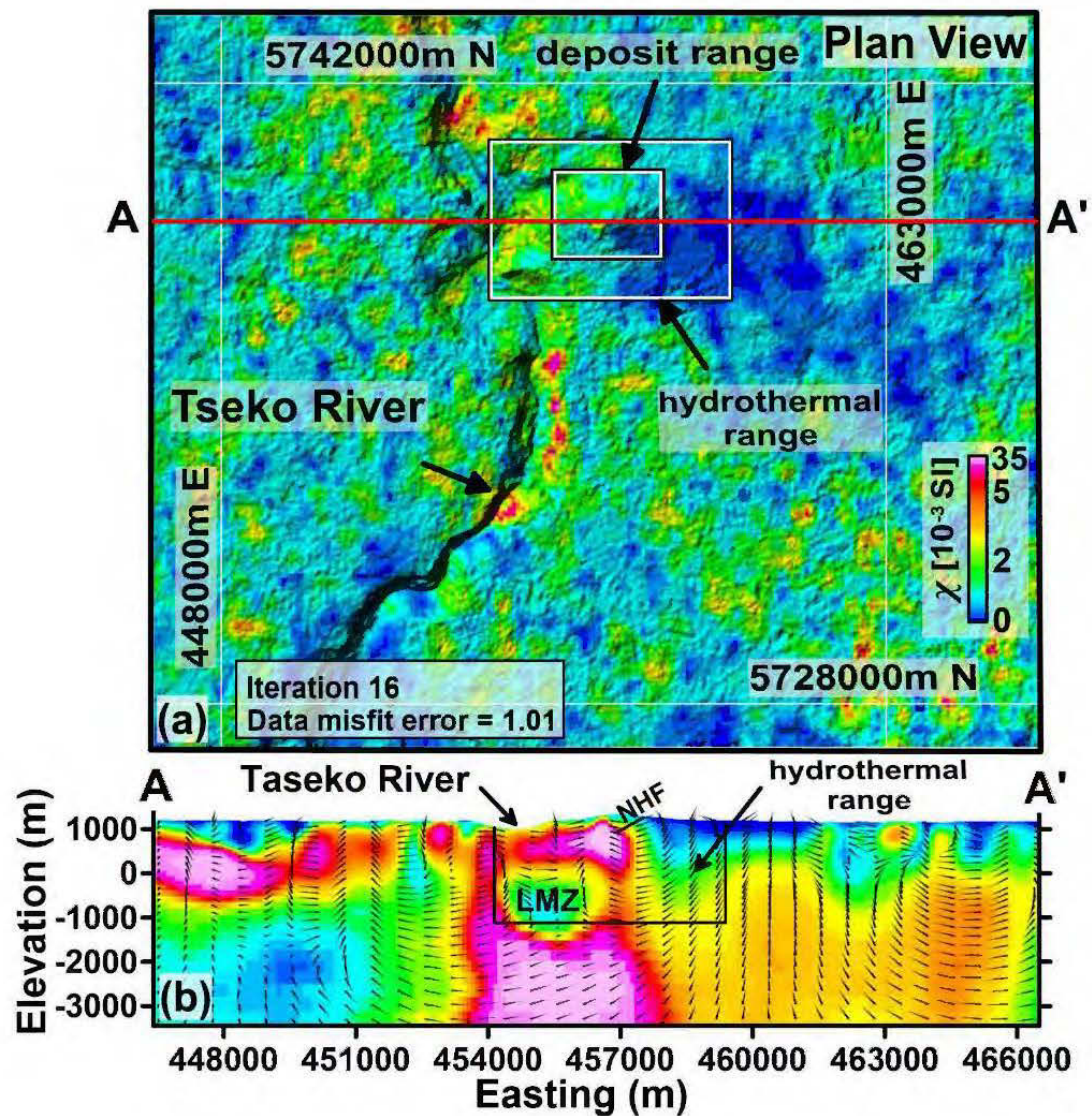


Figure 3.9 Sharp regional MVI model after four IRI focused on the high and low magnetic susceptibility zones: (a) The 3D MVI susceptibility model on a plan view (draped on shaded relief topography). (b) The 3D MVI susceptibility model cross-cut on the profiles AA' 5738800m N. Directions of magnetization vectors are overlain on the cross-section AA'. Outlines of the hydrothermal zone and Newton deposit area are shown in the rectangles.



### 3.6.2 Prospect scale unconstrained interpretation

High radionuclide concentrations are associated with bedrock exposures over Newton epithermal system due to the presence of phyllosilicates in hydrothermal alteration zone (white zones in Figure 3.8a). The RGB demonstration of radioelements ratios provides a higher resolution of variations in elemental concentrations and obviously show a northwest-southeast trend over porphyritic intrusions and felsic volcanic rocks (Fig. 8d).

Unconstrained MVI and IP-DC resistivity inversions reveal finer patterns over the area of the hydrothermal alterations. The MVI results are shown in Fig. 10. The Au-Ag-Cu-rich zone appears in a near-surface low magnetic zone. The geological context is better seen from the section view (Fig. 10c), where low magnetic susceptibilities indicate rocks on the eastern side of NHF, and igneous rocks in the west of the Newton Hill fault correspond to relatively high magnetization (Fig. 10c). The cross-section shows the likely occurrence of mafic volcanic strata overlying a deep LMZ, though the relatively thick layer of top magnetic rocks in the unconstrained inversion is not in good agreement with prior geological information.

The results of 3D prospect scale inversion of DC resistivity and IP data are illustrated in Figure 3.11 and Figure 3.12. The preliminary 2D inversions proved that the main electrical anomaly is elongated sub-vertically. However, regional geological observations show that the Cretaceous volcanic rocks and the related intrusive rocks are mostly horizontally layered. Therefore, performing smoothness horizontally could uncover the hidden anomaly sources. This is done by decreasing the vertical to horizontal flatness filter ratio ( $R_f$ ). In this study, the most stable results came out with the  $R_f = 0.2$ .

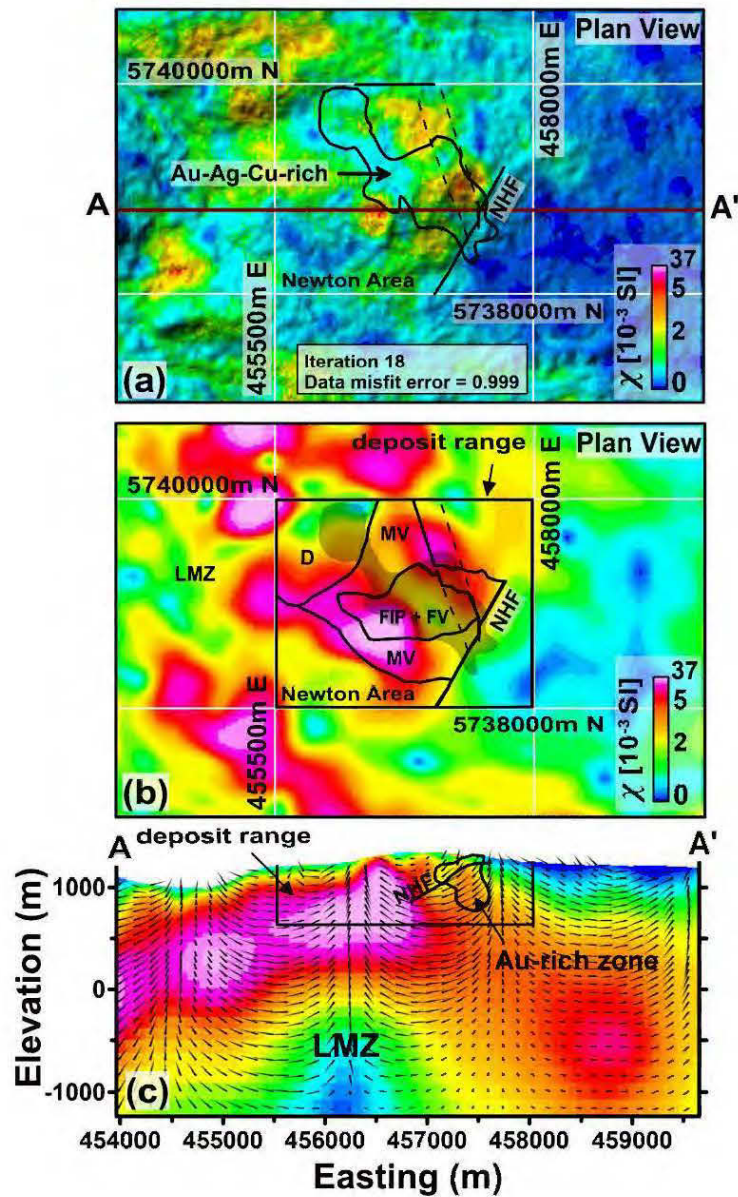


**Figure 3.10** Prospect scale unconstrained MVI model after four IRI on Amarc datasets: (a) The 3D MVI susceptibility model on a plan view draped on shaded relief topography (Outline of Au-Ag-Cu mineralization is shown in the black contour). (b) The 3D MVI susceptibility model sliced at the elevations of 1000 m (the bedrock geology is overlapped). (c) The 3D MVI susceptibility model cross-cut on the profiles AA' at 5738800m N. Directions of magnetization vectors are overlain on the cross-section AA'.

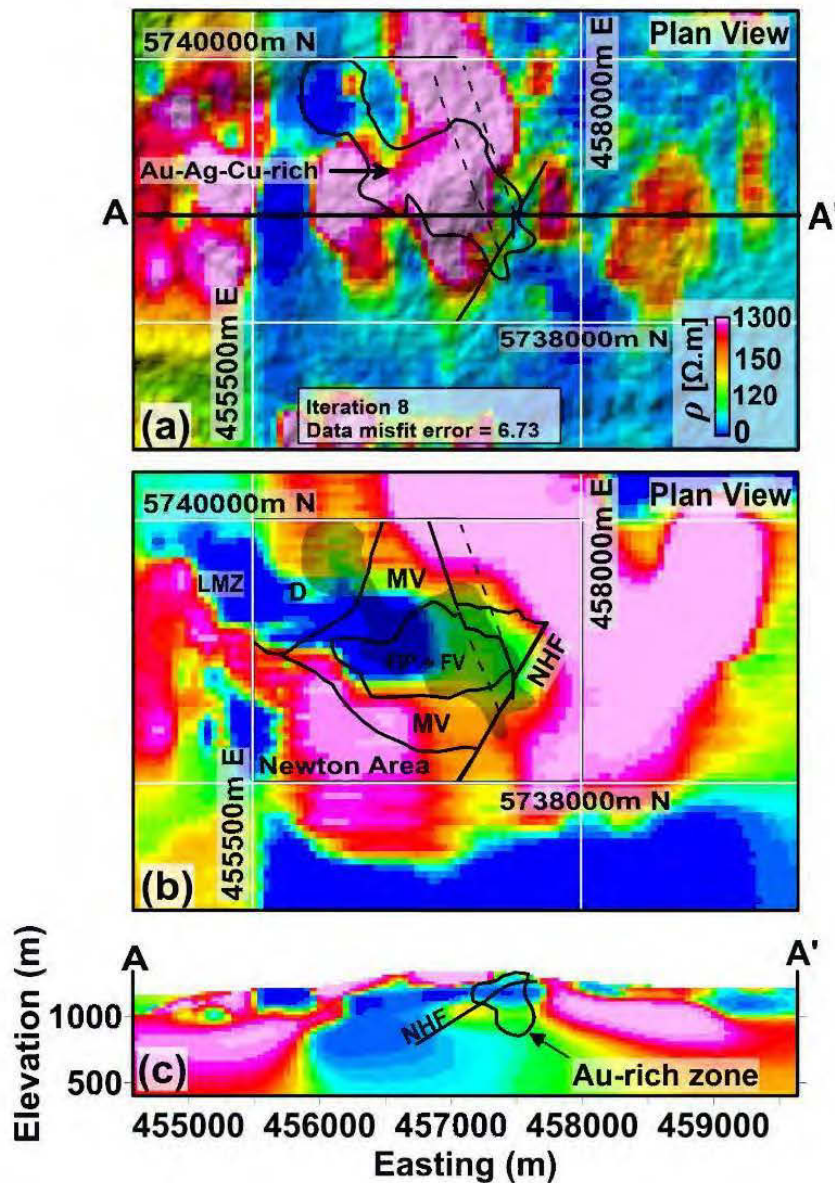


**Figure 3.11** Prospect scale inversion of IP-DC resistivity data over Newton area: (a) Plan view of the recovered resistivity model draped on a shaded relief topography model (Outline of Au-Ag-Cu mineralization is shown in the black contour). (b) Resistivity model sliced at elevation 1000 m (the bedrock geology is overlapped). (c) Resistivity model cross-cut on the profile AA' at 5738800m N (Outline of Au mineralization is shown in the black contour).



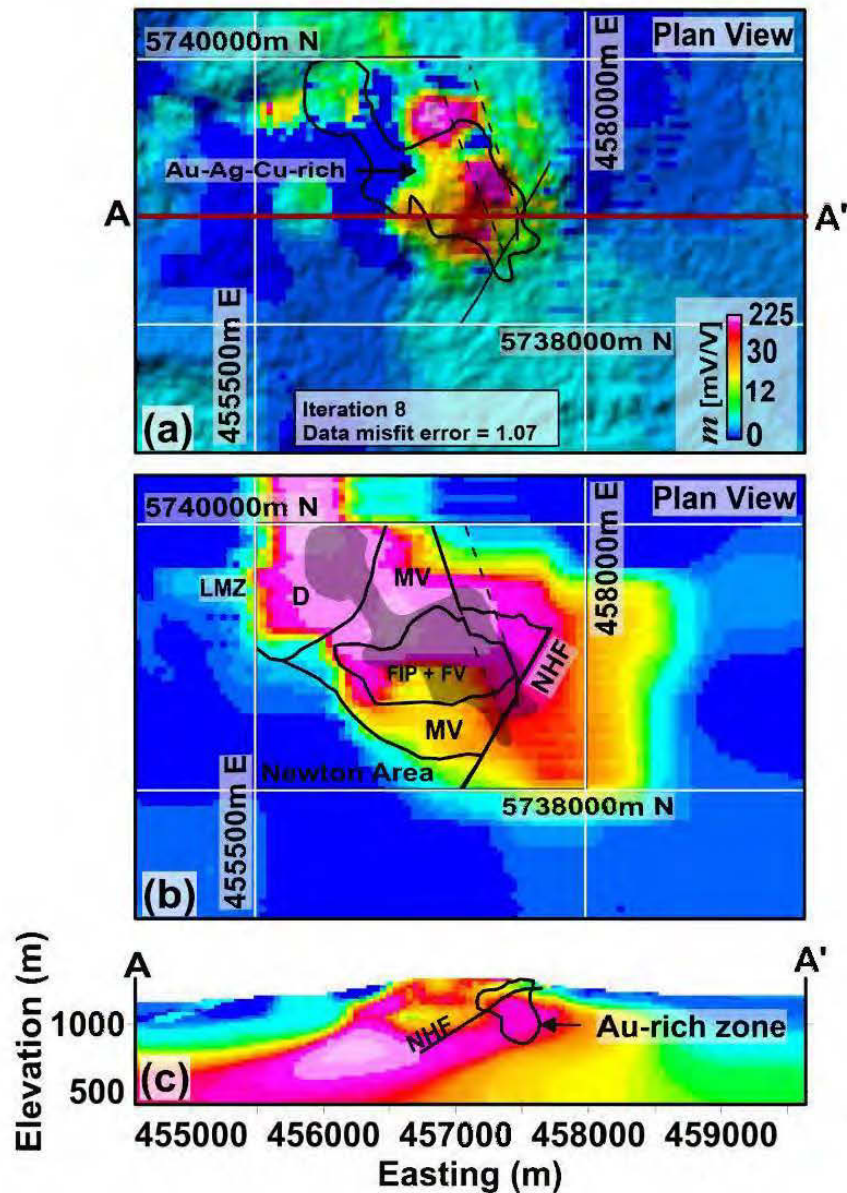


**Figure 3.12** Prospect scale inversion of IP-DC resistivity data over Newton area: (a) Plan view of the recovered chargeability model draped on a shaded relief topography model (Outline of Au-Ag-Cu mineralization is shown in the black contour). (b) Chargeability model sliced at elevation 1000 m (the bedrock geology is overlaid on the model). (c) Chargeability model cross-cut on the profile AA' at 5738800m N (Outline of Au mineralization is shown in the black contour).

IP-DC resistivity inversion is controlled by different  $k_1$  and  $k_2$  factors to see which output is more consistent with our prior knowledge of the region. Getting too close to the  $l^2$ -norm criteria (larger cut-off factors) increased the misfit error. Closer to  $l^1$ -norm (smaller cut-off factors) produced too sharp boundaries not consistent with magnetic inversion and prior geological information. The most consistent results obtained with  $k_1 = 0.05$  and  $k_2 = 0.01$ .

A significant low resistivity zone with an NW-SE trend is hidden under a large resistivity cap (Figure 3.11). The electrical resistivity image divided a very resistive mafic volcano-sedimentary mixture from a low-resistivity region related to a mix of porphyritic intrusions, felsic volcanic rocks, and the younger dioritic intrusion. Therefore, the host rock of Au mineralization (sericitic felsic volcanic rocks) in electrical resistivity images can be detected as a low-resistivity body, though in some places, other low-resistivity sources (within the dioritic and porphyritic intrusions) participate in the bulk resistivity-lows.

The chargeability of sulfide dissemination (Figure 3.12) is more than 50 mV/V, and is related to 2-7% disseminated sulfide mineralization, including pyrite, marcasite, sphalerite, chalcopyrite, and arsenopyrite. Minor chargeability contributors are probably clay contents and membrane polarizations in fracture zones and hydrothermal alterations.

### 3.6.3 Deposit scale constrained interpretation

At this scale (boreholes range), the cooperative magnetic-IP-DC resistivity inversion has focused more to the epithermal mineralization zone. The result of the cooperative magnetic- IP-DC resistivity inversion is also shown in Figure 3.13.

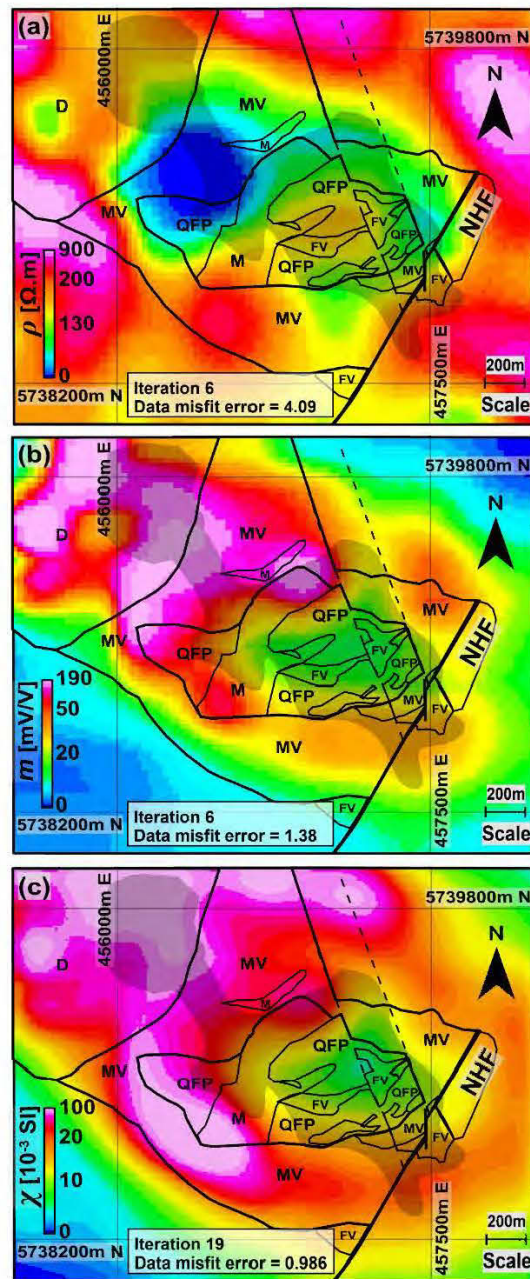


**Figure 3.13** Deposit scale cooperative magnetic-IP-DC resistivity inversions sliced at the elevation of 1000 m: (a) Electrical resistivity model. (b) IP chargeability model. (c) Magnetic susceptibility model. The bedrock geology is overlaid on all models. The gray shaded zone is the outline of Au-Ag-Cu mineralization.

No prior geological information has been used to constrain the inversion. Yet, the cooperative inversion results are reasonably matched with the known borehole geology. As can be seen, the porphyritic intrusions at the center of deposit show low amplitude susceptibilities that are surrounded by a ring of high magnetic mafic volcanic rocks. The diorite intrusion is also imaged as a large magnetic-high in the northwest. By comparing the Figure 3.13c and Figure 3.10b, it is evident that constraining the magnetic inversion with IP chargeability model has produced a more precise magnetic susceptibility image that is in good agreement with the prior geological information.

The cooperatively inverted physical properties are classified into several distinct petrophysical domains (Figure 3.14). Physical property cross plots for every two physical properties are divided into separate regions based on the lower (20<sup>th</sup>) and higher (80<sup>th</sup>) percentiles of the third physical property. Four distinct petrophysical domains (Table 3.1) are inferred from the integration of physical properties on the three physical properties' cross-plots.

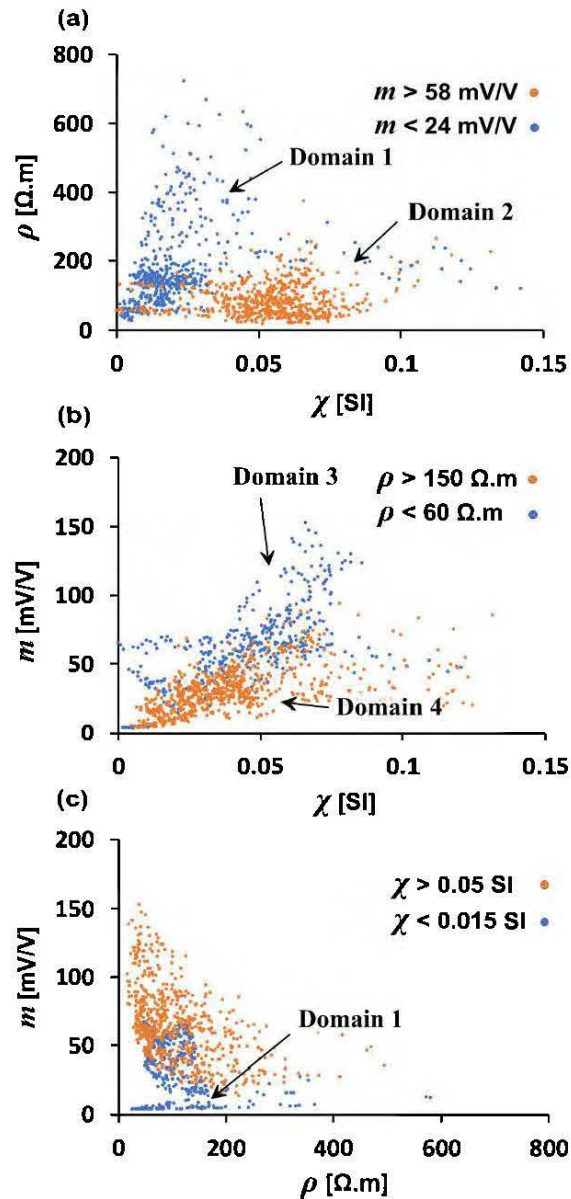


**Figure 3.14** Petrophysical domains inferred from the integration of cooperatively inverted physical properties on the three physical properties' cross-plots. (a) A susceptibility-resistivity cross-plot with two distinct domains related to the high and low chargeability values. (b) A susceptibility-chargeability cross-plot with two distinct domains related to the high and low resistivity values. (c) A resistivity-chargeability cross-plot with two distinct domains related to the high and low susceptibility values.



**Table 3.1** Classified petrophysical domains based on inverted physical properties and their integrated interpretation.

Domain	$\rho$ [ $\Omega$ .m]	$m$ [mV/V]	$\chi$ [ $10^{-3}$ SI]	Interpretation
1	No signature	Low	Low	Porphyritic intrusions
2	Low	High	No signature	Sulfide dissemination
3	Low	High	High	Cu-rich (north-west of the property)
4	High	Low	Low	Au-Ag-Cu-rich with silicifications

In Figure 3.15, the cooperative inversion results are compared with borehole information on cross sections (see profile AA' in Figures 3.3, 3.4 and 3.5). The results help to predict the continuation of the hidden features in deeper levels (Figure 3.15d). The high magnetic cap has been imaged thinner from the constrained inversion, and as can be seen in Figures 3.15c and 3.15d, is related to a mixture of the mafic volcanic rocks (MV) and the younger dioritic intrusions (D). Though, the LMZ was positioned deeper in earlier unconstrained modeling (Figures 3.9 and 3.10), the cooperative inversion has replaced it upward (about 500 m) and imaged it right under the high magnetic cap (magnetic susceptibilities  $> 0.04$  SI). Several flanks of this LMZ locally reduce the magnetic susceptibilities to 0.015 SI. This structure is probably a response of intermediate-to-felsic porphyritic intrusions (FIP) and interbeds of felsic volcanic rocks (FV) within the upper high magnetic cap (Domain 1). Note that the Domain 1 repeats on both cross-plots of Figures 14a and 14c.

The chemical alteration assemblages overprint all rocks in the Newton epithermal system and show specific physical property features. Pyrite is the dominant sulfide dissemination and is accompanied by high chargeabilities and low resistivities (Domain 2). The northwest part of the mineralization (within the gray shaded region in

Figures 3.13) is exclusively a Cu-rich zone with high susceptibilities, high chargeabilities and low resistivities due to the presence of more magnetite-bearing rocks and sulfides (Domain 3). The Quartz-Sericite assemblage is accompanied by Au-Ag-Cu mineralization on the hanging wall of NHF and appears as a silicified Au-Ag-Cu-rich zone with high resistivity and low chargeability/susceptibility (Domain 4).

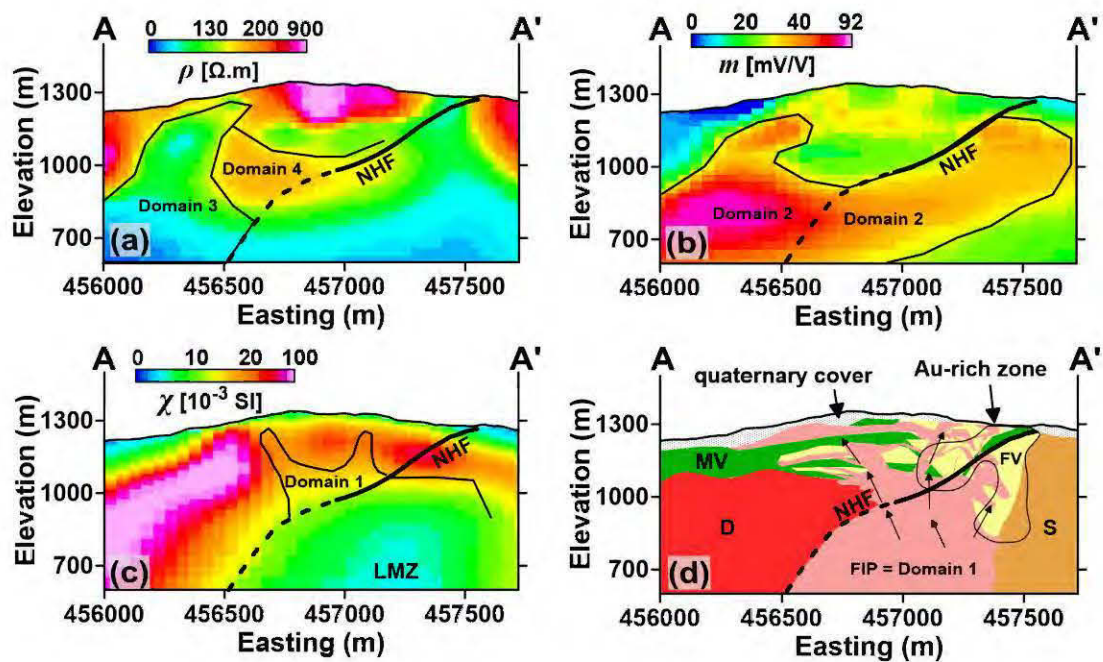


**Figure 3.15** Results of cooperative modeling compared with borehole information cross-cut on the profile AA' at 5738800m N in Figures 3.3: (a) Electrical resistivity model. (b) IP chargeability model. (c) Magnetic susceptibility model. (d) Integrated geological interpretation.

### 3.7 Conclusion

Geophysical images identify successfully several geological features in different scales. However, there are diverse sources of geophysical anomalies that collectively contribute to the observed geophysical signals in a mixed form. At the regional scale, MVI revealed a high susceptibility zone with a very deep root that contains a LMZ within itself. The concentric shape of this LMZ might imply a hydrothermal alteration pattern related to a deep underlying porphyry system. Several flanks of the LMZ reach to the surface and have structural links with the epithermal mineralization near a shallow post mineralization thrust fault.

IP-DC resistivity inversion uncovered a significant low resistivity zone under a large resistivity cap. The host rock of Au mineralization (quartz-sericitic felsic volcanic rocks) in electrical resistivity images can be detected as a low-resistivity body, though in some places, other low-resistivity sources (within the dioritic and porphyritic intrusions) participate in the bulk resistivity-lows. The chargeability of sulfide dissemination is related to the distribution of pyrite, marcasite, sphalerite, chalcopyrite, and arsenopyrite. Minor chargeability contributors are probably clay contents and membrane polarizations in fracture zones and clay alterations.

The cooperative magnetic-IP-DC resistivity inversion reduced the magnetic inversion uncertainty at deposit scale and provided an enhanced magnetic susceptibility image of the deposit. The constrained magnetic susceptibility model detects the high magnetic mafic volcanic rocks and diorites, as well as susceptibility-lows of the porphyritic intrusions and felsic volcanic rocks (host rock of Au). In some places, there is still ambiguity in the distinction between magnetic-highs of diorite and mafic volcanic rocks, as well as susceptibility-lows of felsic volcanic rocks (host rock of Au) and porphyritic intrusions.

Four petrophysical domains are inferred from cross-correlation of physical properties, including:

- Domain 1: A low chargeability and low susceptibility zone related to the porphyritic intrusions with variable resistivity values.
- Domain 2: A low resistivity and high chargeability zone with variable susceptibility values related to the sulfide dissemination.
- Domain 3: A Cu-rich zone with high susceptibilities and chargeabilities and low resistivities due to the presence of more magnetite-bearing rocks and sulfides.
- Domain 4: A Au-Ag-Cu-rich zone with low susceptibilities (epithermal demagnetization), low chargeabilities and high resistivities (silicifications).

Further studies in development include the application of multivariate feature extraction and machine learning to uncover the hidden patterns inside the multiple images semi-automatically.

### 3.8 Acknowledgments

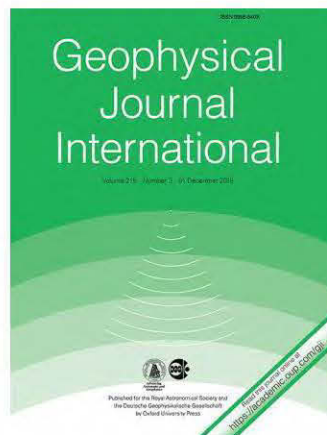
This work is funded by a Strategic Projects Grant from the Natural Sciences and Engineering Research Council of Canada with industry partners Amarc Resources Ltd., Geotech Ltd., Gerald G. Carlson, and John A. Chapman. Amarc Resources Ltd. is particularly thanked for providing access to drillcore and geophysical data; Geotech Ltd. is acknowledged for the collection of the aeromagnetic data as well as valuable discussions with us through the project. We also thank Walcott Geoscience for collecting IP-DC resistivity data and in-field assistance.

## CHAPTER IV

### FEATURES EXTRACTION FOR 3D INTERPRETATION OF MULTIPLE GEOPHYSICAL DATA THROUGH INDEPENDENT COMPONENT ANALYSIS

Bahman Abbassi and Li Zhen Cheng

This paper was submitted to Geophysical Journal International in May 2018



## Résumé

La présente étude vise à extraire des informations géologiques à partir de modèles de propriétés physiques inversées ciblant les gisements minéraux. Quelle que soit la précision des inversions de données géophysiques, chaque modèle de propriété physique inversée n'est sensible qu'à un nombre limité de caractéristiques géologiques. Par conséquent, différentes parties de la géologie du sous-sol peuvent être reconstruites à partir de divers modèles de propriétés physiques. La question clé est de savoir comment nous rassemblons ces caractéristiques cachées dans un espace de grande dimension pour reconstruire un modèle géologique pertinent. Une approche d'extraction de caractéristiques multivariées est simulée dans cette étude qui vise à séparer les caractéristiques géologiques superposées à l'intérieur de plusieurs images de propriétés physiques. Nous montrons que l'analyse de composants indépendants rapides (Fast-ACI) est une méthode robuste pour l'extraction de caractéristiques géologiques qui extrait les caractéristiques latentes par maximisation de la non-gaussianité. Nous montrons également que l'accentuation des images de propriétés physiques inversées a un effet important sur le processus d'extraction de caractéristiques et conduit à des reconstructions de modèles géologiques plus efficaces. La présente méthodologie est reproductible pour n'importe quel nombre de lithologies et de combinaisons de propriétés physiques et sépare les motifs géologiques de fond des surimpressions de l'altération chimique.

## Abstract

The present study aims to extract geological information from inverted physical property models, targeting mineral deposits. No matter how accurate the geophysical data inversions are, each inverted physical property model is only sensitive to a limited number of geological features. Therefore, different parts of the subsurface geology can be reconstructed from various physical property models. The key question is how we put together these hidden features inside a high-dimensional space to rebuild a relevant geological model. A multivariate feature extraction approach is simulated in this study that aims to separate the overlapped geologically features inside multiple physical property images. We show that the fast-independent component analysis (fast-ICA) is a robust method for the geological feature extraction that seeks to extract latent geological features through non-gaussianity maximization. We also show that the sharpening of the inverted physical property images has an important effect on the feature extraction process and leads to more efficient geological model reconstructions. The present methodology is reproducible for any number of lithologies and physical property combinations and separates the background geological patterns from overprints of chemical alteration.



#### 4.1 Introduction

Integrated 3D imaging methods provide a high potential for the detection and the characterization of mineral deposits (Dentith and Mudge, 2014; Lelièvre and Farquharson, 2016). Inferring geological information from multiple physical property models, without incorporating prior geological information considerably adds value to pre-drilling decision-making assessments. However, in most cases, additional chemical alteration heterogeneously overprints and eventually changes the bulk physical properties of rocks and imposes difficulties in identification of the latent geological features inside 3D physical property images.

The current numerical advances are focused mostly on the inversion methodologies to tackle the problem of non-uniqueness of the recovered physical properties through various methods like, borehole constrained inversion (Fullagar et al., 2000; Wisen and Christiansen, 2005; Lelièvre, 2009; Lelièvre et al., 2009), cooperative inversion (Lines et al., 1988; Paasche and Tronicke, 2007) and joint inversion methods (Haber and Oldenburg, 1997; Doetsch et al., 2010; Chen and Hoversten, 2012; Gallardo et al., 2012; Haber and Gazit, 2013). Though it is essential to recover reliably accurate 3D physical property models; a more meaningful but challenging question is how to unmix independent geological sources from physical property images.

We compare different unmixing schemes based on variance maximization, kurtosis maximization, and negentropy maximization principles. Variance maximization is the standard method of source separation that is used in the principal component analysis (PCA). However, the uncorrelatedness obtained by PCA is just a weaker form of independence (Hyvärinen and Oja, 1997; Honório et al., 2014). The kurtosis and negentropy maximization methods are widely used in ICA-based source separation algorithms. Unlike PCA, ICA goes beyond the Gaussian assumption and incorporates

higher order statistics to find a new set of latent variables that are maximally independent of each other (Hyvärinen and Oja, 1997; Hyvärinen and Oja; Hyvärinen et al., 2001).

ICA is an active and interdisciplinary research topic (Comon, 1994; Hyvärinen and Oja, 1997; Hyvärinen and Oja, 2000; Hyvärinen et al., 2001; Hyvärinen, 2013) with numerous applications in remote sensing (Bayliss et al., 1998; Amato et al., 2008; Barnie and Oppenheimer, 2015; Liu et al., 2015), medical imaging (Choudrey and Roberts, 2002; Beckmann and Smith, 2004; Griffanti et al., 2014), and image processing (Jenssen and Eltoft, 2003; Zou et al., 2006). In geophysical studies, the applications are mostly focused in the field of exploration seismology to handle the multidimensionality of seismic data and reducing unwanted seismic artifacts from raw data (Van der Baan, 2006), or extracting useful frequency features from processed seismic data (Honório. et al., 2014).

In this study, we propose a 3D implementation of independent component analysis (ICA) to extract hidden geological features from multiple physical property images. The ICA algorithm in this study transforms a set of physical property images into independent geological features. At first, we produce three physical property models, including magnetic susceptibility, electrical resistivity and induced polarization chargeability to form a petrophysical system, which bears specific underlying geological patterns. Then, three geophysical fields' responses are synthesized from previously modeled physical properties. The inversion of those synthetic data seeks to rebuild the three physical properties models, which are later used to recover the hidden geological features by different source separation methods. Finally, we show how negentropy maximization compared to variance, and kurtosis maximization successfully separates the alteration overprints from background geological features.

We also explore the effect of sharp and smooth inversions on the performance of the feature extraction process.

#### 4.2. Feature Extraction Methodology

The general assumption in all geophysical methods is that the observed geophysical fields are due to the subsurface physical property sources, which are linked to several latent geological features. Geophysical inversion methods partially solve this problem through transforming measured signals to 3D physical property models. However, separation of overlapped (mixed) geological features from multiple physical property images is also crucial in the identification of mineral exploration targets with complex hydrothermal alteration patterns overprinted on the host geology.

In this study, we simulated the physical properties in the form of the combination of latent geological features. A linear mixing model is used to create physical property images ( $P_j$ ) from latent geological features ( $L_i$ ) with an additional non-gaussian geological noise ( $P_{Noise}$ ):

$$P_j = \sum \alpha_{ij} L_i + P_{Noise} \quad (IV.1)$$

Where  $i = 1, 2, \dots, n$  denotes the number of the latent geological features and  $j = 1, 2, \dots, m$  indicates the number of physical properties. The  $\alpha_{ij}$  are the mixing weights.

The problem is to find a separation matrix ( $w_{ij}$ ) that tends to unmix the physical properties ( $P_j$ ) to recover the source geological features ( $L_i$ ):

$$L_i = \sum w_{ij} P_j \quad (IV.2)$$

The Equation IV.2 is the general formulation of a feature extraction process that tends to eliminate or at least reduce the effect of geological feature-overlaps on the physical property images.

Obtaining a relevant separation matrix ( $w_{ij}$ ) is possible through making few assumptions about statistical measures. One important statistical measure is correlation. It is very common that two geophysical properties imaged by two different methods being correlated. For example, if the magnetic susceptibility and the electrical resistivity of a rock show a linear relationship, both physical properties reflect a common source, and consequently, we can transfer the bivariate data (susceptibility vs. resistivity) to a univariate form (principal component) without losing any valuable information. This transformation is called dimensionality reduction that is the basis of PCA algorithms (Hyvärinen and Oja, 2000; Trauth, 2015). PCA produces images that are linearly uncorrelated, and this approach is usually called whitening because this is the property of the white noise. PCA algorithms utilize maximization of second-order statistical measure (variance) for image separation. However, when there is a nonlinear form of correlation (dependency) between images, PCA will not work, and one needs to find another way to unmix interdependent images (Hyvärinen, 2002; Trauth, 2015).

On the other hand, ICA separates mixed images into nonlinearly uncorrelated images through maximization of non-gaussianity. The one-dimensional ICA analogy is well-known as a classical cocktail party problem (Cherry 1953), where crowds of people are talking independently together. Human auditory system, for example, with two receivers, hear a mixture of signals in a cocktail party and can differentiate the latent sources to a certain degree. However, by installing several microphones and maximizing the non-gaussianity of received signals, we will be able to separate more voices. The same analogy is applied to neuroscience where the spatiotemporal ICA problem in medical imaging is compared to a neurological cocktail party problem by

Von der Malsburg and Schneider (1986) and Brown (2001). The feature extraction procedure in this study also can be seen as a form of 3D geophysical cocktail party problem, where one tries to extract latent geological features inside multiple physical property images.

Two characteristics of the mixing process enable us to separate geological features in two different ways:

1. The mixing process increases the normality of the images, i.e., the distributions of physical property images are more Gaussian than the distributions of latent geological features. This is a result of the central limit theorem in probability theory which states that the distribution of a sum of independent random variables tends toward a Gaussian (normal) distribution (Hyvärinen and Oja, 2000). We use this principle to maximize the non-gaussianity of physical properties through kurtosis maximization.
2. The spatial complexities of the physical property images are equal to or greater than that of the least complex geological features (Hyvärinen and Oja, 2000). This general principle enables us to maximize the non-gaussianity of physical properties through negentropy maximization.

Fast-ICA algorithm starts with two preprocessing steps. First, removing the mean of input physical properties ( $P$ ), and then whitening by PCA giving their variance unit value. PCA looks for a weight matrix  $D$  so that a maximal variance of the principal components of the centered physical properties ( $Y_{PC}$ ) are confirmed:

$$Y_{PC} = D^T P \quad (\text{IV.3})$$

Optimization of the PCA criterion is possible by eigenvalue decomposition (Hyvärinen and Oja, 2000). The next step in the Fast-ICA is increasing the non-gaussianity of the

principal components. It aims to find a rotation matrix  $R$  that during the multiplication with principal components produces the least Gaussian outputs ( $L^*$ ) that are approximations of the latent geological features:

$$L^* = R^T Y_{PC} \quad (\text{IV.4})$$

One way to calculate the rotation matrix  $R$  is to use kurtosis as a measure of non-Gaussianity:

$$\text{kurt}(L^*) = E\left((R^T Y_{PC})^4\right) - 3\left\{E\left((R^T Y_{PC})^2\right)\right\}^2 \quad (\text{IV.5})$$

Where  $E(\cdot)$  denotes the expected value.

Kurtosis provides a measure of how Gaussian ( $\text{kurt} = 0$ ), super-gaussian ( $\text{kurt} > 0$ ) or sub-gaussian ( $\text{kurt} < 0$ ) the probability density functions of the physical properties are. Therefore, the highest non-Gaussianity of  $L^*$  is equivalent to the maximum or minimum excess kurtosis of its distribution. In this study, we use the fixed-point iteration scheme of Hyvärinen and Oja (1997), for finding the local extrema of the kurtosis. Fast-ICA has a fast quadratic or cubic convergence and requires slight memory space (Hyvärinen, 2002). However, kurtosis is not a robust measure of non-gaussianity in the presence of noises. Kurtosis is an approximated measure of the fourth central moment of the probability density function of data, and to calculate it accurately we need to have an infinite number of physical property values. This makes kurtosis very sensitive to outliers, i.e., a single erroneous outlier value in the tails of the distribution makes kurtosis extremely large. Therefore, using kurtosis is well justified only if the independent components (geological features) are sub-gaussian and there are no outliers (unknown geological noises or other artifacts on inverted physical property images).

Therefore, we need to assess non-gaussianity in a different way that can handle the fluctuations of outliers. Alternatively, maximization of negentropy is a robust technique to obtain the rotation matrix  $R$  during the Fast-ICA procedure.

Negentropy is based on the information-theoretic quantity of entropy. The entropy ( $H$ ) of a signal ( $P$ ) with probability density of  $p(P)$  is defined as (Hyvärinen, 2000):

$$H(P) = -\int p(P) \log p(P) dP \quad (\text{IV.6})$$

The more random (unpredictable and unstructured) the variable is, the larger its entropy. Among all random variables, the Gaussian variable has the largest entropy.

By definition, negentropy (normalized differential entropy) of a signal is the difference between the entropy  $H(P)$  of that signal and the entropy  $H(P_{gauss})$  of a Gaussian random vector of the same covariance matrix as  $P$ . Negentropy of the  $P$ , therefore is:

$$neg(P) = H(P_{gauss}) - H(P) \quad (\text{IV.7})$$

Negentropy is always non-negative and is zero when the signal has a Gaussian distribution. In other word, the more random (unpredictable and unstructured) the variable is, the larger its entropy. We approximate the negentropy through a nonpolynomial method (Hyvärinen, 2000):

$$neg(P) \approx c \left[ E\{G(P)\} - E\{G(P_{std})\} \right]^2 \quad (\text{IV.8})$$

Where  $c$  is an irrelevant constant, and  $P_{std}$  is a standardized gaussian variable ( $P_{gauss}$  of zero mean and unit variance).  $G$  is a non-quadratic exponential function that can handle the outliers efficiently (Hyvärinen, 2000):

$$G(P) = -e^{\left(\frac{P^2}{2}\right)} \quad (\text{IV.9})$$

To find the rotation matrix  $R$ , we maximize the objective negentropy by the fixed-point algorithm of Hyvärinen et al. (2000).

#### 4.3 Petrophysical Model: A Mixing System

The purpose of this study is to show numerically how the overlapped geological features could be seen in the form of physical properties and eventually appear as geophysical signals on the Earth surface. We also show how geological noise and inversion artifacts influence the process of feature extraction. We are not concerned about reconstructing any existing geological model, but we use a range of physical property values based on typical values of physical properties (Dentith and Mudge, 2014) attributed to disseminated sulfide deposits.

The underlying geological model is constructed from an original layered earth model that has passed through several faulting, folding, dyke intrusion, shear deformation and alteration overprints (Figure 4.1). The final 3D lithology model includes a set of background rock units ( $L_{1a}$ ,  $L_{1b}$ ,  $L_{1c}$ ,  $L_{1d}$ ) and two stages of hydrothermal alteration in the form of plug-shaped alteration overprints ( $L_2$  and  $L_3$ ).



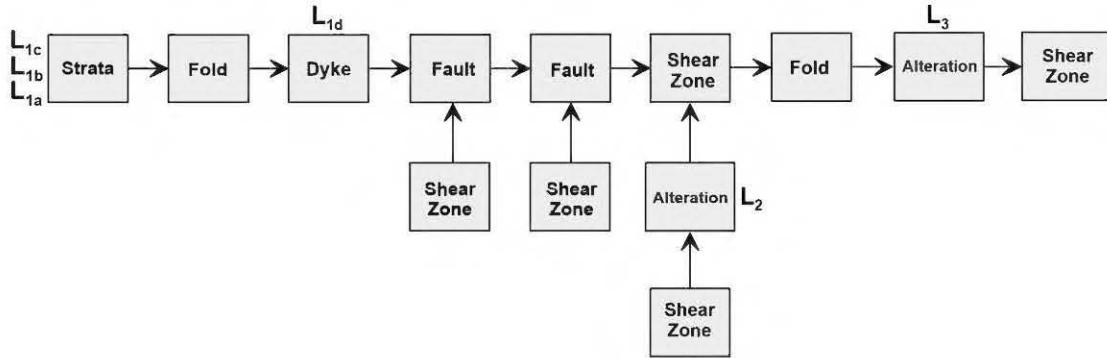


**Figure 4.1** Workflow of geological model construction. The background geology consists of a three-layer stratum ( $L_{1a}$ ,  $L_{1b}$ ,  $L_{1c}$ ) intruded by a dyke ( $L_{1d}$ ). After several faulting and shear deformation, two alteration events ( $L_2$  and  $L_3$ ) along with further deformations overprint the host geology. Noddy 3D geological and geophysical modeling package is used to build the geological model (Encom Technology Pty Ltd, 2009).

Figure 4.2, represents the final independent lithotypes that are used in this study. The mixture of the four background rock units ( $L_1$ ) and the two alteration events ( $L_2$  and  $L_3$ ) correspond to three main physical property distributions, including electrical resistivity ( $\rho$ ), IP chargeability ( $m$ ) and magnetic susceptibility ( $\chi$ ). A linear mixing matrix based on the matrix  $A$  in Equation IV.1 is built to produce the physical properties of the deposit. The mixing weights ( $A$ ) are selected in a way that they produce a petrophysical model of a disseminated sulfide deposit with three major petrophysical properties:

- Resistivity highs and lows related to background geology.
- High chargeabilities related to the alteration halos with high concentrations of disseminated sulfides.
- Magnetic highs and lows related to both background geology and alteration halos.

$$\begin{array}{ccc}
 L_1 & L_2 & L_3 \\
 \downarrow & \downarrow & \downarrow \\
 A = [a_{ij}] = \begin{bmatrix} 0.90 & 0.05 & 0.05 \\ 0.05 & 0.20 & 0.75 \\ 0.45 & 0.25 & 0.30 \end{bmatrix} & \rightarrow & \begin{array}{l} \rho = 0.90L_1 + 0.05L_2 + 0.05L_3 \\ m = 0.05L_1 + 0.20L_2 + 0.75L_3 \\ \chi = 0.45L_1 + 0.25L_2 + 0.30L_3 \end{array}
 \end{array} \quad (\text{IV.10})$$

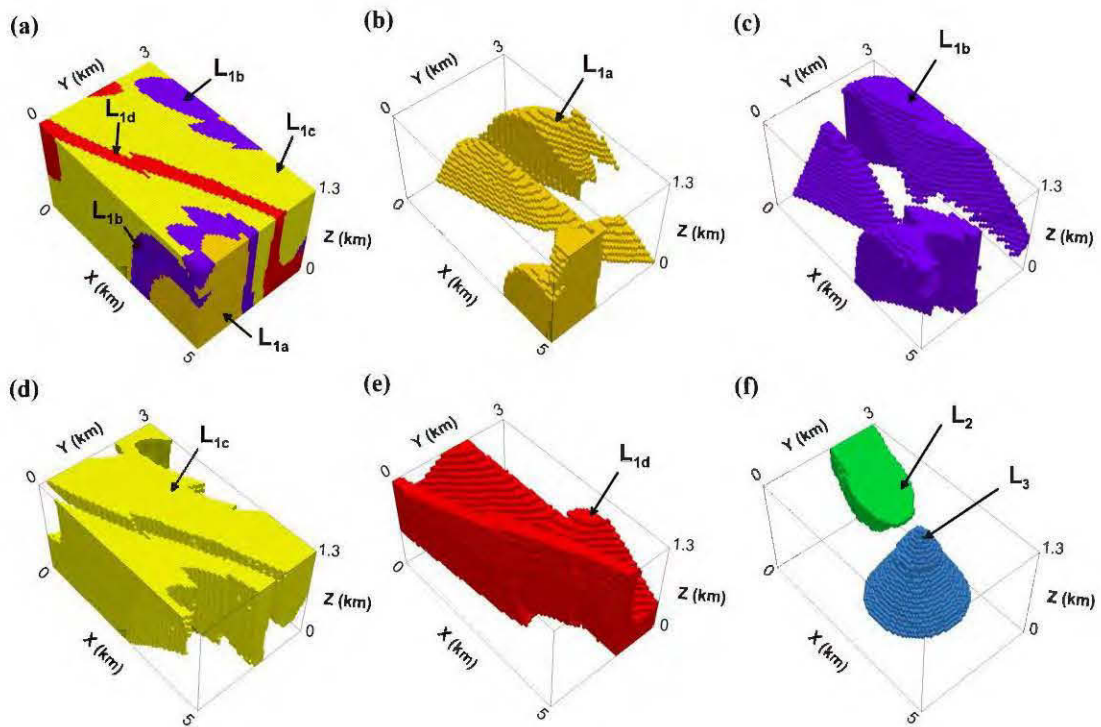
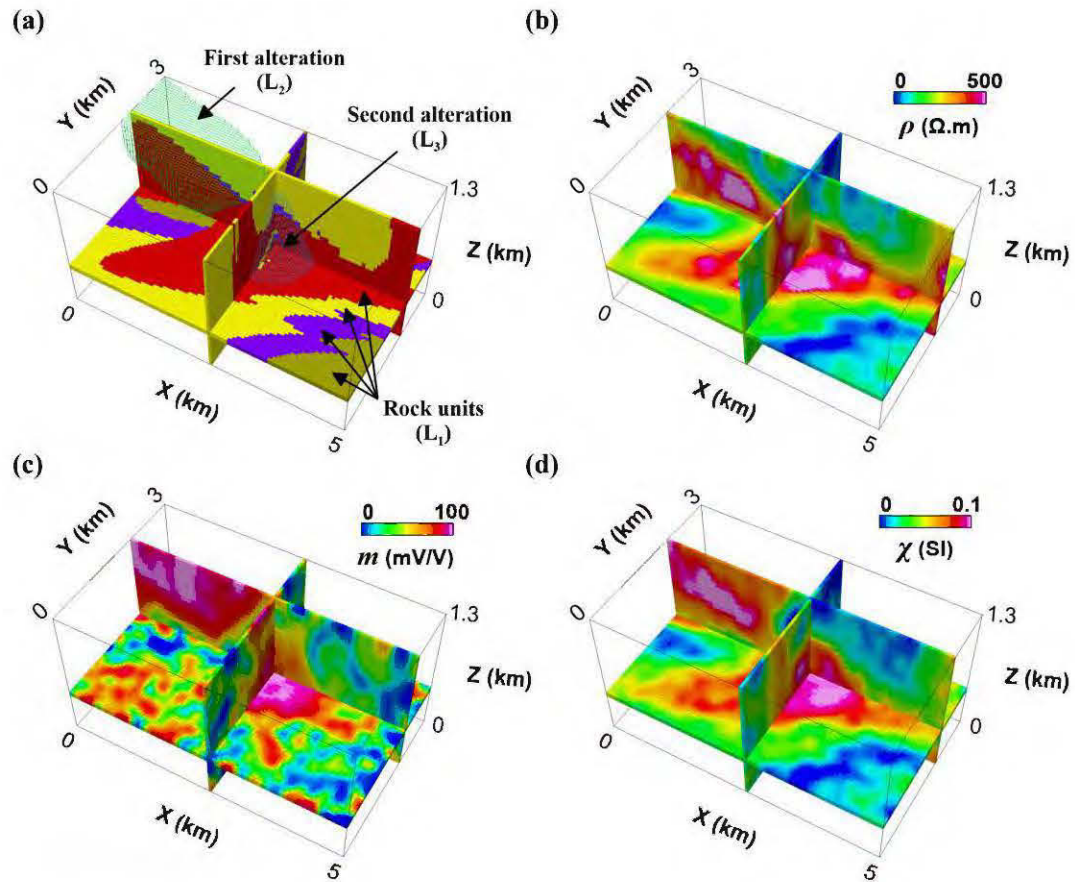


**Figure 4.2** 3D geological model: (a) 3D block view of all the background geological features. (b, c, d, and e) Background geological features ( $L_{1a}$ ,  $L_{1b}$ ,  $L_{1c}$ ). (f) Two successive alteration events overlapped on the background geology ( $L_2$  and  $L_3$ ).

Which means, the background geology ( $L_{1a}$ ,  $L_{1b}$ ,  $L_{1c}$ ,  $L_{1d}$ ) comprises 90 percent of the electrical resistivities, and the rest of the resistivities come from the two alterations (each 5 percent). The IP chargeabilities are least sensitive to the background geology (5 percent) and, 20 percent and 75 percent of them are related to the disseminated sulfidation associated with two alteration events ( $L_2$  and  $L_3$ ). Note that the 75 of

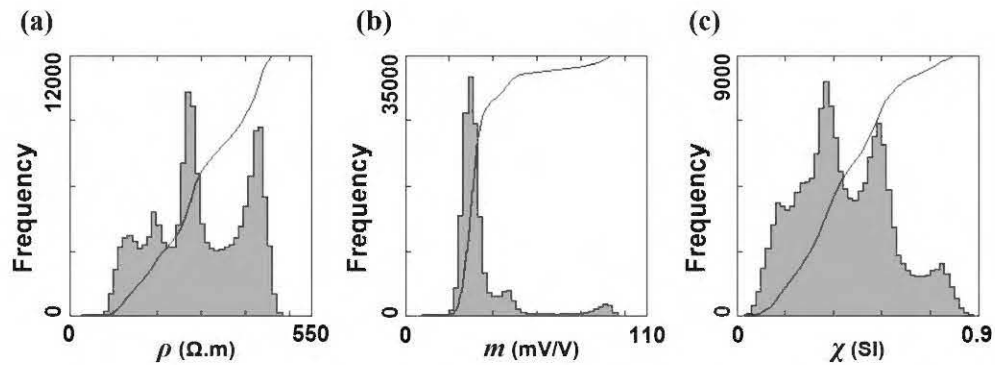
chargeability belongs to the second alteration, which means  $L_3$  bears largest amount of disseminated sulfide, but in deeper levels. The magnetic susceptibility is representative of 45 percent of the background geology, and the rest of the resistivities come from the two alterations (25 percent from  $L_2$  and 30 percent from  $L_3$ ). The resulting mixtures are then scaled from zero to a reasonable maximum, which is set to 500 Ohm-m, 100 mV/V and 0.1 SI for resistivities, chargeabilities, and susceptibilities, respectively.

Figure 4.3 shows the calculated physical property models. An additional non-gaussian noise is also added to the model. We used a Pearson random system in the form of a 3D matrix with unit standard deviation and skewness equal to 1 for resistivity and chargeability models and skewness equal to -1 for susceptibility model. The kurtosis of the geological noise is set to 5 for the resistivity model, 4 for the chargeability and susceptibility model.



**Figure 4.3** Latent geological features (a) compared to physical properties produced in the petrophysical mixing system ( $\rho$ ,  $m$ , and  $\chi$  in b, c, and d). Each physical property model provides partial information about the latent geological features.

The histograms of physical properties (Figures 4.4a, 4.4b, and 4.4c) show the multimodal nature of the physical properties due to the mixing process. However, the added non-gaussian geological noise has weakened some smaller patterns related to the overlaps of the background geological features with two alteration events. We expect that the transformation of geological information to geophysical signals and then reconstruction of physical properties through inverse modeling will significantly reduce this multimodality to bimodality or even unimodality. This information loss is one of the major limitations of 3D geophysical imaging.



**Figure 4.4** Histograms of simulated physical properties with added non-gaussian geological noise: (a) Electrical Resistivity distribution. (b) IP chargeability distribution. (c) Magnetic susceptibility distribution. The solid curve indicates the cumulative distribution function.

#### 4.4 Petrophysical Feature Extraction

We evaluate PCA and two ICA algorithms in Matlab environment to see which method is more stable in the extraction of geological features from physical properties. Based on the above mixed petrophysical model, we test our algorithms to separate sources without having any concern about how 3D inversion artifacts could influence our feature extraction procedure. Then, we introduce a more realistic scenario where input physical properties are obtained from the 3D inversion of geophysical data and compare the results to see how inverse modeling could change the efficiency of the feature extraction process.

Running PCA to separate petrophysical images did not yield efficient separation of geological features (Figure 4.5a, 4.5b, and 4.5c). The first and third principal components ( $PC_1$  and  $PC_3$  in Figures 4.5a and 4.5c) successfully represent the background geology ( $L_1$ ) and the first alteration event ( $L_2$ ), but in the second principal component ( $PC_2$  in Figure 4.5b) the two alteration events are still mixed. In other word,

PCA recreates another set of overlapped images on PC2 and is obviously not useful in source separation.

Fast-ICA by kurtosis maximization (kICA) separates sources to some extent, but, some of the features remain mixed in the first and second independent components in the form of outliers (Figures 4.5d and 4.5e ), and the background geology is still mixed with the second alteration event (Figure 4.5f). However, Fast-ICA by negentropy maximization (nICA) has recovered the underlying geological features almost perfectly (Figure 4.5g, 4.5h, and 4.5i). As can be seen, nICA efficiently handles the added non-gaussian geological noise while separating the main geological features.



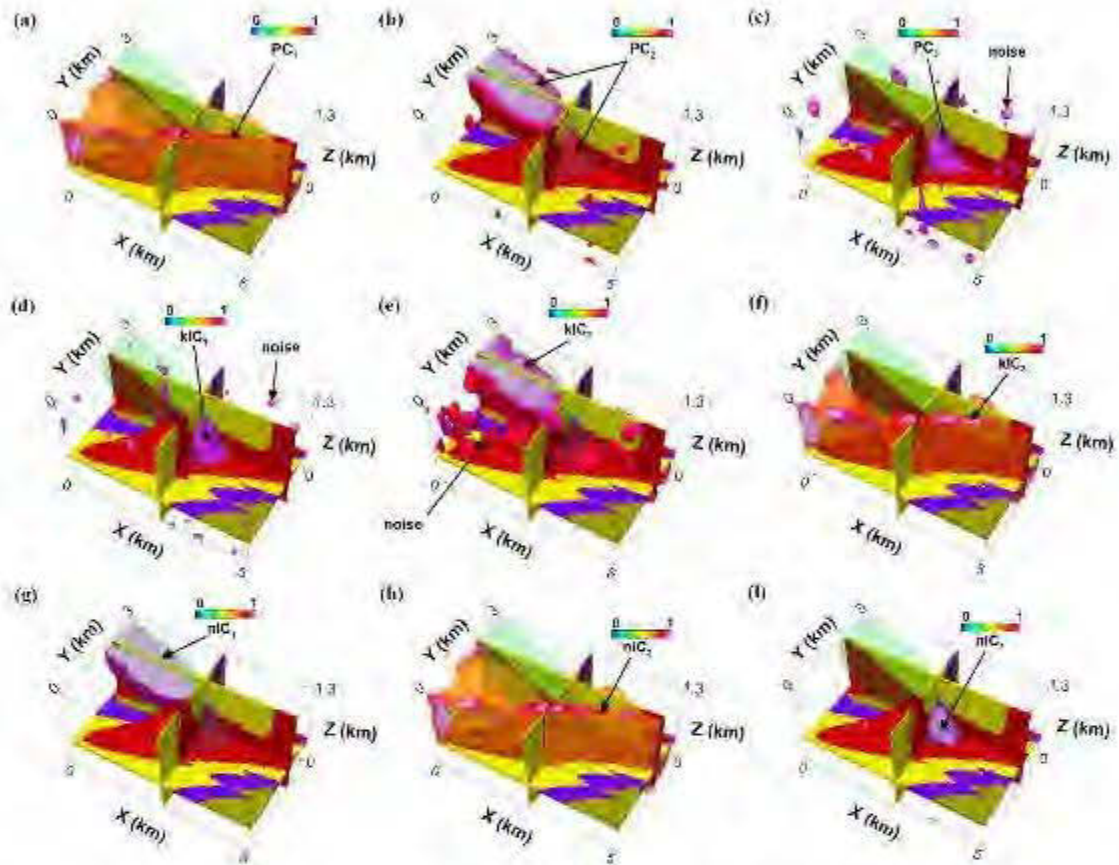


**Figure 4.5** Assessment of different source separation methods. (a, b and c) Principal component analysis. (d, e, f) Fast independent components by kurtosis maximization. (g, h, i) Fast independent components by negentropy maximization. All principal components (PCs) and independent components (kICs and nICs) are normalized from zero to one for consistency of visualization.

## 4.5 Simulation of Geophysical System

One of the objectives of this study is a post-inversion evaluation of geological feature extraction through adjustment of different inversion parameters. To illustrate the method, we generate synthetic data from the petrophysical model, then perform an inversion of those data, and finally extract geological features from the inversion results.

### 4.5.1 3D Forward Modeling

The simulation of the geophysical system consists of a well-posed set of equations that calculates the geophysical responses on the Earth surface of 3D physical property distributions. For the three physical property models, we used a finite element method to calculate their apparent resistivity, chargeability and total magnetic field responses (Li and Oldenburg, 1997; Li and Oldenburg, 2000; Loke et al., 2003; Loke, 2015).

In the case of DC/IP forward problem, the IP chargeability model is considered as a small perturbation of the reference electrical conductivity model (Li and Oldenburg, 2000). Normalized chargeability ( $0 \leq m \leq 1$ ) tends to decrease the reference conductivity ( $\sigma_{DC}$ ) in the modeled IP phenomenon and produces a perturbed subsurface conductivity ( $\sigma_{IP}$ ) as is presented below (Li and Oldenburg, 2000):

$$\sigma_{IP} = (1 - m)\sigma_{DC} \quad (\text{IV.11})$$

The Res3DMode program used in this study (Loke, 2015) calculates the forward potential responses of two conductivity models ( $\sigma_{DC}$  &  $\sigma_{IP}$ ) separately. The  $\sigma_{DC}$  model gives the apparent conductivity values ( $\sigma_a$ ), and apparent chargeabilities are calculated as bellow (Li and Oldenburg, 2000):



$$m_a = [\phi(\sigma_{IP}) - \phi(\sigma_{DC})] / \phi(\sigma_{DC}) \quad (\text{IV.12})$$

DC/IP forward calculation is performed with pole-dipole electrode configurations, the dipolar spacing of 100 m and dipolar separations up to 12 times in X and Y directions. The model mesh consists of 151 cells in the X direction, 111 cells in the Y direction and 38 cells in the Z direction, which has total 636918 rectangular cells. The electrical potentials calculated are 51 electrodes locations in the X direction and 31 electrodes locations in the Y direction.

Geosoft VOXI Earth Modeling package (Geosoft Inc., 2018) is used for the magnetic forward modeling. The magnetic spacing is 100m between observation points in both X and Y directions. The magnetic field over the 3D volume is set to 53913 nT with inclination and declination of 70 and -16 degrees, respectively. We assume that there is no remanent magnetization contributing to the surface observations and that demagnetization of rocks is negligible.

Figure 4.6 shows the forward responses of the magnetic and DC/IP models in the form of total magnetic field intensities (after reduction to the magnetic pole, Figure 4.6a), apparent resistivities (Figure 4.6b) and apparent chargeabilities (Figure 4.6c).

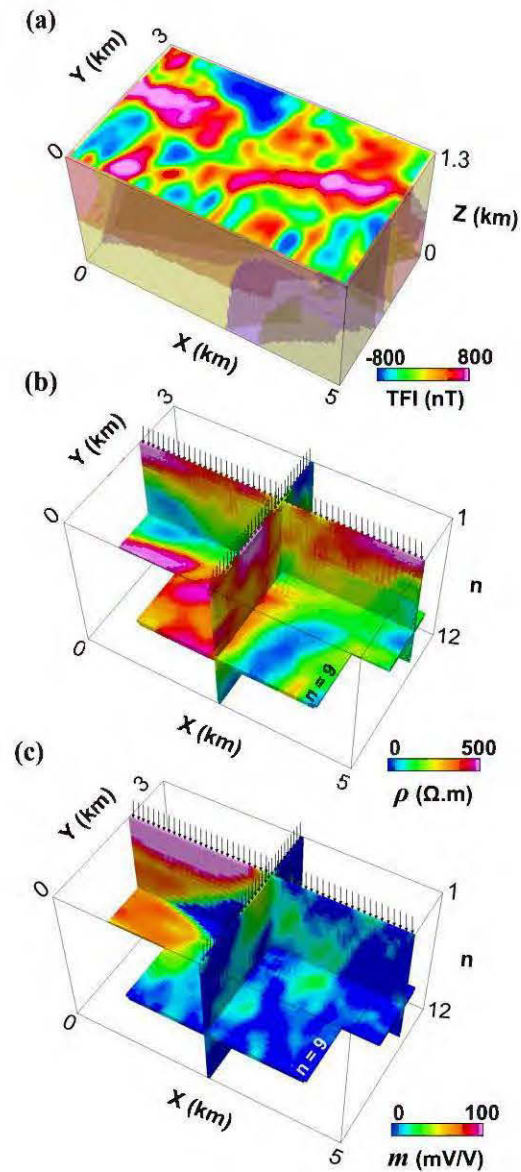


**Figure 4.6** The geophysical responses of the mixed physical properties. (a) Total magnetic field intensities after reduction to the magnetic pole. (b) Apparent resistivities. (c) Apparent chargeabilities. DC/IP responses are presented on two NS and EW pseudo-sections as well as a horizontal slice corresponding to the dipolar separation of  $n = 4$ . The arrows (black) indicate the location of simulated DC/IP electrodes.

#### 4.5.2 3D Inversion

Through the inversion process (imaging), we explore the effect of the smoothness and sharpness of the imaging system on the output of the feature extraction system. Two imaging scenarios - sharp versus smooth are considered in DC/IP inversion as well as magnetic inversion. We used Res3DInv program (Loke, 2015) for blocky inversion of electrical resistivity and chargeability data (Claerbout, 1973; Loke et al., 2003), and Geosoft VOXI Earth Modeling package (Geosoft Inc., 2012) for iterative reweighting inversion of magnetic data (Portniaguine and Zhdanov, 2002).

In each iteration of DC/IP inversion, a least-squares optimization reduces the gap between measured and calculated apparent properties ( $\sigma_a$  and  $m_a$ ) by modifying the  $\sigma_{DC}$  and  $\sigma_{IP}$  values. When the calculation reaches its threshold, the modeled resistivities and chargeabilities are determined by  $\rho = 1/\sigma_{DC}$  and  $m = 1 - (\sigma_{IP}/\sigma_{DC})$ , respectively. The blocky inversion algorithm (Loke et al., 2003), which uses an extension of  $l^2$ -norm and  $l^1$ -norm inversions, incorporates two cut-off factors in the DC/IP inversion: A data constraint cut-off factor ( $0 < k_1 < 1$ ), and a model constraint cut-off factor ( $0 < k_2 < 1$ ). Larger cut-off factors result in smoother physical property models closer to  $l^2$ -norm results. We used three different cut off factors: (1) The first DC/IP inversion with  $k_1 = 1$  and  $k_2 = 1$ , which results in smoothest physical properties. (2) The second DC/IP inversion with  $k_1 = 0.1$  and  $k_2 = 0.05$ , which results in sharper physical properties. (3) The third DC/IP inversion with  $k_1 = 0.01$  and  $k_2 = 0.005$ , which results in sharpest physical properties.

The iterative reweighting magnetic inversion uses a different approach to recover sharp susceptibilities: It uses the first iteration susceptibility inversion result as a constraint for subsequent inversions. This process is iterated until a satisfactory model is achieved (Portniaguine and Zhdanov, 2002; Geosoft Inc., 2012). The first three successive

iterations of the iterative reweighing magnetic inversion are also used to produce three smooth to sharp susceptibility models.

Figure 4.7 illustrates the recovered physical properties from above inversions. Figures 4.7a, 4.7b, 4.7c show physical property distributions ( $\rho$ ,  $m$ , and  $\chi$ ) from smooth inversion. Figures 4.7d, 4.7e, 4.7f show results of the sharper inversion. The sharpest inversion results are presented in figures 4.7g, 4.7h, 4.7i.

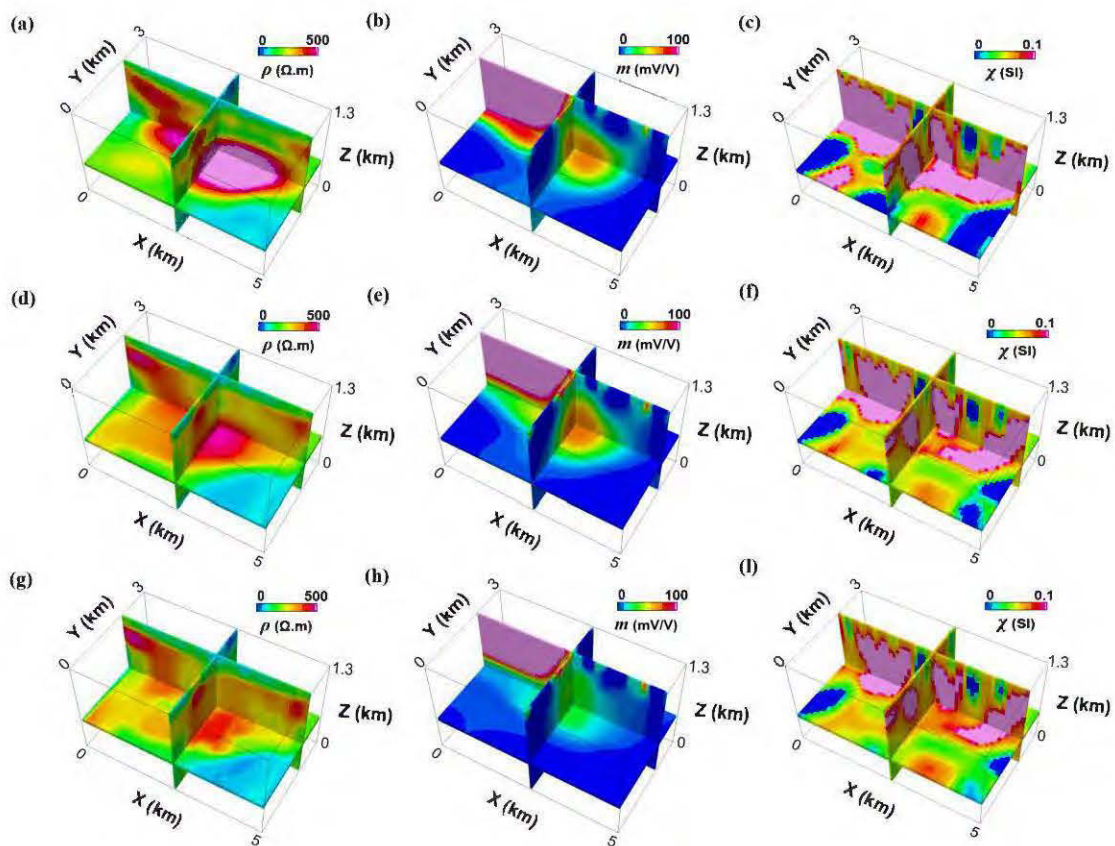


**Figure 4.7** Geophysical inversion results. (a), (b) and (c) are smooth inversion results. (d), (e) and (f) are sharper inversion results. (g), (h), (i) represent sharpest inversion results.

#### 4.6 Post-Inversion Feature Extraction

The negentropy maximization ICA method is used for geological features extraction from inversion results (Figure 4.8). The nICA of the smoothest physical properties (Figures 4.8a, 4.8b, and 4.8c) bear some mixed features inside the outputs of the independent components, which is understandable due to the effect of smoothness that make the edges of the geological features blurred. The first alteration event ( $L_2$ ) is clearly extracted in the second independent component ( $nIC_2$ ), but the background geology ( $L_1$ ) and the second alteration event ( $L_3$ ) are still mixed in the other independent components ( $nIC_1$  and  $nIC_3$ ).

The sharper inversion procedure increased the contrasts of the physical property images; however, a certain amount of information is always lost during the imaging process. The first alteration event ( $L_2$ ) is clearly extracted in the third independent component ( $nIC_3$  in Figure 4.8f), and the background geology ( $L_1$ ) is extracted in the second independent component ( $nIC_2$  in Figure 4.8e). However, the first independent component ( $nIC_1$  in Figure 4.8d) was not able to separate the first alteration event from the background geology.

The sharpest physical property images outline most of the latent geological features (Figure 4.8g, 4.8h, and 4.8i). Both alteration events are successfully extracted as distinct independent components ( $nIC_1$  and  $nIC_2$  in Figures 4.8g and 4.8h). The third independent component also represents a more accurate image of the latent background geology ( $nIC_3$  in Figures 4.8i).

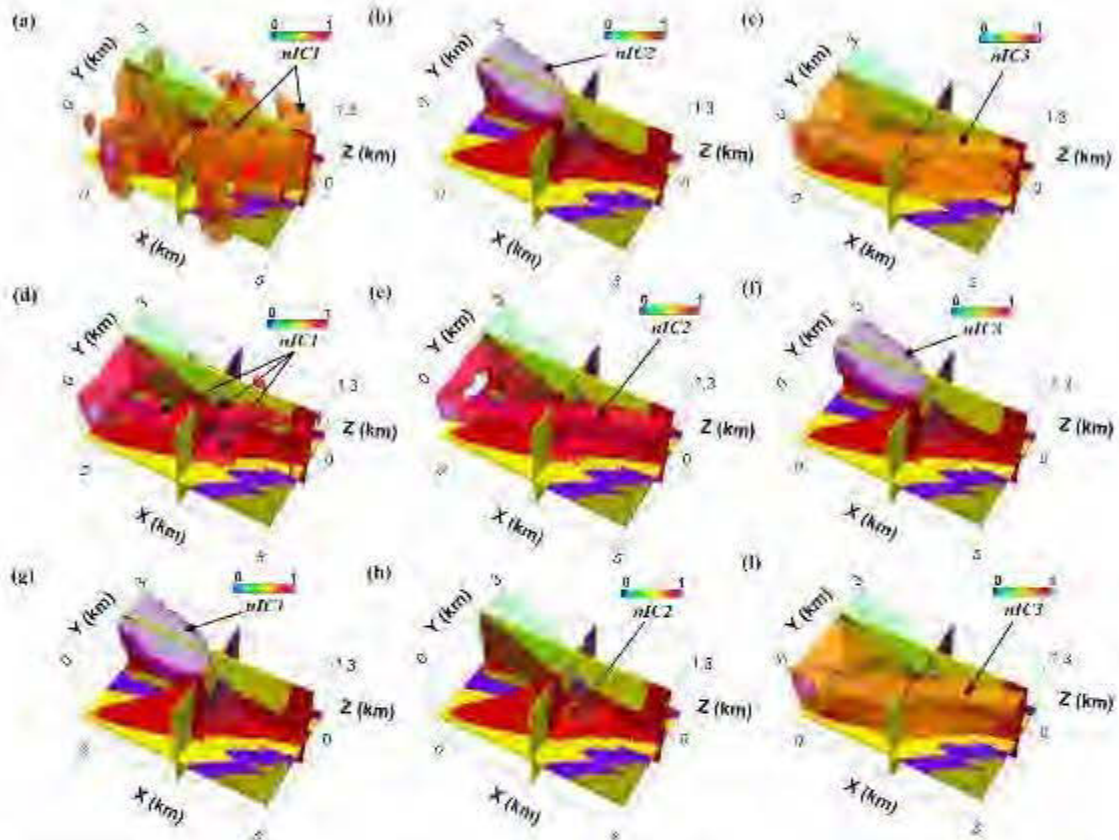


**Figure 4.8** Post-inversion feature extraction through negentropy maximization (nICA) on different inversion scenarios. (a), (b) and (c) are independent components of smoothest physical properties. (d), (e) and (f) are independent components of sharper physical properties. (g), (h), and (i) are independent components of sharpest physical properties.

Reducing the effect of the inversion artifacts, specifically in the magnetic inversion, demands to provide deep information about physical properties. Incorporating other techniques such as seismic and electromagnetic imaging can help to capture more geological features from modeled physical properties. If there is any coupling between physical property distributions, it is possible to run a cooperative inversion between multiple geophysical data, which allow inversions converge into more satisfactory results.



#### 4.7 Conclusion

We presented a 3D geological feature extraction method from multiple geophysical images, where negentropy of multiple physical properties is maximized as a criterion of Fast-ICA for the geological source separation. The methodology is tested through simulation of synthetic models. We showed that in the presence of non-gaussian geological noises, the negentropy maximization is superior to the variance and kurtosis maximization. We also showed that increasing the sharpness of the inversions produces sharper physical property images and improved the performance of the feature extraction method.

The advantage of this methodology is that the simulated petrophysical system allows considering the geological features as spatially coexisting patterns inside multidimensional physical properties. Interpretation of these kinds of complicated and mixed petrophysical systems is a challenge to post-inversion qualitative geophysical interpretations. We simulated a petrophysical system with multiple physical properties that are images of overlapped geological features, including a complex background geology and two chronologically distinct chemical alteration overprints on rock units. We show that the feature extraction through ICA is a useful tool for post-inversion semi-automatic interpretations which requires no prior geological or petrophysical information for geological feature extraction.

#### 4.8 Acknowledgments

The authors acknowledge financial support from NSERC (Natural Sciences and Engineering Research Council of Canada) and FRQNT (Fonds de recherche, Nature et technologies du Québec).

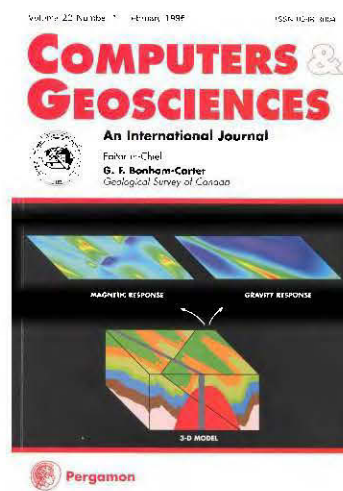


## CHAPTER V

### 3D SUPERVISED SPECTRAL FEATURE SUBSET SELECTION

Bahman Abbassi and Li Zhen Cheng

This paper will be submitted to Computer and Geoscience in November 2018



## Résumé

L'interprétation automatisée de plusieurs images géophysiques 3D est un sujet important dans l'interprétation de données volumineuses et la reconnaissance de formes multivariées. Dans le chapitre précédent, nous avons introduit la maximisation négentropique des propriétés physiques comme un moyen de découvrir des modèles géologiques latents à l'intérieur des images de propriétés physiques 3D. Dans cette section, nous proposons un algorithme d'intelligence artificielle supervisée généralisée qui cherche à reconstruire des cibles géologiques limitées d'observations de forages à partir d'images géophysiques 3D. Le Fast-ACI grâce à la maximisation négentropie fournit un ensemble de composants indépendants 3D qui sont séparés au maximum. Cependant, les spectres de fréquence de chaque image indépendante de composants englobent des caractéristiques interdépendantes qui sont habituellement invisibles au cours du processus d'apprentissage de réseau neuronal traditionnel. Dans cette section, une transformée continue en ondelettes est utilisée pour décomposer les composants indépendants des propriétés physiques, puis la maximisation de la négentropie a été effectuée pour séparer les caractéristiques spectrales des variables latentes afin de nourrir le processus d'apprentissage du réseau neuronal. Contrairement aux modèles de réseaux neuronaux conventionnels qui sont alimentés avec toutes les fonctionnalités d'entrée disponibles pour apprendre des cibles spécifiques, un algorithme de sélection de sous-ensembles spectraux hybrides (SSSH) est proposé ici pour sélectionner automatiquement la combinaison optimale des caractéristiques spectrales des propriétés indépendantes. Une optimisation bi-objective utilisant l'algorithme génétique a été incorporée pour minimiser une fonction objective globale qui tient compte à la fois des poids de réseau neuronal et du nombre de caractéristiques d'entrée spectrales pour l'apprentissage de la régularisation. L'algorithme d'apprentissage spectral est formé, testé et évalué sur le système épithermal de Newton et montre une capacité robuste dans la prédiction 3D de cibles géologiques, y compris les

concentrations de forage Au et les lithotypes mafiques à felsiques provenant de multiples images de propriétés physiques. Comparés aux méthodes d'interpolation 3D conventionnelles, telles que le maillage direct 3D et le krigeage, les modèles géologiques 3D récupérés avec l'apprentissage spectral ajoutent une valeur prédictive à notre entreprise géologique dans des endroits sans information de forage.

## Abstract

Automated interpretation of multiple 3D geophysical images is an important topic in large data interpretation and multivariate pattern recognition. In the previous chapter, we introduced the negentropy maximization of physical properties to uncover latent geological patterns inside 3D physical property images. In this section, we propose a generalized supervised artificial intelligence algorithm that seeks to rebuild geological targets from 3D geophysical images. The ICA through negentropy maximization provides a set of 3D independent components that are maximally separated. However, the frequency spectra of each independent component image encompass interdependent features that are usually unseen during traditional artificial neural network (ANN) learning process. A continuous wavelet transform is used to decompose the independent components of physical properties, and then negentropy maximization was performed to separate spectral features of latent variables to feed the ANN learning process. Unlike conventional ANN models that are supplied with all available input features to learn specific targets, a feature subset selection (FSS) algorithm automatically selects the optimum combination of spectral features from independent components of the physical properties. A bi-objective optimization using a genetic algorithm (GA) is incorporated to minimize a global objective function that considers both ANN weights and number of spectral input features for learning regularization. The spectral learning algorithm is trained, tested and evaluated on Newton epithermal system and shows a robust capability in the 3D prediction of geological targets, including borehole Au concentrations and mafic to felsic lithotypes from multiple physical property images. Compared to conventional 3D interpolation methods such as 3D direct gridding and kriging, the 3D geological models recovered with spectral learning add predictive value to our geological understanding without borehole information.

## 5.1 Introduction

A fundamental problem in integrated geophysical interpretation is the proper geological understanding of multiple inverted physical property images, which demands high dimensional techniques for extraction of geological information from modeled physical property images. Study of seismic attributes is an example of high dimensional pattern recognition that seeks to extract relevant geological features from broadband seismic data (Brown, 1996; Chen and Sidney, 1997; Chopra and Pruden, 2003; Lindseth, 2005; Chopra, 2008; Hall, 2016). In mineral exploration, treatment of multiple non-seismic data also put forth a similar pattern recognition problem, which seeks to extract relevant geological features from modeled potential field and electromagnetic data in the form of multiple 3D physical property images.

Several techniques are available for feature extraction in the high dimensional space, and this can be seen as a dimensionality increase problem that consequently leads to an overload of information (Murtaugh et al., 2000). Spectral decomposition of geophysical images, for example, provides a robust way for feature extraction in the frequency domain (Sinha et al., 2005; Castagna and Sun, 2006). However, the underlying patterns inside the high dimensional images are just related to certain frequencies, and sometimes most of the decomposed spectra are redundant. The question is that which frequency or frequency ranges are geologically relevant. This, in turn, can be seen as a dimensionality reduction problem, in which one tries to extract the best representative components of high dimensional images to facilitate the visual interpretations and machine learning optimization (Liu and Motoda, 2012).

Conventionally, high redundancy in the spectral domain is treated by incorporation of principal component analysis (PCA) to extract the principal components of multiple images (Hyvärinen and Oja, 2000). In the previous chapter, we explained why PCA is

not a good choice for separation of overlapped features inside multiple physical property images. Alternatively, independent component analysis (ICA), specifically the negentropy maximization approach was proposed as a robust tool in the separation of background lithotypes from alteration events (chapter IV). However, the spectra of the independent components still contain certain hidden overlapped features in different frequencies. Honório et al. (2014) utilize a similar approach for visualization of seismic broadband data in different frequencies. They used ICA to maximize non-gaussianity of the decomposed seismic frequency volume and stacked the resulting independent components in three red, green and blue (RGB) channels. The single RGB image provided a better way to delineate a sedimentary channel system. However, their approach involves manual selection and stacking of representative independent components of the decomposed seismic data.

Extraction of spectral features provides a way to feed machine learning algorithm with more detailed features, but the problem of “relevance” is still unsolved. Also, it is challenging to decide how much dimensionality reduction is necessary to present the most prominent spectral features to machine learning algorithms. Feature subset selection (FSS) provides a powerful tool for intelligent dimensionality reduction and feature learning (Zhao and Liu, 2011; Liu and Motoda, 2012). FSS reduces the size of a large set of the input features to a new set of relatively small and representative input features that improve the accuracy of ANN prediction. Therefore, unlike conventional statistical dimensionality reduction methods that are blind source separation algorithms, there is a criterion for selection of the best features that can be expressed as optimization of the neural learning process, in the light of the optimization of both neural weights and number of selected input features (Zhao and Liu, 2011).

The spectral feature subset selection (SFSS) procedure in this study is seen as a bi-objective optimization problem in which both the ANN weights and number of the

selected features are updated in different iterations. Several heuristic algorithms are known that solve these kinds of multi-objective optimization problems, such as genetic algorithms (Shapiro, 2002; Van Coillie et al., 2007) and particle swarm optimization (Clerc, 2013). We use a bi-objective genetic algorithm (GA) optimization to optimize the ANN weights as well as to find the most adaptable combination of input spectral features in the supervised machine learning procedure. The advantage of this approach is that it can direct the learning of ANN in a way that only a relevant set of input features are allowed to be used during the learning process.

The predicted outputs of this SFSS program are the estimated geological targets, as well as selected sets of spectral features related to each geological target. The selected features and predicted targets also provide a unique way for interpreters to see which spectral features inside physical properties are prominent in relation to certain geological targets.

## 5.2 Theory and methods

Our proposed 3D spectral FSS algorithm works for not only dimensionality reduction but also the separation of high dimensional spectral overlapped features. We offer an algorithm that automatically selects the best representative components based on multi-objective machine learning optimization. However, FSS demands several preprocessing steps that are explained in the previous chapters of this thesis, including 3D inversion of geophysical data and 3D feature extraction methods.

It is evident that the accuracy of geophysical modeling is critically important in the subsequent feature extraction and selection procedures. 3D inversion algorithms are dedicated to tackling this problem. As we discussed in chapter two and three of this Ph.D. thesis for the Newton epithermal deposit, the cooperative inversion can enhance the inverted physical property images. Even if the geophysical inversion provides the

most accurate physical property distributions, each physical property image provides only partial information about subsurface geology. We modeled this phenomenon through a linear mixing process in chapter four and proposed an independent component analysis through negentropy maximization to reconstruct the hidden geological features from multiple physical property images. The advantage of this method is that it can separate the host geology from alteration overprints in a multidimensional physical property space.

Subsequently, spectral decomposition reveals many latent features that are not properly visible in the spatial domain. The major difficulty arises in extraction and selection of the spectral features, due to the statistical interdependence of features in various spectra. Spectral decomposition of images also overloads the computational cost of interpretation and demands a methodology to pick the best spectral representation of images.

The algorithm proposed in this chapter is based on the results introduced in chapters II, III and IV, plus spectral feature extraction and feature selection algorithms presented in this chapter in the MATLAB environment. Thus, the whole process involves five major phases (Figure 5.1):

1. 3D inversion of geophysical data (chapters II and III)
2. Separation of physical properties through ICA (chapter IV).
3. Spectral decomposition of independent components through a continuous wavelet transform (CWT).
4. Dimensionality reduction and separation of raw spectral features through ICA.
5. SFSS based on a supervised ANN feature selection algorithm optimized by a multi-objective genetic algorithm (GA).



The objective is to present a robust way to train ANN with automatically selected input spectral features to predict specific geological targets. In the following sections, we demonstrate the wavelet feature extraction methodology as well as ANN optimized by GA.

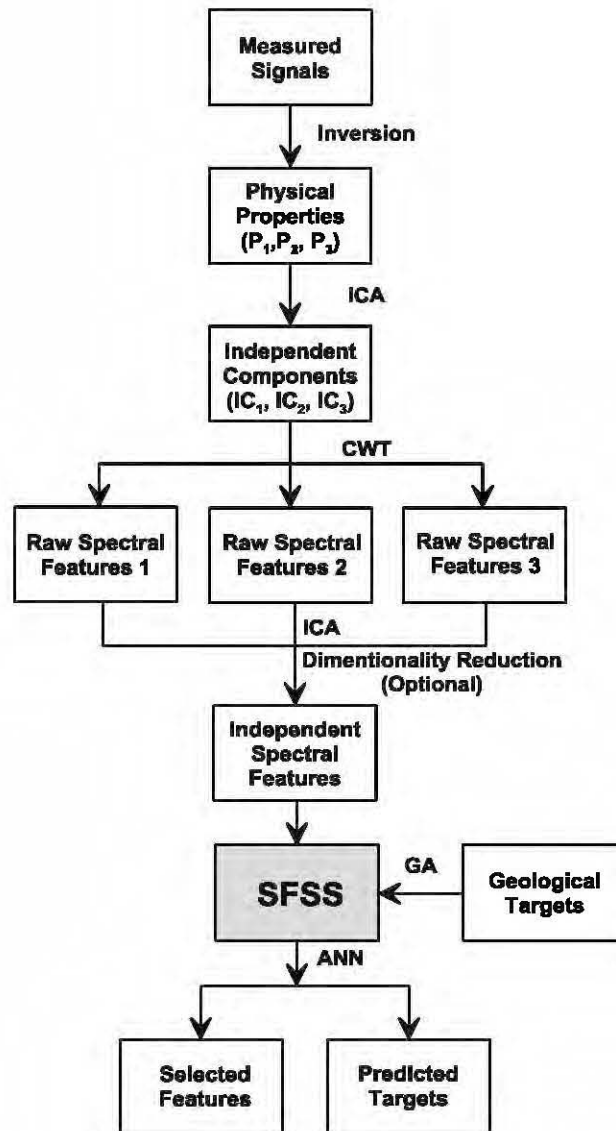


**Figure 5.1** Workflow of feature selection algorithm designed for geological interpretation.

### 5.2.1 Wavelet-ICA feature extraction

Continuous wavelet transforms (CWT) has been applied in various fields, as an alternative to Fourier analysis for feature extraction (Kumar, 1997; Moreau et al., 1997; Li et al., 2006; Liu, 2009). As small packets of waves, wavelets are defined by a specific frequency and decay towards either end. Therefore, the wavelet transform, in contrast to the Fourier transform, uses base functions (wavelets) with smooth ends (Lau and Weng 1994, Mackenzie et al. 2001). Since wavelets can be stretched and translated in both frequency and space, they can easily map changes of underlying features in the spatial-frequency domain. In other word, instead of dividing the images into overlapping segments and computing the power spectrum for each segment, the wavelet transform uses short packets of waves that better map local changes in the images (Trauth, 2015).

Mathematically, the 2D CWT of an image  $I(x, y)$  is defined as a decomposition of  $I$  on translated and dilated mother wavelet  $\psi(x, y)$ . Thus, the 2D CWT coefficients are given by:

$$C_s = (b_1, b_2, a) = \frac{1}{\sqrt{|a|}} \iint S(x, y) \psi^* \left( \frac{x-b_1}{a}, \frac{y-b_2}{a} \right) dx dy \quad (V.1)$$

Where  $b_1$  and  $b_2$  are defining the spatial translation,  $a > 1$  is the scale, and  $\psi^*$  is the complex conjugate of the mother wavelet  $\psi(x, y)$ .

In this study, a 2D implementation of CWT is used in MATLAB environment to calculate spectral features of 3D physical properties' independent components for successive horizontal slices. A Mexican Hat mother wavelet is used to calculate the wavelet coefficients of the 2D images (Figure 5.2):

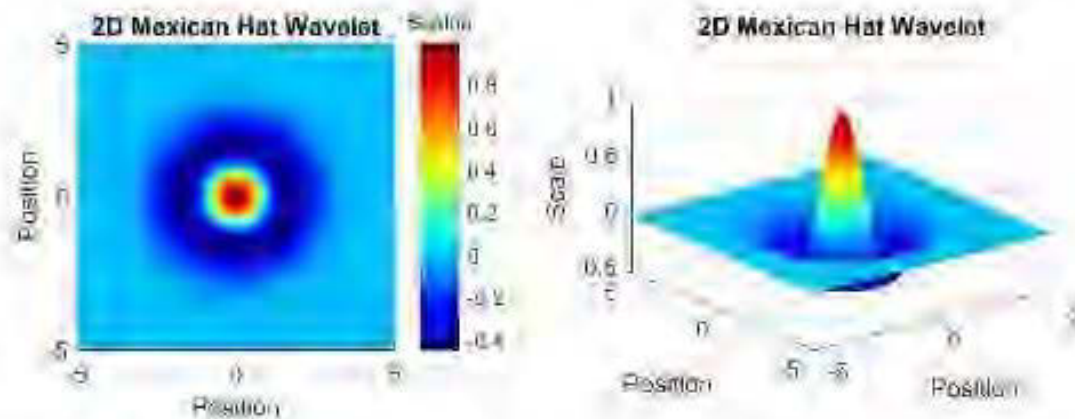


**Figure 5.2** 2D Isotropic Mexican Hat mother wavelet. The left figure is the plan view of the right figure.

$$\psi(x, y) = (x^2 + y^2 - 2)e^{-\frac{1}{2}(x^2 + y^2)} \quad (V.2)$$

### 5.2.2 Supervised artificial neural networks (ANN)

ANNs have been used vastly in nearly all areas of scientific and engineering disciplines. ANNs have already been treated as a nonlinear alternative to traditional models for pattern classification, time series analysis, and regression problems (Bishop, 1995; Benitez, 1997; Zhang, 2007; Siddique and Adeli, 2013). The ANNs are highly adaptive, and the network can learn from experiments in the training process. This data-driven approach is highly applicable to any real-world problem where theory on the underlying relationships is scarce or difficult to prescribe, but data are abundant or easy to gather (Bishop, 1995). ANNs are universal approximators, and this capability is significant because many problems in exploration geophysics such as pattern recognition, classification, and predictive modeling can be treated as function approximation problems.

Essentially, an ANN is a mathematical tool inspired by biological NNs, consists of many interconnected artificial neurons as its building blocks. Each neuron is connected to the other neuron with a numerical synaptic weight. Training is merely the process of adjustment of these interconnected weights in a way that it produces a meaningful output, compatible with our targets (expensive geological observations in this study).

Various ANN algorithms are evolved for evaluating the complex relationships in science and engineering. The most general and most widely used ANN model is the Multi-Layer Perceptron (MLP). The basic building block of this model is the Perceptron, a mathematical analog of the biological neuron, first described by Rosenblatt (1962). In this model as is shown in Figure 5.3, the integrated weights and biases of input vectors ( $x$ ) are activated by a sigmoid function (activation function) to produce the output ( $y$ ):

$$y = \frac{1}{1 + e^{-k \cdot \sigma}} \quad (\text{V.3})$$

In which  $\sigma = \sum_{j=1}^R w_j \cdot x_j$  and  $k$  is the factor determining the shape of the sigmoid.  $R$  is the number of inputs.

In Figure 5.4, an MLP structure is shown. After setting the initial weights randomly, the network is ready to train. Then, the output will be compared to the target in an iterative process, adjusting the weights of the ANN. This can be done by defining a Performance or Objective Function ( $E$ ) and minimizing it over  $N$  training samples.  $E$  is defined as least mean square (LMS) of the output vector ( $y_i$ ), and the desired output or the target vector ( $t_i$ ):

$$E = \frac{1}{N} \sum_{i=1}^N (t_i - y_i)^2 \quad (V.4)$$

The MLP networks are useful in parameter estimation of extremely complex problems in earth sciences. To separate two or more groups of patterns in our input data is an important classification problem in many fields of science and engineering. Sometimes it is straightforward to separate two groups of geophysical patterns linearly, but sadly, most signatures in large data sets are not linearly separable (Haupt, 2009).

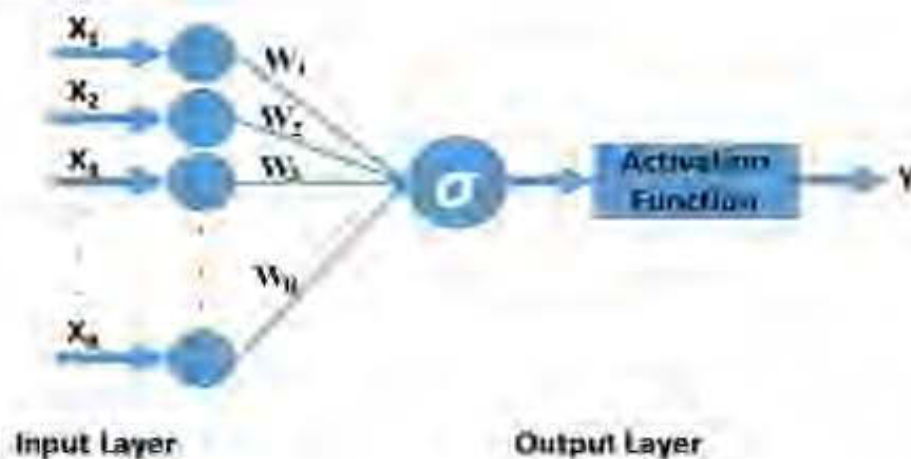


**Figure 5.3** A simple perceptron maps a set of inputs ( $X_R$ ) onto a specific output ( $y$ ).

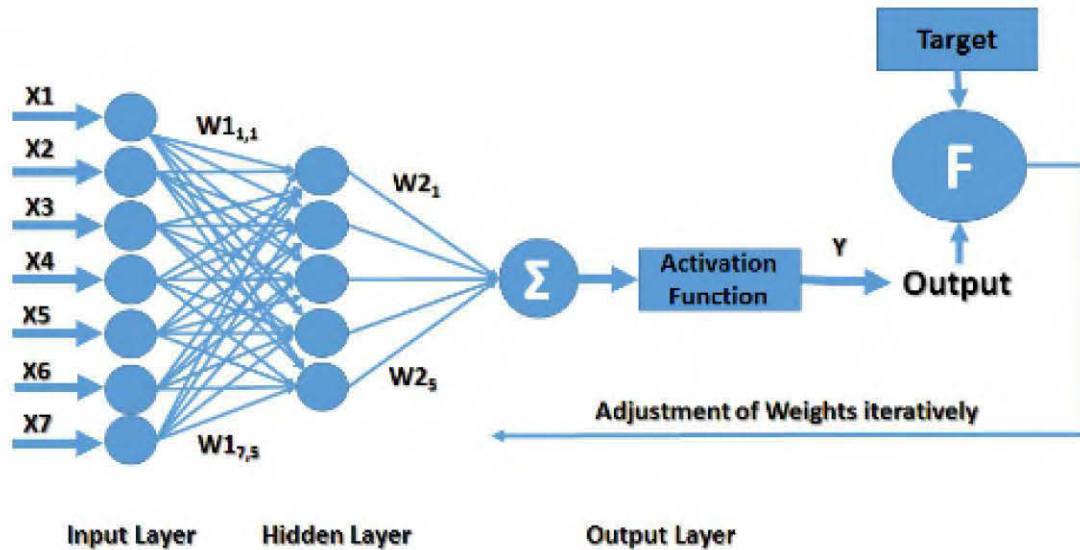


**Figure 5.4** A multilayer perceptron (seven inputs and five neurons in the hidden layer) maps a set of inputs ( $X_R$ ) onto an appropriate output ( $y$ ). Defining a performance function ( $F$ ) during the back-propagation process updates the synaptic weights to make output closer to the specified target.

Suppose, we are going to determine the lithological type of rocks based on physical properties (e.g., electrical resistivity and magnetic susceptibility). For example in Figure 5.5, physical properties of rocks in the left side can be separated linearly. However, in a more complex condition, instead of one straight line, we have to plot several lines to separate one class (the blue lithology) from others (the red lithology). ANNs can help us to do this process automatically for large number of data points. The extra lines can be created in the hyper-dimensions provided by the hidden layer of the network, separating different groups of patterns with any degree of complexity. That make ANNs universal pattern recognizers.

Despite successful applications of ANNs in nearly all branches of science and engineering, we still face many problems and potential pitfalls. A potential pitfall is over-fitting problem. Building too complex network (too many neurons and too many



iterations) sometimes gives us noisy outputs. On the other side, under-fitting would happen when too simple network is created that sometimes gives rise to underestimated values. Preprocessing of original data is also an important criterion. Random noises in inputs or targets can propagate through networks and disturb the outputs. For example, surficial noises in geophysical images can lead to under-estimation in final results. Smoothing the inputs and targets can reduce spurious effects, but it can also eliminate useful attributes in the images and this lead even to over-estimation in final models. Obviously, there is an optimum smoothness filtering strategy to avoid over-fitting and under-fitting effects (Zhang, 2007; Siddique and Adeli, 2013).

Choose an efficient algorithm is critical because a suitable learning algorithm can make a considerable difference in final estimations. Levenberg-Marquardt optimization technique (Marquardt, 1963, Nocedal and Wright 2006) is a robust technique for minimizing the performance function. This algorithm is a fast method for training ANNs (up to several hundred weights). It also has an efficient implementation in MATLAB, because the solution of the matrix equation is a built-in function in MATLAB environment (Siddique and Adeli, 2013).

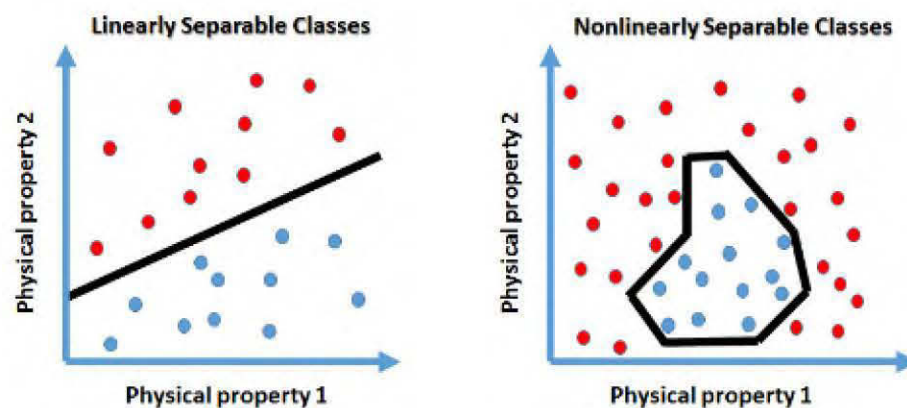


**Figure 5.5** Linearly (left) and nonlinearly (right) separable two-object classification problems.

Because of the local minima problem inherent in nonlinear optimization procedures, finding a global optimal or better local solution is the goal of an effective learning process. Several novel heuristic stochastic techniques are able to solve this complex hyper-dimensional optimization problem, including Ant Colony Optimization (Martens et al., 2007; Dorigo, 2004), Simulated Annealing Optimization (Tsuzuki, 2014), Particle Swarm Optimization (Clerc, 2013) and Evolutionary methods like Genetic Algorithms – GA (Haupt, 2004). In this study, we use a GA optimization technique to simultaneously minimize the ANN cost function as well as the number of input features (see section 5.2.3).

### 5.2.3 Spectral FSS optimization through GA optimization

One of the advanced algorithms for feature selection is the genetic algorithm (GA). GAs mimic the evolutionary process of natural selection and mutation in living organisms to solve nonlinear optimization problems (Haupt, 2004). In GAs, calculations begin with initializing the input parameters that we wish to optimize. These considerations are codified in an objective function or cost function with different weights depending on the survivability of individuals. The best-fitted individuals meet the specifications of the objective function and survive, while the rest of the population extinct (Gen and Cheng, 1997).

In GAs, the optimal solution emerges out of parallel processing among the population with complex fitness landscape. The whole idea is moving the population away from local optima that classical hill climbing techniques usually might be trapped in. This makes GA an extremely robust global optimization technique that can resolve the traditional problem of local pockets existing in older optimization routines (Haupt, 2004). The GA algorithm used in this study consists of four steps (Gen and Cheng, 1997):



1. Initializing Population: Encoding the problem in a string of a random population.
2. Calculate fitness of each solution.
3. Select pairs of parent strings based on the fitness.
4. Generate a new population by random change (using crossover and mutation) until a new population has been produced.

The algorithm repeats step 1 to 4 until an optimal solution is achieved (Figure 5.6). If we reiterate the process of evaluation, selection, crossover, and mutation, the algorithm will get closer and closer to the optimal global solution. GAs can process a large number of variables. They provide a group of optimal as well as the single best solution (Global Optimal). They are excellent at finding global minimum rather than being trapped in local minima (Haupt, 2004).

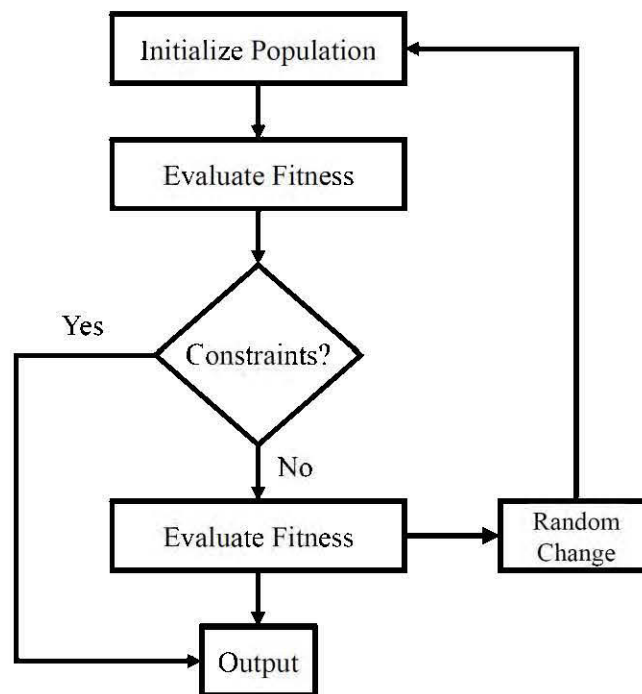


**Figure 5.6** A general GA flowchart. Random change includes crossover and mutation that produces new population better fitted to the environmental landscape.

Today, evolutionary methods are promising techniques in the field of AI, and GAs are universal solving problems tools in the economy, sociology, engineering, and environmental science. Haupt et al. (2009), enlisted many environmental applications of GAs. Xu et al. (2011) have presented an application of genetic programming to pipe failures modeling in water distribution systems. Matthews (2001) has applied GAs to multi-objective land-use planning. Several other applications are building empirical models of data, (Haupt, 2006), atmospheric data assimilation with a GA (Kalnay, 2003), and even using a GA to find steadily translating solutions of a highly nonlinear fifth order partial differential equation (Haupt et al., 2009). Some researchers also suggested that global search techniques like the GAs might help ANNs learning to move away from local minima (Tahmasebi and Hezarkhani, 2009).

However, some disadvantages are the lack of viable convergence criteria and the fact that they are not well known for their speed, However, through the careful choice of GA parameters, we can improve the speed of the optimization. Nevertheless, engineers, for example in the field of robotics, are concerned with speed; applied scientists are more interested to find a better solution using heuristic approaches to enhance the convergence. The GA is such an approach (Haupt, 2004).

In this study, we use an implementation of the Nondominated Sorting Genetic Algorithm (NSGA) proposed by Srinivas and Deb (1995) in the MATLAB environment. NSGA optimizes a global bi-objective cost function in the form of :

$$E_{Global} = f(E_{ANN}, n_f) \quad (V.5)$$

Where  $f$  is the global cost function operator. The bi-objective GA simultaneously minimizes the number of spectral features ( $n_f$ ) as well as neural networks cost ( $E_{ANN}$ ).

### 5.3 Results

We first ran several tests to justify and evaluate our SFSS algorithm on 2D images (Appendix B). This simulation helped us to make sure that the SFSS works and is superior to the conventional ANN predictions. Then we rewrote the MATLAB code to predict geological targets in 3D, in the case of 3D lithotype estimation, as well as 3D Au grade estimation. We show that the SFSS is able to reconstruct the 3D geological targets robustly and provides a set of selected spectral features that are well matched to the relevant geological targets in 3D.

We used data from Newton Gold deposit (Chapters II and III) to interpolate lithotypes and Au grade data using the SFSS algorithm. The 3D procedure is similar to the simpler 2D algorithm used in Appendix B, except that the calculations of raw spectral features are repeated for all horizontal slices. From unevenly distributed borehole data (Figure 5.7), the lithotype data and Au concentrations in g/t (Figure 5.8a and 5.8d) are used for Newton epithermal system characterization. The borehole lithotypes of the Newton deposit are sorted according to their magnetic properties from low magnetic felsic volcanic rocks and intrusions to high magnetic mafic volcanic rocks and diorites. Those data are interpolated with nearest neighbor (direct gridding) and kriging methods. As can be seen in Figure 5.8, the traditional interpolation methods are not able to add any new geological information in places without borehole data.

However, the SFSS algorithm presented in this study is able to compare the geophysical images to geological targets and learn how to reconstruct the targets from spectral features extracted from 3D physical property models. The physical property models are derived from cooperative inversion (Abbassi et al., 2018a, and Abbassi et al., 2018b) of magnetic and DC/IP datasets and are presented in Figure 5.9.

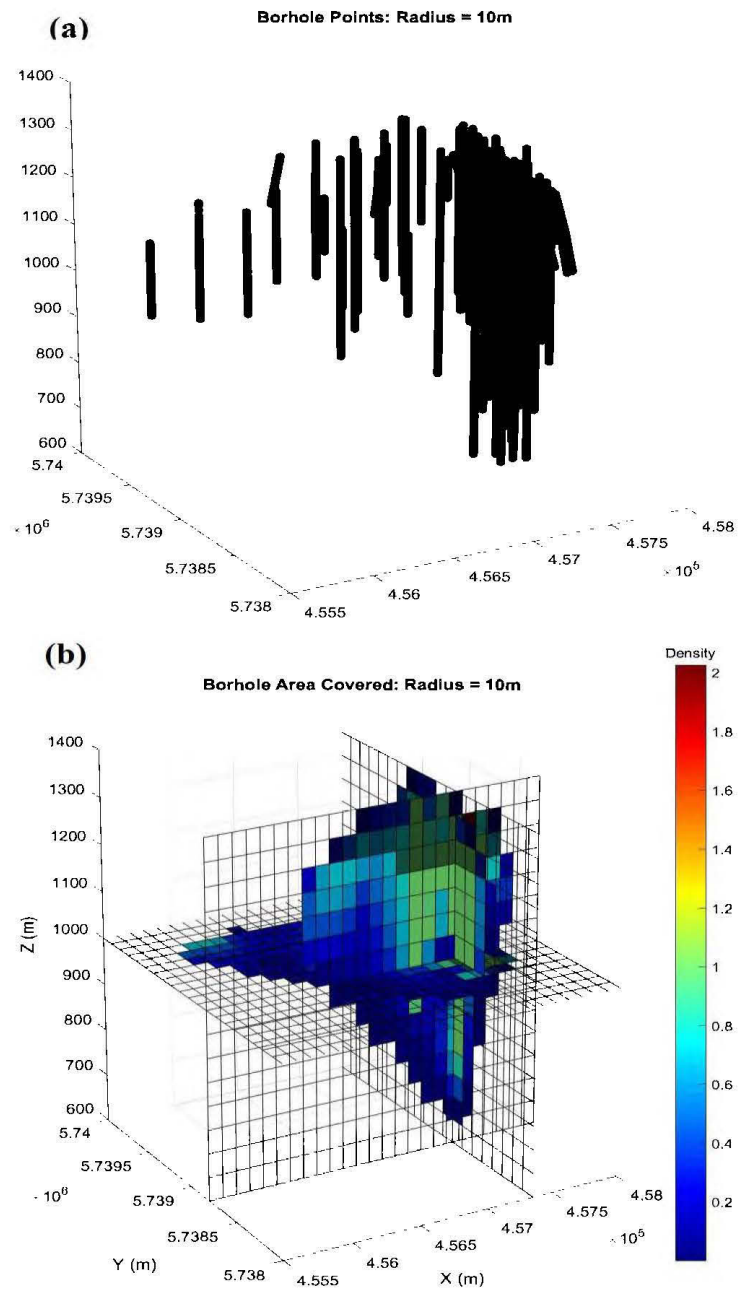


**Figure 5.7** Location of boreholes in Newton epithermal system (a), versus density of borehole data points in 3D (b). Borehole data are available in places with densities more than one. In places without data points, conventional interpolations methods do not work properly.

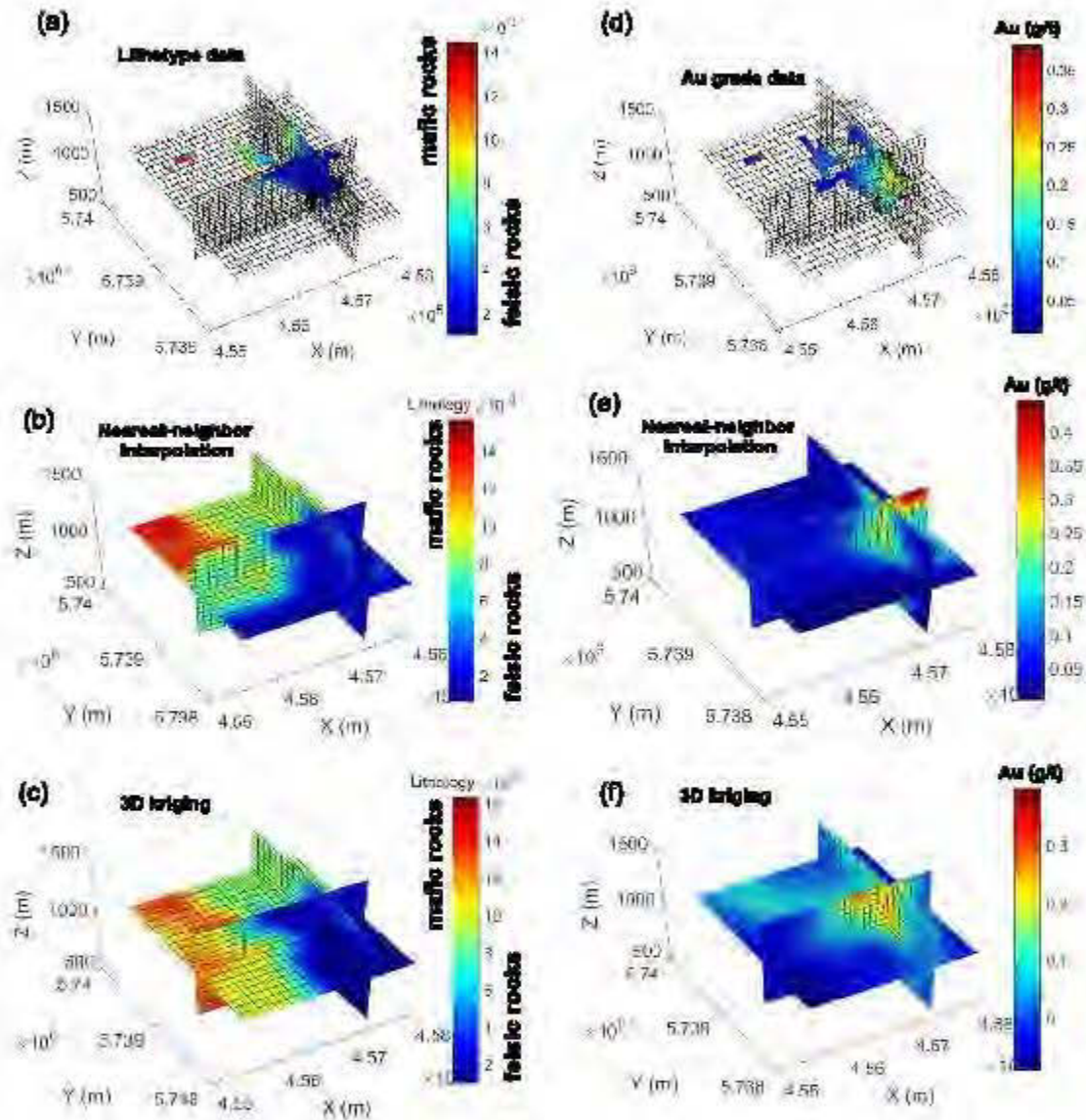


**Figure 5.8** Interpolation of geological targets with conventional methods. (a) Lithotype data (mafic/felsic). (b) Nearest-neighbor interpolation of lithotypes. (c) Kriging of lithotypes. (d) Au grade data. (e) Nearest-neighbor interpolation of Au grades. (f) Kriging of Au grades.

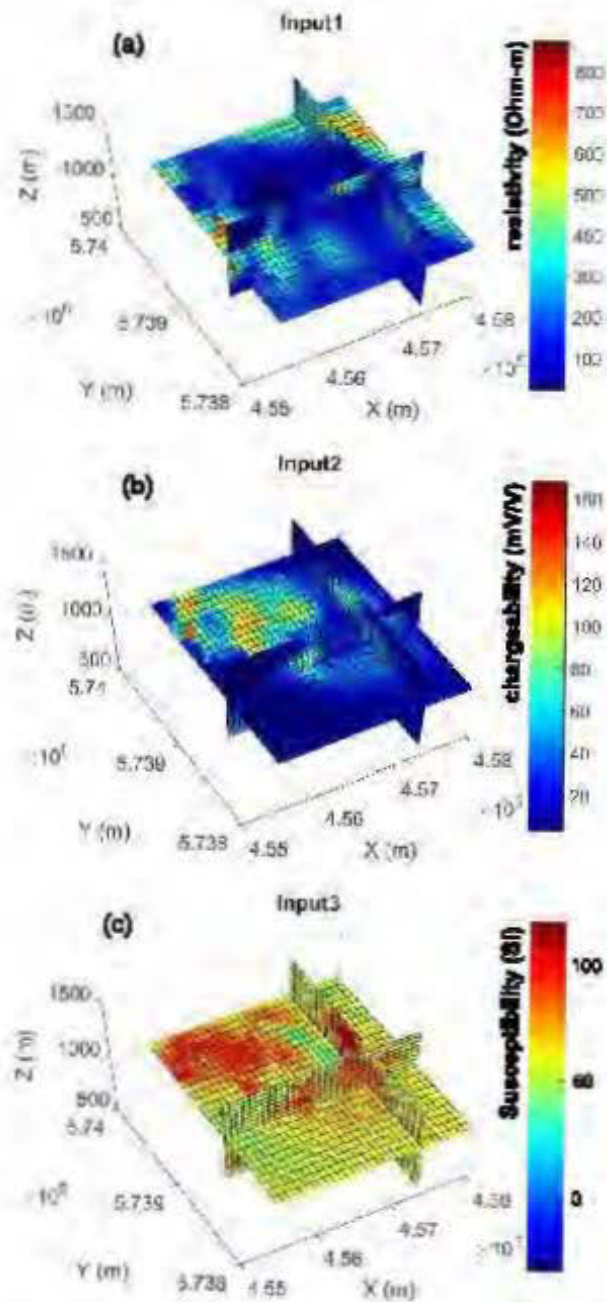


**Figure 5.9** Three inverted physical property models used as inputs of the SFSS algorithm.



A preliminary Fast-ICA separates the latent features inside the multiple physical property images. The results are shown in Figure 5.10, in the form of three negentropy optimized independent components.

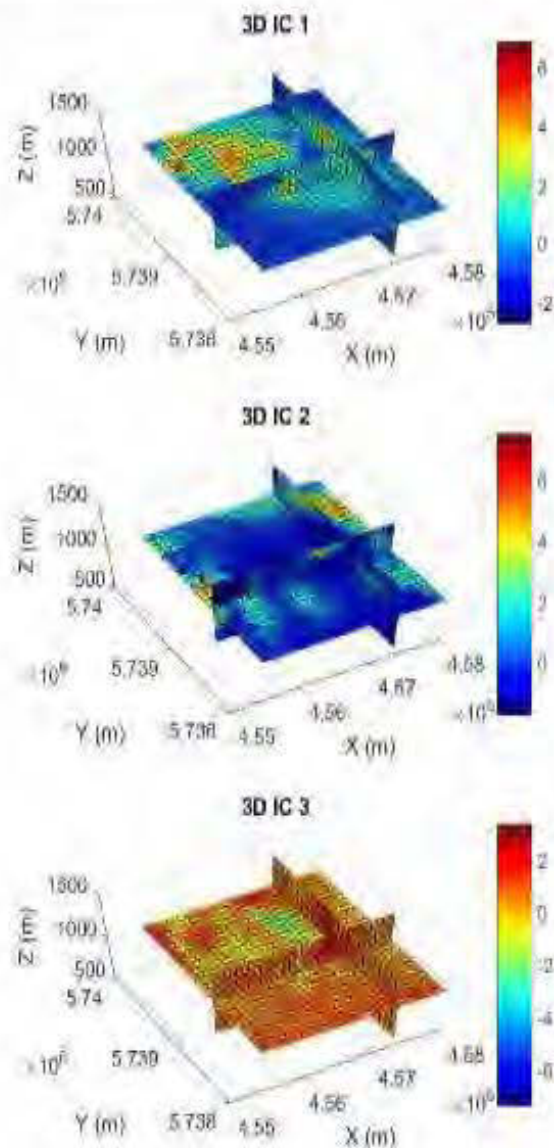


**Figure 5.10** Three independent components (ICs) of the physical properties calculated through negentropy maximization.

Then, three independent components are decomposed to form a set of raw spectral features through a continuous wavelet transform. We calculated the 2D wavelet coefficients for five scales and in 24 directions (every  $15^\circ$ ). We decided to use only five scales because we observed that for more than five scales the changes in low-frequency features (high scales) would disappear and there won't be any difference in the raw spectral features for scales more than five. The 3D spectral decomposition is iterated for the three initial independent components and has produced 360 ( $5 * 24 * 3$ ) raw features containing several frequency-dependent raw features that are needed to be extracted further. Figure 5.11 demonstrates the raw spectral features sliced at the elevation of 1000 m.

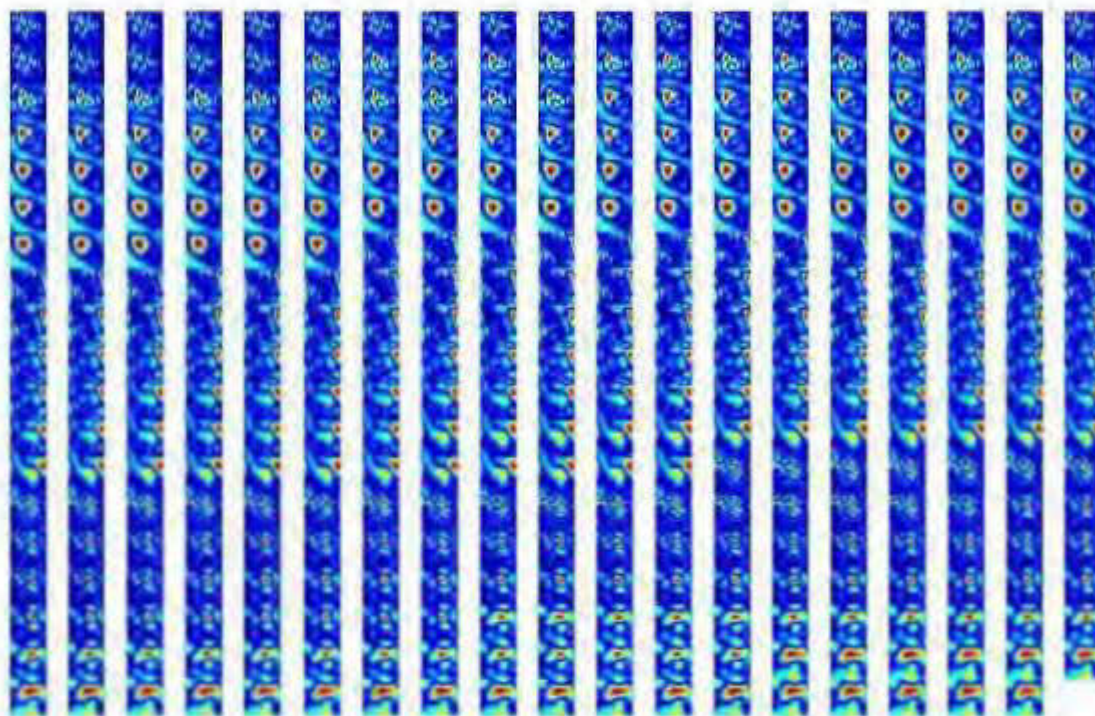


**Figure 5.11** Raw 3D spectral features produce by CWT with 5 scales in 24 directions ( $0^\circ, 15^\circ, 30^\circ, 45^\circ, 60^\circ, 75^\circ, 90^\circ, 105^\circ, 120^\circ, 135^\circ, 150^\circ, 165^\circ, 180^\circ, 195^\circ, 210^\circ, 225^\circ, 240^\circ, 255^\circ, 270^\circ, 285^\circ, 300^\circ, 315^\circ, 330^\circ, 345^\circ$ ). The extracted features are sliced at the elevation of 1000 m.



Fast-ICA through negentropy maximization separates 360 number of raw features to produce the 3D independent spectral inputs necessary for feature selection. The Fast-ICA algorithm here is also able to reduce the dimensionality of the raw features. The best strategy to reduce the dimensionality of features depends on two factors including computer hardware resources and stability of the SFSS output. Low reductions result in high computational costs and severe reductions lead to loss of valuable information and results in poor predictions. There is always an optimum way to moderately reduce the dimensionality of features through several testing and running the algorithm by user. In cases where there is no hardware limitation, this trial and error strategy is not necessary. We ran the SFSS algorithm two times in parallel for prediction of lithotypes and Au grades. For feature selection, we used an MLP network with independent spectral features as inputs, 20 neurons in the hidden layer, maximum 30 iterations, and one output. 70% of the borehole data are used for training, and the rest is used for testing and evaluation. The GA is iterated in 20 generations with 20 population, 70% crossover, 40% of mutation and mutation rate of 0.05.

In the case of lithological predictive modeling, the dimensionality of the raw spectral features is reduced to 120 features to decrease the computational cost of the SFSS (Figure 5.12).

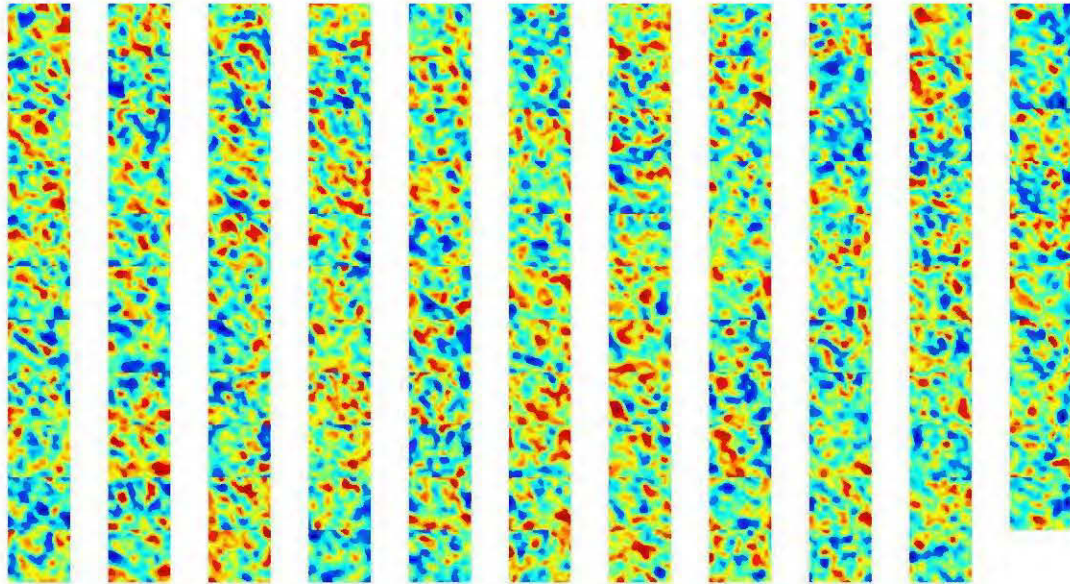


**Figure 5.12** Total 120 number of separated 3D spectral features after Fast-ICA dimensionality reduction for lithological feature selection. The extracted features are sliced at the elevation of 1000 m.

For the lithotypes model reconstruction, evaluation results are compared for both conventional ANN optimized with the Levenberg-Marquardt method, as well as SFSS algorithm optimized with GA (Figure 5.13). As can be seen, the SFSS algorithm gives a better evaluation result with 89% R-squares of the predicted results versus the target values.

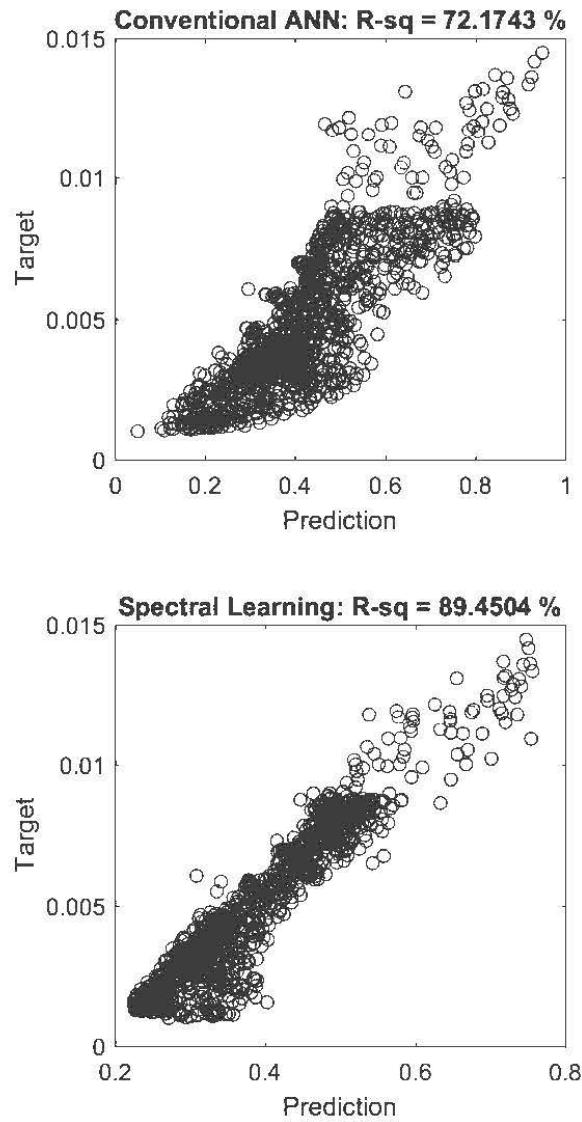


**Figure 5.13** Evaluation of lithotype prediction for ANN and FSS algorithms. R-sq denotes the R-squared values.

The error landscape of the lithotype prediction by SFSS is also shown in Figure 5.14. As can be seen, the best results (least global error indicated by blue color) come after the generation 10 of GA, and for the last generation, SFSS algorithm selects 78 features

for spectral learning (Figure 5.15). As can be seen, the SFSS can recover a much better lithological model, compatible with prior information (compare Figure 5.15b to Figure 3.3). The selected features are also shown in Figure 5.16.

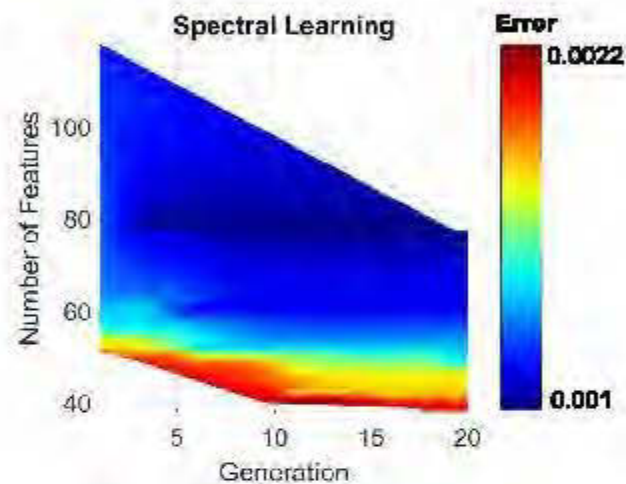


**Figure 5.14** The bi-objective error landscape of SFSS algorithm during lithotype estimation.

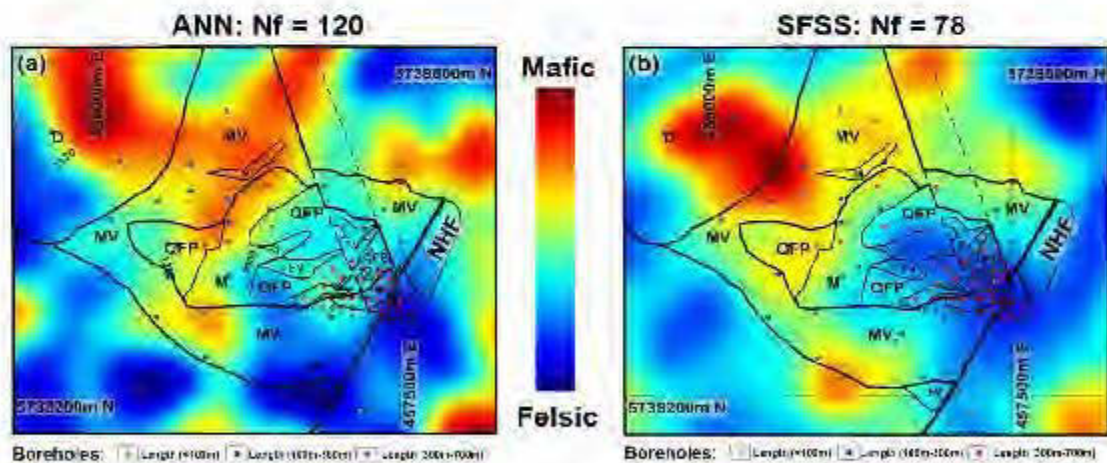


**Figure 5.15** Lithotype predictions: Results of 3D ANN prediction (a) versus 3D SFSS predictions (b). SFSS resulted in the better reconstruction of lithotypes with less number of input spectral features ( $N_f = 78$ ). Results are sliced horizontally at the elevation of 1000 m.



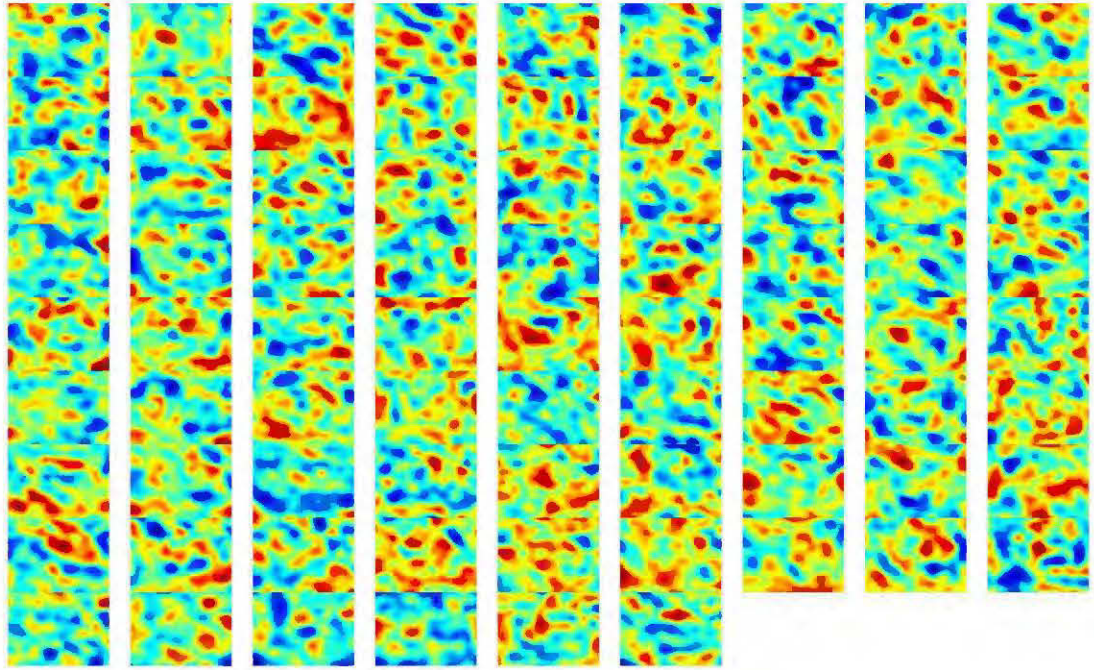


**Figure 5.16** Total 78 number of 3D selected features used for lithotype prediction. The selected features are sliced at the elevation of 1000 m.

For Au grade prediction, the same network parameters are used, except that this time, the Fast-ICA dimensionality reduction has reduced the number of independent spectral features to 108 (Figure 5.17).

Evaluation results are compared for both conventional ANN optimized with the Levenberg-Marquardt method, as well as SFSS algorithm optimized with GA (Figure 5.18). As can be seen, the SFSS algorithm gives a much better evaluation result with 89% R-squares of the predicted results versus the target values, compared to poor results of the conventional ANN with 33% R-squares.

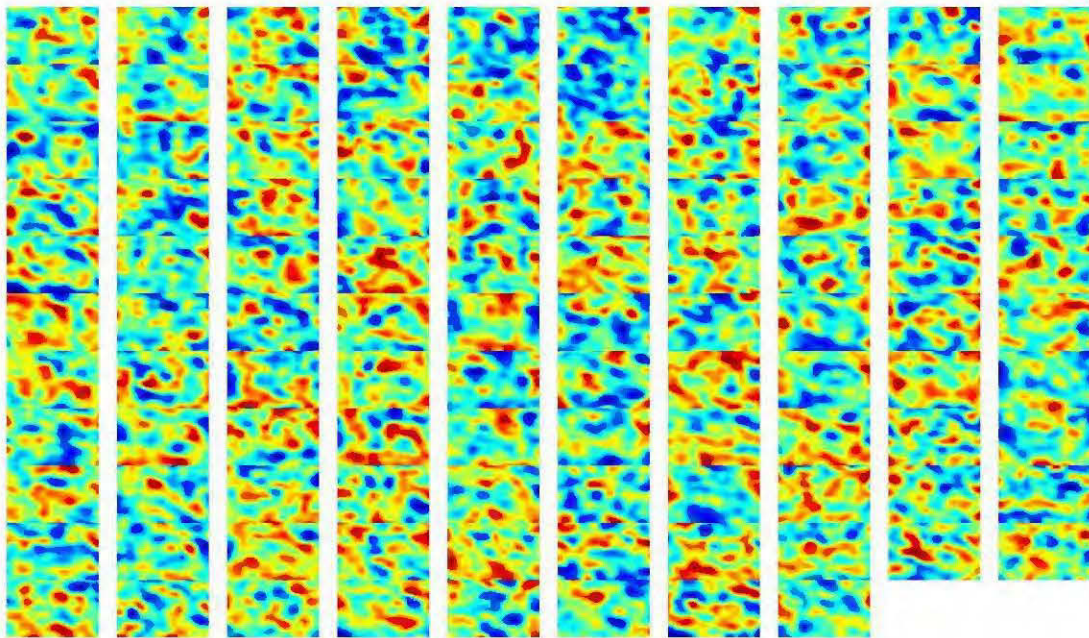


**Figure 5.17** Total 108 number of separated 3D spectral features after Fast-ICA dimensionality reduction for Au grade feature selection. The extracted features are sliced at the elevation of 1000 m.

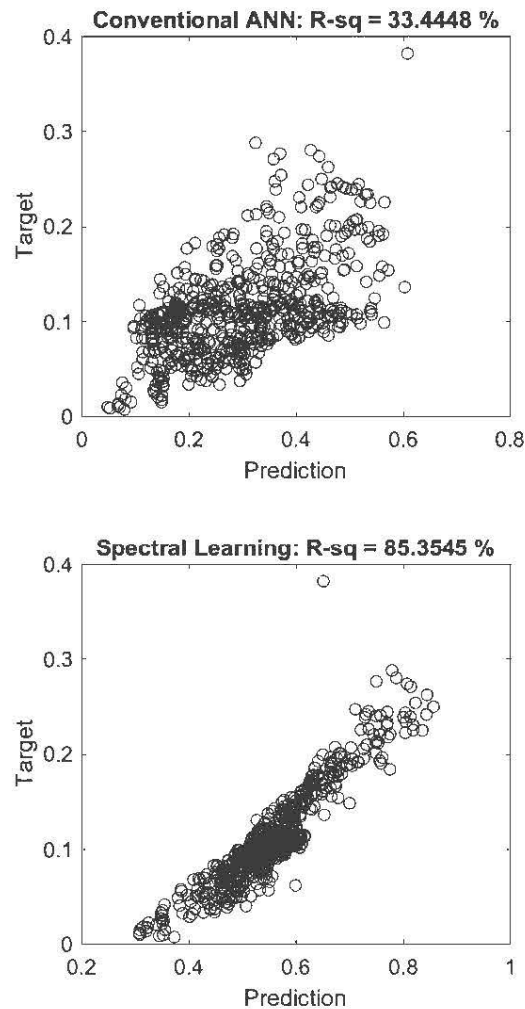


**Figure 5.18** Evaluation of Au grade prediction for ANN and FSS algorithms. R-sq denotes the R-squared values.

The error landscape of the Au grade prediction by SFSS is also shown in Figure 5.19. As can be seen, the best results (least global error indicated by blue color) come after the generation ten of GA, and for the last generation, SFSS algorithm selects 96 features for spectral learning (Figure 5.20). The SFSS is able to recover a much better Au grade model compared to conventional ANN estimations. The SFSS selects 96 out of 108



features (Figure 5.21), which means 12 spectral features were extremely redundant in the prediction of Au concentrations.

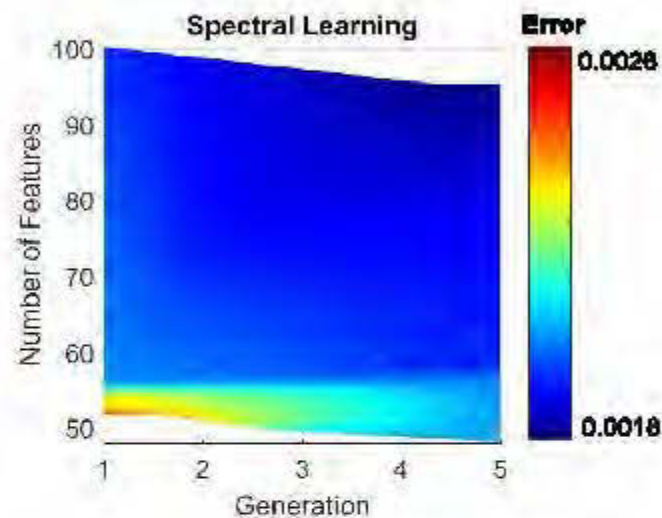


**Figure 5.19** The bi-objective error landscape of SFSS algorithm during Au grade estimation.

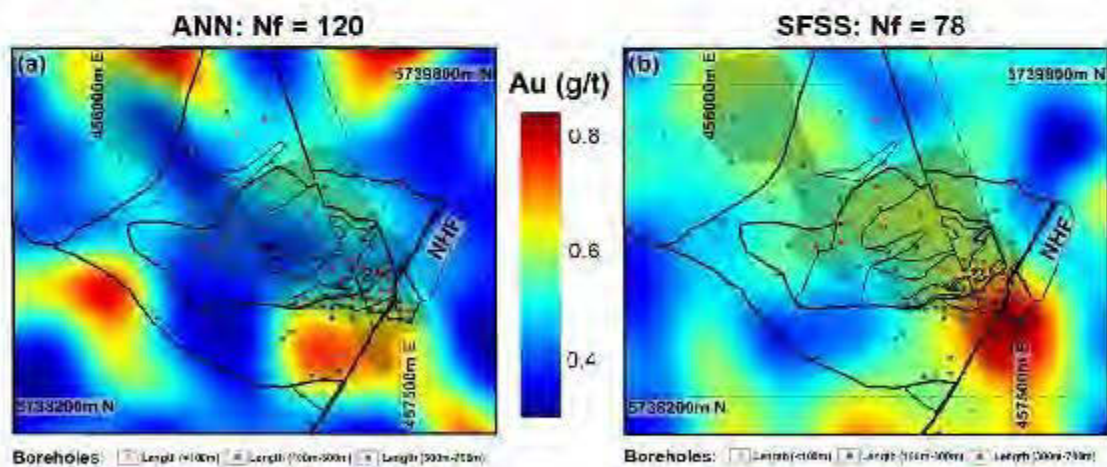


**Figure 5.20** Au grade predictions: Results of 3D ANN predictions (a) versus 3D SFSS predictions (b). SFSS resulted in better reconstruction of Au grade distributions with less number of input spectral features ( $N_f$ ). Results are sliced horizontally at the elevation of 1000 m. The gray shaded zone is the outline of mineralization.



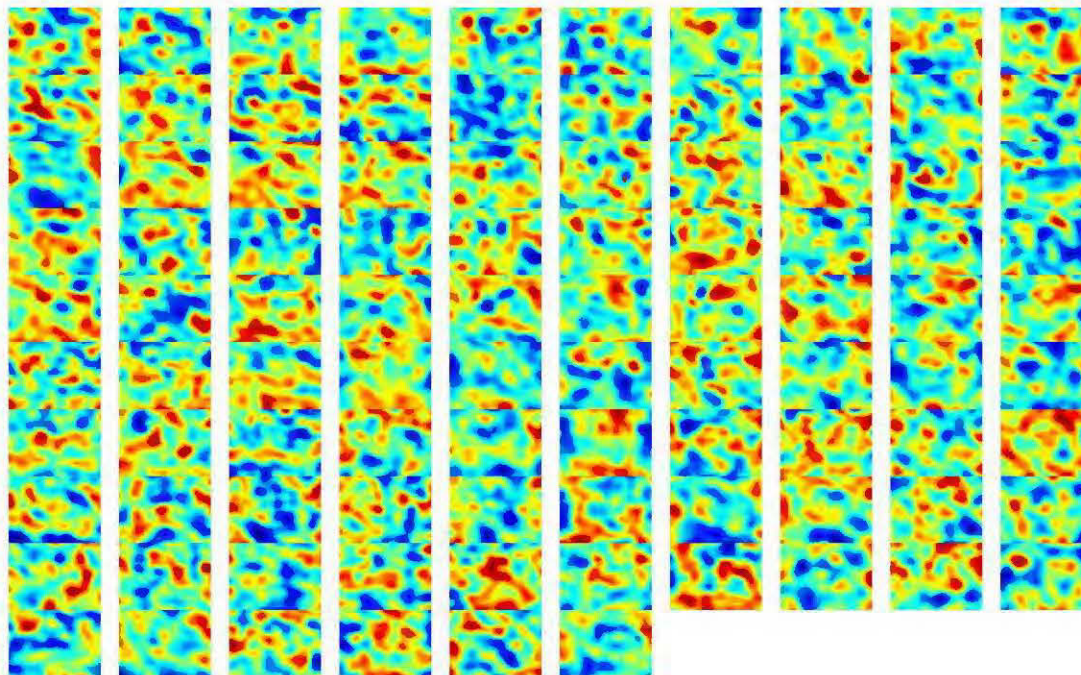


**Figure 5.21** Total 96 number of 3D selected features used for lithotype prediction. The selected features are sliced at the elevation of 1000 m.

## 5.4 Conclusion

In this chapter, we proposed a spectral feature selection algorithm for supervised learning of geological patterns to do 3D predictive modeling from 3D inverted physical properties. Our work is based on the synergy between the ICA and CWT feature extraction methods and multi-objective machine learning optimization through GA for feature selection. The spectral feature extraction method here provided the inputs of the feature selection algorithm, and we showed that our SFSS algorithm is able to pick the relevant spectral features that are necessary for 3D predictive modeling of the targets.

The practical implementation of the SFSS algorithm is also evaluated for an epithermal Au deposit in Canada (chapter II and III of this thesis). The results show the spectral learning scheme proposed can efficiently learn geological patterns to make predictions based on 3D physical property inputs. The SFSS also minimizes the number of the extracted spectral features and for each target learning case tries to pick the best representative geophysical spectral features. This also makes a possibility for interpreters to not only have a predictive model at the end but also have an understanding about the relevant (selected by SFSS) and irrelevant (features that are ignored by SFSS) features.

## 5.5 Acknowledgments

The authors acknowledge financial support from NSERC (Natural Sciences and Engineering Research Council of Canada) and FRQNT (Fonds de recherche, Nature et technologies du Québec).

## CHAPTER VI

### GENERAL CONCLUSION

In this Ph.D. thesis, new methodologies are tested and evaluated for 3D integrated interpretation of multiple geophysical images targeting mineral deposits. 3D inverse modeling of multiple geophysical data, multivariate statistics, and machine learning methods are used to develop a 3D integrated interpretation methodology.

In the first two chapter, we explored the challenges related to practical 3D inversion of geophysical data targeting the Newton epithermal Gold-Silver deposit in Canada. In chapter II, we used MVI modeling to recover the vector properties of rocks' magnetizations, combined with sharp inversion methods both for MVI and DC/IP inversions to recover the high-contrast variations of the subsurface physical properties. We showed that the accuracy of DC/IP inversion in the localization of a Gold-rich zone in Newton deposit provided a valuable constraint on the magnetic inversion, for better localization of the low susceptibility zone associated with mineralization. Therefore, we ran a cooperative inversion of multiple data sets based on this physical property coupling. The chargeability results were used to constrain the magnetic inversion. The recovered cooperative susceptibilities successfully located the magnetite destructive zone associated with the Au enrichments. The value of this methodology is that it does not necessarily need any prior information for physical property coupling. The coupling between susceptibilities and chargeabilities (or any other types of physical properties) can be tested through calculation of forward responses of them. This methodology is potentially reproducible in cooperative inversion between other geophysical methods with slight modifications.

In chapter III, we explored the geophysical properties of Newton deposit on the regional, prospect and deposit scale. In this chapter, we presented more geological and petrophysical details about the Newton deposit. Geophysical images identified several geological features successfully on different scales.

The cooperative magnetic-DC/IP inversion results were also used for petrophysical interpretation. Four petrophysical domains were inferred from cross-correlation of physical properties, detecting the footprints of the porphyritic intrusions, sulfide dissemination, magnetite-bearing alterations, and silicifications.

In chapter IV, higher order statistical algorithms are applied for geological source separation. A 3D geological feature extraction method was presented from multiple geophysical images, through maximization of negentropy of multiple physical properties as a criterion of Fast-ICA. The methodology was tested through simulation of synthetic models. We showed that the negentropy maximization is superior to the variance and kurtosis maximization in geological source separation. We also showed that increasing the sharpness of the inversions produces sharper physical property images and improved the performance of the feature extraction method. We show that the feature extraction through ICA is a useful tool for post-inversion semi-automatic interpretations which requires no prior geological or petrophysical information for geological feature extraction.

In chapter V, a machine learning algorithm is provided for semi-automatic interpretation of multiple geophysical images. We proposed a spectral feature selection algorithm for supervised learning of geological patterns to do 3D predictive modeling from 3D inverted physical properties. Our work is based on a synergy between the ICA and CWT feature extraction methods and multi-objective machine learning optimization through a genetic algorithm for feature selection. The spectral feature

extraction method here provided the inputs of the feature selection algorithm, and we showed that our SFSS algorithm is able to pick the relevant spectral features that are necessary for 3D predictive modeling of the targets. The practical implementation of the SFSS algorithm was also evaluated for an epithermal Au deposit in Canada (chapter II and III of this thesis). The results show the spectral learning scheme proposed is able to efficiently learn geological patterns to make predictions based on 3D physical property inputs. The SFSS also minimizes the number of the extracted spectral features and for each target learning case tries to pick the best representative geophysical spectral features. This also makes a possibility for interpreters to not only have a predictive model at the end but also have an understanding about the relevant (selected by SFSS) and irrelevant (features that are ignored by SFSS) features.

## APPENDIX A

### MATLAB PROGRAMS FOR 2D SFSS

#### A.1 Main MATLAB program: SpectralFeatureLearning.m

```
%% 2D SFSS

% This Matlab program is a two-dimensional version of the
Spectral Feature Subset Selection (SFSS).
% Author:
% Bahman Abbassi (bahman.abbassi@uqat.ca)
% Institut de Recherche en Mines et en Environnement (IRME)
% Université du Québec en Abitibi-Témiscamingue (UQAT)
% This hybrid program uses several default Matlab functions
including 2D interpolation functions, Continuous Wavelet
Transform (CWT) functions,
% as well as open source functions for Fast-ICA provided by
Brian Moore in
% https://www.mathworks.com/matlabcentral/fileexchange/38300-
pca-and-ica-package
% And Feature Subset Selection (FSS) functions from
http://matlabsite.com.
%-----
clc
clear all
close all

%% 1. All parameters:
%-----
Image1 = im2double(rgb2gray(imread('Image1_.png'))); % The
original images
Image2 = im2double(rgb2gray(imread('Image2_.png'))); % The
original images
Image3 = im2double(rgb2gray(imread('Image3_.png'))); % The
original images

Parameter = 1; % Just for display purpose...
resize = 0.2; % Image resize ratio
```

```

mu1 = 0; sigm1 = 5; skew1 = 1; kurt1 = 5;    %% Non-Gaussian
(Pearson) Noise added to Mixed PPs
mu2 = 0; sigm2 = 5; skew2 = 1; kurt2 = 4;    %% Non-Gaussian
(Pearson) Noise added to Mixed PPs
mu3 = 0; sigm3 = 5; skew3 = -1; kurt3 = 4;    %% Non-Gaussian
(Pearson) Noise added to Mixed PPs

numberoffeatures = 3;    % Number of Initial ICA Features: this
can be equal or less than the number of the original images.

sigma1 = 0.00001;        % Smooth the images
sigma1b = 0.25;          % Smooth the initial independent
components (ICs)
sigma2 = 0.00001;        % Smooth the wavelet spectra of the
ICs
sigma3 = 0.5;            % Smooth the separated spectra
sigma4 = 0.5;            % Smooth the 2D predicted pattern

Scale = 20;
Angle = 4;                % Number of directions where the mother
wavelet shift and expand during the CWT.
Scale_Expand = 1;        % Scale_Expand determines how the scale
values are sampled.
Scales = 1:Scale_Expand:(Scale*Scale_Expand); % The values
of the scales.
Freqs = 1000* scal2frq(Scales,'mexh',1);      % The
corresponding frequencies for mexican hat mother wavelet.
Angles = 0:180/Angle:180-180/Angle;           % The values
of the Angles (directions) in degree.
Angles = (Angles/180)*pi;                     % The values
of the Angles (directions) in radian.
DR = 0.5;          % ICA dimensionality reduction after CWT. Here
dimensionality is reduced to half.

r2 = round(DR * (numberoffeatures*Scale*Angle)) % Number of
independent spectral features: inputs of the FSS.

TrPercent = 70;        % Percentage of the data used for
training.
Neurons = 10;         % Number of the neurons in the hidden
layer.
NN_Iteration = 10;   % Number of the ANN optimization
iteratgions.

```



```

MaxIt = 5;          % Genetic Algorithm (GA) Maximum Number of
Iterations.
nPop = 10;         % GA Population Size
pCrossover = 0.7; % Crossover
Percentage
nCrossover = 2*round(pCrossover*nPop/2); % Number of crossovers
pMutation = 0.4;  % Mutation Percentage
nMutation = round(pMutation*nPop);    % Number of Mutants
mu = 0.1; % Mutation Rate: If SFSS algorithm didn't leave out
the redundant features, then increase the mutation rate for
more strict selection.

q1 = 0.75; % Inputs for training traverse 1: Direction of the
target pixels sampling.
q2 = 0.25; % Inputs for training traverse 2: Direction of the
target pixels sampling.
v1 = 0.75; % Target for training traverse 1: Direction of the
target pixels sampling.
v2 = 0.25; % Target for training traverse 2: Direction of the
target pixels sampling.

%% 2. The simulation of a mixing Process
%-----
Image1 = imresize(Image1, resize); Image1 =
imgaussfilt(Image1,sigma1);
[G, H] = size(Image1);
Image2 = imresize(Image2, [G H]); Image2 =
imgaussfilt(Image2,sigma1);
Image3 = imresize(Image3, [G H]); Image3 =
imgaussfilt(Image3,sigma1);

Image_targ = Image1;

[Noise1,type1] = pearsrnd(mu1,0.001*sigm1,skew1,kurt1,G,H);
% r = pearsrnd(mu,sigma,skew,kurt,m,n) m-by-n Pearson system
mean mu,
[Noise2,type2] = pearsrnd(mu2,0.001*sigm2,skew2,kurt2,G,H);
% standard deviation sigma, skewness skew, and kurtosis kurt.
[Noise3,type3] = pearsrnd(mu3,0.001*sigm3,skew3,kurt3,G,H);
% The parameters must be scalars.

type1
type2
type3

```

```

ImageMix1 = 0.2*Image1 + 0.5*Image2 + 0.3*Image3; ImageMix1 =
ImageMix1 + Noise1;
ImageMix2 = 0.35*Image1 + 0.2*Image2 + 0.45*Image3; ImageMix2
= ImageMix2 + Noise2;
ImageMix3 = 0.25*Image1 + 0.55*Image2 + 0.20*Image3; ImageMix3
= ImageMix3 + Noise3;

Images = cat(3,ImageMix1,ImageMix2,ImageMix3); % mixed images
matrix

fig('Name','Original Images and Mixed
Image','units','inches','width',10,'height',5,'font','Helvetic
a','fontsize',11)
subplot(2,3,1), imshow(Image1)
title('Image 1')
subplot(2,3,2), imshow(Image2)
title('Image 2')
subplot(2,3,3), imshow(Image3)
title('Image 3')
subplot(2,3,4), imshow(ImageMix1)
title('Mixed Image 1')
subplot(2,3,5), imshow(ImageMix2)
title('Mixed Image 2')
subplot(2,3,6), imshow(ImageMix3)
title('Mixed Image 3')

saveas(gcf,['InputImages_Mixed' num2str(Parameter) '.jpg'])

pause(0.5);

%% 3. Blind Source Separation (BSS): Fast-ICA for initial
separation of images
%-----
PPs = cat(3,ImageMix1(:), ImageMix2(:), ImageMix3(:)); PPs =
PPs(:,:); PPs = PPs';

[nFastICA_pp, WICA2, TICA2, muICA2] =
fastICA(PPs,numberoffeatures,'negentropy');
%{'kurtosis','negentropy'} specifies which flavor of non-
Gaussianity to maximize. The default value is type =
'kurtosis'
nFastICA_pp = nFastICA_pp';

xx3d = 1:1:H;

```

```

yy3d = 1:1:G;
[XI3d,YI3d] = meshgrid(xx3d,yy3d);

for ss = 1:numberoffeatures
    nFastICA_pp_IC(:, :, ss) =
griddata(XI3d(:), YI3d(:), nFastICA_pp(:, ss), XI3d, YI3d, 'nearest'
); nFastICA_pp_IC(:, :, ss) =
imgaussfilt(nFastICA_pp_IC(:, :, ss), sigma1b);
end

plt1 = round((numberoffeatures)^0.5)-1;
plt2 = round((numberoffeatures)^0.5)+1;

fig('Name','IC
Features','units','inches','width',8,'height',3,'font','Helvet
ica','fontsize',12)
for sss = 1:numberoffeatures
    subplot(plt1,plt2,sss),
imshow(histeq(nFastICA_pp_IC(:, :, sss)))
    title(['IC ', num2str(sss), ''])
end

saveas(gcf, ['IC_Features' num2str(Parameter) '.jpg'])

pause(5);

%% 4. Spectral Feature Extraction
%-----
for kkk = 1:numberoffeatures
    Feature = nFastICA_pp_IC(:, :, kkk);
    % cwtmor =
cwtft2(Feature, 'wavelet', 'mexh', 'scales', Scales, 'angles', Angle
s, 'plot', 'norm', 'L1');
    cwtmor =
cwtft2(Feature, 'wavelet', 'mexh', 'scales', Scales, 'angles', Angle
s, 'norm', 'L1');
    cwtout = cwtmor.cfs; %X-Y-1-Scales-Angles
    cwtout_abs = abs(cwtout);
    %WLFs = zeros(G*H, Scale*Angle);
    for jj = 1:Scale
        for jjj = 1 : Angle
            WL = cwtout_abs(:, :, :, jj, jjj);
            WLFs(:, (jj-1)*Angle+jjj) = cat(3, WL(:));
        end
    end
end
end

```

```

    % WLFs_(:, :, kkk) = WLFs;
    Fe(:, :, kkk) = WLFs;
end

for fss = 1:numberoffeatures
    Fs(:, ((fss-1)*(Scale*Angle)+1):fss*(Scale*Angle)) =
Fe(:, :, fss);          % (fss-1)*(Scale*Angle)+fss)
end
for rr = 1:Angle*Scale*numberoffeatures
    Fs_(:, :, rr) =
griddata(XI3d(:), YI3d(:), Fs(:, rr), XI3d, YI3d, 'nearest');
Fs_(:, :, rr) = imgaussfilt(Fs_(:, :, rr), sigma2);
end

features_plot = numberoffeatures*Angle*Scale; %
plt3 = round((features_plot)^0.5)+1;
plt4 = round((features_plot)^0.5);

fig('Name', 'Wavelet
Features', 'units', 'inches', 'width', 8, 'height', 8, 'font', 'Helvet
ica', 'fontsize', 9)

for ssss = 1:features_plot
    subplot_tight(plt3, plt4, ssss, 0),
surf(XI3d, YI3d, Fs_(:, :, ssss))
    colormap jet;
    axis off;
    shading interp
    view(0, 90)
end

saveas(gcf, ['Wavelet_Features' num2str(Parameter) '.jpg'])

pause(0.1);

[nFastICA, WICA, TICA, muICA] =
fastICAWL(Fs', r2, 'negentropy'); %{'kurtosis', 'negentropy'}
specifies which flavor of non-Gaussianity to maximize. The
default value is type = 'kurtosis'
nFastICA_F = nFastICA';
nFastICA_Fs = nFastICA_F;

for rr = 1:r2
    nFastICA_Fs_IC(:, :, rr) =
griddata(XI3d(:), YI3d(:), nFastICA_Fs(:, rr), XI3d, YI3d, 'nearest')

```

```

); nFastICA_Fs_IC(:, :, rr) =
imgaussfilt(nFastICA_Fs_IC(:, :, rr), sigma3);
end

plt3 = round((r2)^0.5)+1;
plt4 = round((r2)^0.5);

fig('Name', 'Wavelet-ICA
Features', 'units', 'inches', 'width', 8, 'height', 8, 'font', 'Helvetica', 'fontsize', 12)
for ssss = 1:r2
    subplot_tight(plt3, plt4, ssss, 0),
surf(XI3d, YI3d, nFastICA_Fs_IC(:, :, ssss))
    colormap jet;
    axis off;
    shading interp
    view(0, 90)
end
saveas(gcf, ['Wavelet_ICA_Features' num2str(Parameter) '.jpg'])

nFastICA_Fs_nd = cat(3, nFastICA_pp_IC, nFastICA_Fs_IC); %
Initial ICs + CWT-ICs
NumbFeat = size(nFastICA_Fs_nd); NumbFeat = NumbFeat(1, 3);

pause(0.5);

%% 5. Traditional ANN prediction: MLP Training
%-----
Xtraversx1 = nFastICA_Fs_nd(round(q1*G), :, :); Xtraversx1 =
permute(Xtraversx1, [2 3 1]);
Xtraversx2 = nFastICA_Fs_nd(round(q2*G), :, :); Xtraversx2 =
permute(Xtraversx2, [2 3 1]);
Xtraversy1 = nFastICA_Fs_nd(:, round(v1*H), :); Xtraversy1 =
permute(Xtraversy1, [1 3 2]);
Xtraversy2 = nFastICA_Fs_nd(:, round(v2*H), :); Xtraversy2 =
permute(Xtraversy2, [1 3 2]);
Ytraversx1 = Image_targ(round(q1*G), :); Ytraversx1 =
permute(Ytraversx1, [2 1]);
Ytraversx2 = Image_targ(round(q2*G), :); Ytraversx2 =
permute(Ytraversx2, [2 1]);
Ytraversy1 = Image_targ(:, round(v1*H));
Ytraversy2 = Image_targ(:, round(v2*H));

```

```

X = cat(1,Xtraversx1,Xtraversx2,Xtraversy1,Xtraversy2); % NN
Inputs
Y = cat(1,Ytraversx1,Ytraversx2,Ytraversy1,Ytraversy2); % NN
Targets

X2 = cat(2,nFastICA_pp,nFastICA_Fs); % NN Estimation data:
Initial ICs + CWT-ICs

DataNum = size(X,1);
InputNum = size(X,2);
OutputNum = size(Y,2);

% Normalization

MinX = min(X);
MaxX = max(X);

MinY = min(Y);
MaxY = max(Y);

XN = X;
YN = Y;

for ii = 1:InputNum
    XN(:,ii) = Normalize_Fcn(X(:,ii),MinX(ii),MaxX(ii));
end

for ii = 1:OutputNum
    YN(:,ii) = Normalize_Fcn(Y(:,ii),MinY(ii),MaxY(ii));
end

% Test and Train Data

TrNum = round(DataNum * TrPercent / 100);
TsNum = DataNum - TrNum;

R = randperm(DataNum);
trIndex = R(1 : TrNum);
tsIndex = R(1+TrNum : end);

Xtr = XN(trIndex,:);
Ytr = YN(trIndex,:);

Xts = XN(tsIndex,:);
Yts = YN(tsIndex,:);

```

```

% Network Structure

pr = [-1 1];
PR = repmat(pr,InputNum,1);
Network = newff(PR,[Neurons OutputNum],{'tansig'
'tansig'},'trainlm');

net.performFcn = 'mse';
Network.plotFcns =
{'plotperform','ploterrhist','plotregression','plotfit','plott
rainstate'};
Network.trainParam.epochs = NN_Iteration;
Network.trainParam.showWindow=true;
Network.trainParam.showCommandLine=true;
Network.trainParam.show=1;
Network.trainParam.goal=1e-8;
Network.trainParam.max_fail=20;
Network.trainParam.mu=1e-3;

% Training
Network = train(Network,Xtr',Ytr');

% Assesment

YtrNet = sim(Network,Xtr')'; % Train Output of Net
YtsNet = sim(Network,Xts')'; % Test Output of Net

RMSEtr = sqrt(mse(YtrNet - Ytr)) % Train Error
RMSEts = sqrt(mse(YtsNet - Yts)) % Test Error
CCtr = corrcoef(YtrNet,Ytr)
CCts = corrcoef(YtsNet,Yts)

% Display Performance Info

fig('Name','ANN: Training and Testing Cross
Plots','units','inches','width',4,'height',8,'font','Helvetica
','fontsize',12)
subplot(2,1,1)
plot(Ytr,YtrNet,'ok')
title(['ANN Training: CC = ',num2str(100*CCtr(1,2)),'%'])
xlabel('Training Target')
ylabel('Training Prediction')

```

```

subplot(2,1,2)
plot(Yts,YtsNet,'ok')
title(['ANN Testing: CC = ',num2str(100*CCts(1,2)),'%'])
xlabel('Testing Target')
ylabel('Testing Prediction')
saveas(gcf,['ANN_Performance' num2str(Parameter) '.jpg'])

% Estimation

DataNum2 = size(X2,1);
InputNum2 = size(X2,2);

% Normalization2

MinX2 = min(X2);
MaxX2 = max(X2);

XN2 = X2;

for ii = 1:InputNum2
    XN2(:,ii) = Normalize_Fcn2(X2(:,ii),MinX2(ii),MaxX2(ii));
end

YestNet = sim(Network,XN2)'; % Estimation Output of Net
(Normalized)

% MLP ANN Predictions

PredictNN =
griddata(XI3d(:),YI3d(:),YestNet(:,1),XI3d,YI3d,'nearest');
PredPredictNNict1 = imgaussfilt(PredictNN,sigma4);
CCEval_Before = corrcoef(PredictNN(:),Image_targ(:));

fig('Name','Final Predicted Target with
ANN','units','inches','width',2,'height',2,'font','Helvetica',
'fontsize',12)
Predict_resizedNN = imresize(PredictNN,2);
Predict_resizedNN1 = imresize(PredictNN,12);
imshow(histeq(Predict_resizedNN1))
title(['ANN Prediction: Nf = ' num2str(NumbFeat) ''])
saveas(gcf,['Predicted_ANN' num2str(Parameter) '.jpg'])

%% 6. SFSS: Multi-Objective Feature Selection Optimization
through Genetic Algorithm

```



```

x = XN';
t = YN';
data.x=x;
data.t=t;

data.nx=size(x,1);
data.nt=size(t,1);
data.nSample=size(x,2);

CostFunction=@(s) FeatureSelectionCost(s,data);% Cost Function

nVar=data.nx;          % Number of Decision Variables

VarSize=[1 nVar];    % Size of Decision Variables Matrix

% Number of Objective Functions
nObj=numel(CostFunction(randi([0 1],VarSize))));

% Initialization

empty_individual.Position=[];
empty_individual.Cost=[];
empty_individual.Out=[];
empty_individual.Rank=[];
empty_individual.DominationSet=[];
empty_individual.DominatedCount=[];
empty_individual.CrowdingDistance=[];

pop= repmat(empty_individual,nPop,1);

for i=1:nPop

    if i~=1
        pop(i).Position=randi([0 1],VarSize);
    else
        pop(i).Position=ones(VarSize);
    end

    [pop(i).Cost, pop(i).Out]=CostFunction(pop(i).Position);

end

% Non-Dominated Sorting
[pop, F]=NonDominatedSorting(pop);

```

```

% Calculate Crowding Distance
pop=CalcCrowdingDistance(pop,F);

% Sort Population
[pop, F]=SortPopulation(pop);

% NSGA Main Loop

for it=1:MaxIt

    % Crossover
    popc= repmat(empty_individual,nCrossover/2,2);
    for k=1:nCrossover/2

        i1=randi([1 nPop]);
        p1=pop(i1);

        i2=randi([1 nPop]);
        p2=pop(i2);

        [popc(k,1).Position,
popc(k,2).Position]=Crossover(p1.Position,p2.Position);

        [popc(k,1).Cost,
popc(k,1).Out]=CostFunction(popc(k,1).Position);
        [popc(k,2).Cost,
popc(k,2).Out]=CostFunction(popc(k,2).Position);

    end
    popc=popc(:);

    % Mutation
    popm= repmat(empty_individual,nMutation,1);
    for k=1:nMutation

        i=randi([1 nPop]);
        p=pop(i);

        popm(k).Position=Mutate(p.Position,mu);

        [popm(k).Cost,
popm(k).Out]=CostFunction(popm(k).Position);

```

```

end

% Merge
pop=[pop
      popc
      popm]; %#ok

% Non-Dominated Sorting
[pop, F]=NonDominatedSorting(pop);

% Calculate Crowding Distance
pop=CalcCrowdingDistance(pop,F);

% Sort Population
[pop, F]=SortPopulation(pop); %#ok

% Truncate
pop=pop(1:nPop);

% Non-Dominated Sorting
[pop, F]=NonDominatedSorting(pop);

% Calculate Crowding Distance
pop=CalcCrowdingDistance(pop,F);

% Sort Population
[pop, F]=SortPopulation(pop);

% Store F1
F1=pop(F{1});
F1=GetUniqueMembers(F1);

% Show Iteration Information
disp(['Iteration ' num2str(it) ': Number of F1 Members = '
num2str(numel(F1))]);

% Plot F1 Costs
fig('Name','Feature Selection
Information','units','inches','width',6,'height',6,'font','Hel
vetica','fontsize',11)
PlotCosts(F1);
title('Last Generation Selected Features versus Errors')
saveas(gcf,['Last_Generation_Error_vs_Nf'
num2str(Parameter) '.jpg'])

```

```

    pause(0.1);

    Qq = size(F1); Qq = Qq(:,1);
    for dddd = 1:Qq
        Res(ddd,1) = dddd;
        Res(ddd,2) = F1(ddd).Out.nf;
        Res(ddd,3) = it;
        Res(ddd,4) = F1(ddd).Out.E;
        Res(ddd,5:5 + max(size(F1(ddd).Out.S))-1) =
F1(ddd).Out.S;
    end
    Res1 = Res;
    clear Res
    ResSize = size(Res1); ResSizeb = ResSize(1,2);
    ResSize1 = ResSize(1,1);
    ResSize2(it,1) = ResSize1;
    Res2(1 + sum(ResSize2(1:it-
1)):sum(ResSize2(1:it)),1:ResSizeb) = Res1;

end

% Results of the Feature Selection
Num_states = size(F1); Num_states = Num_states(:,1);

for hhhh = 1: Num_states
    COsts_(:,hhhh) = F1(hhhh).Cost;
end

A = 1:1:Num_states;
B = COsts_(1,:);
C = COsts_(2,:);

[~,Csort] = sort(C); %Get the order of B
D = A(Csort);

The_Best1 = D(1);
Selected_Fs1 = F1(The_Best1).Out.S;
Num_Selected_Fs1 = size(Selected_Fs1); Num_Selected_Fs1 =
Num_Selected_Fs1(1,2)

pause(0.5);

Selected_Features = Selected_Fs1
csvwrite(['Selected_Features' num2str(Parameter)
'.csv'],Selected_Features);

```

```

Num_Sel = size(Selected_Fs1); Num_Sel = Num_Sel(2);

plt3 = round((Num_Sel)^0.5)+1;
plt4 = round((Num_Sel)^0.5);
fig('Name','Selected
Features','units','inches','width',10,'height',8,'font','Helve
tica','fontsize',10)
for ssss = 1:Num_Sel
    subplot_tight(plt3,plt4,ssss,0),
surf(XI3d,YI3d,nFastICA_Fs_nd(:, :, ssss))
    colormap jet;
    axis off;
    shading interp
    view(0,90)
end

saveas(gcf,['Selected_Feature_Subsets' num2str(Parameter)
'.jpg'])

% Post-Feature Selection Spectral Learning results

XN1_1 = XN(:,Selected_Fs1);      % Initial ICs, Wavelet-ICs.
YN1_1 = YN(:,end);              % Target
XN2_1 = XN2(:,Selected_Fs1);    % Initial ICs, Wavelet-ICs.

Predict1 = sim(F1(The_Best1).Out.net,XN2_1'); % Predicted
Target for Feature Selection 1

CCTR_After_FSS1 =
corrcoef(F1(The_Best1).Out.TrainData.t,F1(The_Best1).Out.Train
Data.y);
CCTS_After_FSS1 =
corrcoef(F1(The_Best1).Out.TestData.t,F1(The_Best1).Out.TestDa
ta.y);

Predict1 =
griddata(XI3d(:),YI3d(:),Predict1',XI3d,YI3d,'nearest');
Predict1 = imgaussfilt(Predict1,sigma4);

CCEval_After_FSS1 = corrcoef(Predict1(:),Image_targ(:));

```

```

pause(0.5);

fig('Name','Predicted Targets with ANN and
FSS','units','inches','width',8,'height',4,'font','Helvetica',
'fontsize',12)
subplot(1,2,1)
imshow(histeq(Predict_resizedNN))
title(['ANN Prediction: Nf = ' num2str(NumbFeat) ''])
xlabel(['R-squared = ' num2str(CCEval_Before(1,2)^2) ''])

subplot(1,2,2)
Predict1_resized = imresize(Predict1,2);
imshow(histeq(Predict1_resized))
title(['FSS Prediction: Nf = ' num2str(Num_Sel) ''])
xlabel(['R-squared = ' num2str(CCEval_After_FSS1(1,2)^2) ''])

saveas(gcf,['Pridicted_ANN_FSS' num2str(Parameter) '.jpg'])

pause(0.5);

% Display Performance Info

fig('Name','FSS: Training and Testing Cross
Plots','units','inches','width',4,'height',8,'font','Helvetica',
'fontsize',10)
subplot(2,1,1)
plot(F1(The_Best1).Out.TrainData.t,F1(The_Best1).Out.TrainData
.y,'ok')
title(['FSS Training: CC =
',num2str(100*CCtr_After_FSS1(1,2)), ' %'])
xlabel('Training Target')
ylabel('Training Prediction')
subplot(2,1,2)
plot(Yts,YtsNet,'ok')
plot(F1(The_Best1).Out.TestData.t,F1(The_Best1).Out.TestData.y
,'ok')
title(['FSS Testing: CC =
',num2str(100*CCts_After_FSS1(1,2)), ' %'])
xlabel('Testing Target')
ylabel('Testing Prediction')
saveas(gcf,['Performance' num2str(Parameter) '.jpg'])

pause(0.5);

```

```

% Evaluation

fig('Name','Evaluation: ANN &
FSS','units','inches','width',4,'height',8,'font','Helvetica',
'fontsize',11)
subplot(2,1,1)
plot((PredictNN(:)),(Image_targ(:)),'ok')
title('Conventional ANN')
title(['Conventional ANN: CC =
',num2str(100*CCEval_Before(1,2)),' %'])
xlabel('Prediction') % x-axis label
ylabel('Target') % y-axis label
subplot(2,1,2)
plot((Predict1(:)),(Image_targ(:)),'ok')
title(['Spectral Learning: CC =
',num2str(100*CCEval_After_FSS1(1,2)),' %'])
xlabel('Prediction') % x-axis label
ylabel('Target') % y-axis label
saveas(gcf,['Evaluation' num2str(Parameter) '.jpg'])

pause(0.5);

% Error Landscape

xx_it = Res2(:,3);
yy_nf = Res2(:,2);
Error_ = Res2(:,4);

xx_it_ = min(xx_it):0.1:max(xx_it);
yy_nf_ = min(yy_nf):0.1:max(yy_nf);

[XXI, YYI] = meshgrid(xx_it_,yy_nf_);
Error = griddata(xx_it,yy_nf,Error_,XXI,YYI,'nearest'); Error
= imgaussfilt(Error,3);

fig('Name','Error','units','inches','width',4,'height',4,'font
','Helvetica','fontsize',12)
surf(XXI,YYI,Error)
title('Spectral Learning')
title('Spectral Learning ')
xlabel('Generation','LineWidth',6) % x-axis label
ylabel('Number of Features','LineWidth',6) % y-axis label
shading interp
axis equal, view(0,90)

```

```

axis square
colorbar
title(colorbar, 'Error')
saveas(gcf,['Error' num2str(Parameter) '.jpg'])

Param = [resize, numberoffeatures, sigma1, sigma2, sigma3,
Scale, Angle, Scale_Expand, TrPercent, Neurons, NN_Iteration,
MaxIt, nPop, mu, q1, q2, v1, v2, Num_Sel]';
csvwrite(['Parameters' num2str(Parameter) '.csv'],Param);

ANN_RSQ_Train = CCtr; ANN_RSQ_Train = ANN_RSQ_Train(1,2)^2
ANN_RSQ_Test  = CCTs; ANN_RSQ_Test = ANN_RSQ_Test(1,2)^2
ANN_RSQ_Eval  = CCEval_Before; ANN_RSQ_Eval =
ANN_RSQ_Eval(1,2)^2

FSS_RSQ_Train = CCtr_After_FSS1; FSS_RSQ_Train =
FSS_RSQ_Train(1,2)^2
FSS_RSQ_Test  = CCTs_After_FSS1; FSS_RSQ_Test =
FSS_RSQ_Test(1,2)^2
FSS_RSQ_Eval  = CCEval_After_FSS1; FSS_RSQ_Eval =
FSS_RSQ_Eval(1,2)^2

Perff =
[ANN_RSQ_Train,ANN_RSQ_Test,ANN_RSQ_Eval,FSS_RSQ_Train,FSS_RSQ
_Test,FSS_RSQ_Eval];

```



## A.2 Functions

Here is an additional list of MATLAB functions that are necessary to run the main MATLAB code:

- **CalcCrowdingDistance.m**

```
function pop=CalcCrowdingDistance(pop,F)

    nF=numel(F);
    for k=1:nF
        Costs=[pop(F{k}).Cost];
        nObj=size(Costs,1);
        n=numel(F{k});
        d=zeros(n,nObj);
        for j=1:nObj
            [cj so]=sort(Costs(j,:));
            d(so(1),j)=inf;
            for i=2:n-1
                d(so(i),j)=abs(cj(i+1)-cj(i-1))/abs(cj(1)-
cj(end));
            end
            d(so(end),j)=inf;
        end

        for i=1:n
            pop(F{k}(i)).CrowdingDistance=sum(d(i,:));
        end
    end
end

% Reference: lectures from matlabsite.com
```

- **centerRows.m**

```
function [Zc, mu] = centerRows(Z)
%
% Syntax:      [Zc, mu] = centerRows(Z);
% Inputs:     Z is an (d x n) matrix containing n samples of
a
%             d-dimensional random vector
% Outputs:    Zc is the centered version of Z
%             mu is the (d x 1) sample mean of Z
```

```

% Description: Returns the centered (zero mean) version of
the input data
% Note:      Z = Zc + repmat(mu,1,n)
% Author:    Brian Moore
%           brimoor@umich.edu
% Date:      November 1, 2016
% Compute sample mean
mu = mean(Z,2);
% Subtract mean
Zc = bsxfun(@minus,Z,mu);

```

- **CreateAndTrainANN.m**

```

function results=CreateAndTrainANN(x,t)

    if ~isempty(x)
        % Choose a Training Function
        % For a list of all training functions type: help
ntrain
        % 'trainlm' is usually fastest.
        % 'trainbr' takes longer but may be better for
challenging problems.
        % 'trainscg' uses less memory. NFTOOL falls back to
this in low memory situations.
        trainFcn = 'trainlm'; % Levenberg-Marquardt

        % Create a Fitting Network
        hiddenLayerSize = 20;
        net = fitnet(hiddenLayerSize,trainFcn);

        % Choose Input and Output Pre/Post-Processing
Functions
        % For a list of all processing functions type: help
nprocess
        net.input.processFcns =
{'removeconstantrows','mapminmax'};
        net.output.processFcns =
{'removeconstantrows','mapminmax'};

        % Setup Division of Data for Training, Validation,
Testing
        % For a list of all data division functions type: help
nndivide
        net.divideFcn = 'dividerand'; % Divide data randomly

```

```

net.divideMode = 'sample'; % Divide up every sample
net.divideParam.trainRatio = 70/100;
net.divideParam.valRatio = 15/100;
net.divideParam.testRatio = 15/100;

% Choose a Performance Function
% For a list of all performance functions type: help
nnperformance
net.performFcn = 'mse'; % Mean squared error

% Choose Plot Functions
% For a list of all plot functions type: help nnplot
net.plotFcns = {};
% net.plotFcns =
{'plotperform','plottrainstate','ploterrhist',
'plotregression','plotfit'};

net.trainParam.showWindow=false;

% Train the Network
[net,tr] = train(net,x,t);

% Test the Network
y = net(x);
e = gsubtract(t,y);
E = perform(net,t,y);

else

y=inf(size(t));
e=inf(size(t));
E=inf;

tr.trainInd=[];
tr.valInd=[];
tr.testInd=[];

end

% All Data
Data.x=x;
Data.t=t;
Data.y=y;
Data.e=e;
Data.E=E;

```

```

% Train Data
TrainData.x=x(:,tr.trainInd);
TrainData.t=t(:,tr.trainInd);
TrainData.y=y(:,tr.trainInd);
TrainData.e=e(:,tr.trainInd);
if ~isempty(x)
    TrainData.E=perform(net,TrainData.t,TrainData.y);
else
    TrainData.E=inf;
end

% Validation and Test Data
TestData.x=x(:,[tr.testInd tr.valInd]);
TestData.t=t(:,[tr.testInd tr.valInd]);
TestData.y=y(:,[tr.testInd tr.valInd]);
TestData.e=e(:,[tr.testInd tr.valInd]);
if ~isempty(x)
    TestData.E=perform(net,TestData.t,TestData.y);
else
    TestData.E=inf;
end

% Export Results
if ~isempty(x)
    results.net=net;
else
    results.net=[];
end
results.Data=Data;
results.TrainData=TrainData;
% results.ValidationData=ValidationData;
results.TestData=TestData;

end

% Reference: lectures from matlabsite.com

```

- **Crossover.m**

```

function [y1, y2]=Crossover(x1,x2)

pSinglePoint=0.1;
pDoublePoint=0.2;

```

```

pUniform=1-pSinglePoint-pDoublePoint;

METHOD=RouletteWheelSelection([pSinglePoint pDoublePoint
pUniform]);

switch METHOD
    case 1
        [y1, y2]=SinglePointCrossover(x1,x2);

    case 2
        [y1, y2]=DoublePointCrossover(x1,x2);

    case 3
        [y1, y2]=UniformCrossover(x1,x2);
end
end

```

% Reference: lectures from matlabsite.com

- **cwftf2.m**

% This is a default MATLAB function for 2D continuous wavelet transform.

- **Dominates.m**

```

function b=Dominates(x,y)

    if isstruct(x)
        x=x.Cost;
    end

    if isstruct(y)
        y=y.Cost;
    end

    b=all(x<=y) && any(x<y);

end

```

% Reference: lectures from matlabsite.com

- **DoublePointCrossover.m**

```

function [y1, y2]=DoublePointCrossover(x1,x2)

    nVar=numel(x1);

    cc=randsample(nVar-1,2);
    c1=min(cc);
    c2=max(cc);

    y1=[x1(1:c1) x2(c1+1:c2) x1(c2+1:end)];
    y2=[x2(1:c1) x1(c1+1:c2) x2(c2+1:end)];

end

% Reference: lectures from matlabsite.com

- fastICA.m

function [Zica, W, T, mu] = fastICA(Z,r,type,flag)

%
% Syntax:      Zica = fastICA(Z,r);
%              Zica = fastICA(Z,r,type);
%              Zica = fastICA(Z,r,type,flag);
%              [Zica, W, T, mu] = fastICA(Z,r);
%              [Zica, W, T, mu] = fastICA(Z,r,type);
%              [Zica, W, T, mu] = fastICA(Z,r,type,flag);
%
% Inputs:      Z is an d x n matrix containing n samples of
d-dimensional
%              data
%              r is the number of independent components to
compute
%              [OPTIONAL] type = {'kurtosis','negentropy'}
specifies
%              which flavor of non-Gaussianity to maximize.
The default
%              value is type = 'kurtosis'
%              [OPTIONAL] flag determines what status updates
to print
%              to the command window. The choices are
%              flag = 0: no printing
%              flag = 1: print iteration status
% Outputs:     Zica is an r x n matrix containing the r
independent

```

```

%           components - scaled to variance 1 - of the
input samples
%           W and T are the ICA transformation matrices
such that
%            $Z_r = T \setminus W' * Z_{ica} + \text{repmat}(\mu, 1, n);$ 
%           is the r-dimensional ICA approximation of Z
%
%           mu is the d x 1 sample mean of Z
% Description: Performs independent component analysis (ICA)
on the input
%           data using the Fast ICA algorithm
% Reference:   Hyvärinen, Aapo, and Erkki Oja. "Independent
component
%           analysis: algorithms and applications." Neural
networks
%           13.4 (2000): 411-430
% Author:     Brian Moore
%           brimoor@umich.edu
% Date:       April 26, 2015
%           November 12, 2016
%
% Constants

TOL = 1e-12;           % Convergence criteria
MAX_ITERS = 1000;     % Max # iterations

% Parse inputs
if ~exist('flag','var') || isempty(flag)
    % Default display flag
    flag = 1;
end
if ~exist('type','var') || isempty(type)
    % Default type
    type = 'kurtosis';
end

% Set algorithm type
if strncmpi(type,'kurtosis',1)
    % Kurtosis
    USE_KURTOSIS = true;
    algoStr = 'kurtosis';
elseif strncmpi(type,'negentropy',1)
    % Negentropy
    USE_KURTOSIS = false;

```

```

        algoStr = 'negentropy';
    else
        % Unsupported type
        error('Unsupported type ''%s'',type);
    end

    % Center and whiten data
    [Zc, mu] = centerRows(Z);
    [Zcw, T] = whitenRows(Zc);

    % Normalize rows to unit norm
    normRows = @(X) bsxfun(@rdivide,X,sqrt(sum(X.^2,2)));

    % Perform Fast ICA

    if flag
        % Prepare status updates
        fmt = sprintf('%%0%dd',ceil(log10(MAX_ITERS + 1)));
        str = sprintf('Iter %s: max(1 - |<w%s, w%s>|) =
%%.4g\\n',fmt,fmt,fmt);
        fprintf('***** Fast ICA (%s) *****\\n',algoStr);
    end
    W = normRows(rand(r,size(Z,1))); % Random initial weights
    k = 0;
    delta = inf;
    while delta > TOL && k < MAX_ITERS
        k = k + 1;

        % Update weights
        Wlast = W; % Save last weights
        Sk = permute(W * Zcw,[1, 3, 2]);
        if USE_KURTOSIS
            % Kurtosis
            G = 4 * Sk.^3;
            Gp = 12 * Sk.^2;
        else
            % Negentropy
            G = Sk .* exp(-0.5 * Sk.^2);
            Gp = (1 - Sk.^2) .* exp(-0.5 * Sk.^2);
        end
        W = mean(bsxfun(@times,G,permute(Zcw,[3, 1, 2])),3) - ...
            bsxfun(@times,mean(Gp,3),W);
        W = normRows(W);

        % Decorrelate weights

```



```

[U, S, ~] = svd(W, 'econ');
W = U * diag(1 ./ diag(S)) * U' * W;

% Update convergence criteria
delta = max(1 - abs(dot(W, Wlast, 2)));
if flag
    fprintf(str, k, k, k - 1, delta);
end
end
if flag
    fprintf('\n');
end

```

% Independent components

```
Zica = W * Zcw;
```

- **fastICAWL.m**

% Same as the fastICA.m in 1.2.8. In cases where we have large number of spectral features (extensive wavelet decomposition) we can change the convergence criteria (TOL) and the Max # iterations (MAX\_ITERS) to reduce the computational cost.

- **FeatureSelectionCost.m**

```
function [z, out]=FeatureSelectionCost(s, data)
```

```
% Read Data Elements
```

```
nRun = 5; wTrain = 0.8;
```

```
x=data.x;
```

```
t=data.t;
```

```
% Selected Features
```

```
S=find(s~=0);
```

```
% Number of Selected Features
```

```
nf=numel(S);
```

```
% Ratio of Selected Features
```

```
rf=nf/numel(s);
```

```
% Selecting Features
```

```

xs=x(S,:);

% Weights of Train and Test Errors
%   wTrain=0.7;
wTest=1-wTrain;

% Number of Runs
%   nRun=20;
EE=zeros(1,nRun);
for r=1:nRun
    % Create and Train ANN
    results=CreateAndTrainANN(xs,t);

    % Calculate Overall Error
    EE(r) = wTrain*results.TrainData.E +
wTest*results.TestData.E;
end

E=mean(EE);
if isinf(E)
    E=100;
end

% Calculate Final Cost
z=[nf
    E];

% Set Outputs
out.S=S;
out.nf=nf;
out.rf=rf;
out.E=E;
out.z=z;
out.net=results.net;
out.Data=results.Data;
out.TrainData=results.TrainData;
out.TestData=results.TestData;

end

% Reference: lectures from matlabsite.com

```

- **fig.m**

```

% This function is used for graph plots and display in MATLAB
environment:
% Copyright © 2012 Reza Shirvany,
matlab.sciences@neverbox.com
% Source:
http://www.mathworks.com/matlabcentral/fileexchange/30736
% Updated: 05/14/2012
% Version: 1.6.5
% default arguments
width=28;
font='Times New Roman';
fontsize=14;
units='pixels';
bgcolor='w';
sborder='off';
flag='';
Pindex=[];

%%%%%%%%%%%% process optional arguments
optargin = size(varargin,2);
if optargin>0

% check if a handle is passed in
if isscalar(varargin{1}) && isnumeric(varargin{1})
    flag=[flag '1'];
    i=2;
    if ishghandle(varargin{1})==1
        flag=[flag 'i'];
    end
else
    i=1;
end

% get the property values
while (i <= optargin)
    if (strcmpi(varargin{i}, 'border'))
        if (i >= optargin)
            error('Property value required for: %s',
num2str(varargin{i}));
        else
            sborder = varargin{i+1};flag=[flag 'b'];
            i = i + 2;
        end
    elseif (strcmpi(varargin{i}, 'width'))
        if (i >= optargin)

```

```

        error('Property value required for: %s',
num2str(varargin{i}));
    else
        width = varargin{i+1};flag=[flag 'w'];
        i = i + 2;
    end
elseif (strcmpi(varargin{i}, 'height'))
    if (i >= optargin)
        error('Property value required for: %s',
num2str(varargin{i}));
    else
        height = varargin{i+1};flag=[flag 'h'];
        i = i + 2;
    end
elseif (strcmpi(varargin{i}, 'font'))
    if (i >= optargin)
        error('Property value required for: %s',
num2str(varargin{i}));
    else
        font = varargin{i+1};flag=[flag 'f'];
        i = i + 2;
    end
elseif (strcmpi(varargin{i}, 'fontsize'))
    if (i >= optargin)
        error('Property value required for: %s',
num2str(varargin{i}));
    else
        fontsize = varargin{i+1};flag=[flag 's'];
        i = i + 2;
    end
elseif (strcmpi(varargin{i}, 'units'))
    if (i >= optargin)
        error('Property value required for: %s',
num2str(varargin{i}));
    else
        units = varargin{i+1};flag=[flag 'u'];
        i = i + 2;
    end
elseif (strcmpi(varargin{i}, 'color'))
    if (i >= optargin)
        error('Property value required for: %s',
num2str(varargin{i}));
    else
        bgcolor = varargin{i+1};flag=[flag 'c'];
        i = i + 2;
    end

```

```

        end
    else
        %other figure properties
        if (i >= optargin)
            error('A property value is missing.');
```

```

        else
            Pindex = [Pindex i i+1];
            i = i + 2;
        end
    end
end

end

end

% We use try/catch to handle errors
try

% creat a figure with a given (or new) handle
if length(strfind(flag,'1'))==1
    s=varargin{1};
    if ishandle(s)==1
        set(0, 'CurrentFigure', s);
    else
        figure(s);
    end
else
    s=figure;
end

flag=[flag 's'];

% set other figure properties
if ~isempty(Pindex)
    set(s,varargin{Pindex});
end

% set the background color
set(s, 'color',bgcolor);

% set the font and font size
set(s, 'DefaultTextFontSize', fontsize);
set(s, 'DefaultAxesFontSize', fontsize);
set(s, 'DefaultAxesFontName', font);

```

```

set(s, 'DefaultTextFontName', font);

%%%%%%%%%%%% set the figure size
% set the root unit
old_units=get(0,'Units');
set(0,'Units',units);

% get the screen size
scrsz = get(0,'ScreenSize');

% set the root unit to its default value
set(0,'Units',old_units);

% set the figure unit
set(s,'Units',units);

% get the figure's position
pos = get(s, 'Position');
old_pos=pos;
aspectRatio = pos(3)/pos(4);

% set the width and height of the figure
if length(strfind(flag,'w'))==1 &&
length(strfind(flag,'h'))==1
    pos(3)=width;
    pos(4)=height;
elseif isempty(strfind(flag,'h'))
    pos(3)=width;
    pos(4) = width/aspectRatio;
elseif isempty(strfind(flag,'w')) &&
length(strfind(flag,'h'))==1
    pos(4)=height;
    pos(3)=height*aspectRatio;
end

% make sure the figure stays in the middle of the screen
diff=old_pos-pos;

if diff(3)<0
pos(1)=old_pos(1)+diff(3)/2;
    if pos(1)<0
        pos(1)=0;
    end
end
if diff(4)<0

```

```

pos(2)=old_pos(2)+diff(4);
    if pos(2)<0
        pos(2)=0;
    end
end

% warning if the given width (or height) is greater than the
screen size
if pos(3)>scrsz(3)
warning(['Maximum width (screen width) is reached! width='
num2str(scrsz(3)) ' ' units]);
end

if pos(4)>scrsz(4)
warning(['Maximum height (screen height) is reached! height='
num2str(scrsz(4)) ' ' units]);
end

% apply the width, height, and position to the figure
set(s, 'Position', pos);
if strcmpi(sborder, 'off')
    set(s, 'DefaultAxesLooseInset', [0,0,0,0]);
end

% handle errors
catch ME
    if isempty(strfind(flag, 'i')) &&
~isempty(strfind(flag, 's'))
        close(s);
    end
    error(ME.message)
end

s=figure(s);
% return handle if caller requested it.
if (nargout > 0)
    h =s;
end
%
% That's all folks!
%
%flag/liwhfsucsb

```

- GetUniqueMembers.m

```
function UA=GetUniqueMembers(A)
```

```
    u=true(size(A));

    for i=2:numel(A)
        for j=1:i-1
            if IsSame(A(i),A(j))
                u(i)=false;
                break;
            end
        end
    end
end
```

```
    UA=A(u);
```

```
end
```

```
function e=IsSame(a,b)
```

```
    e=all(a.Position==b.Position);
```

```
end
```

```
% Reference: lectures from matlabsite.com
```

```
- hist_eq.m
```

```
% This function is for histogram equalization of images (by author):
```

```
function [k1]=hist_eq(i)
for j=1:3
k=i(:,:,j);
k1(:,:,j)= histeq(k);
end
```

```
- Mutate.m
```

```
function y=Mutate(x,mu)
```

```
    nVar=numel(x);
```

```
    nmu=ceil(mu*nVar);
```



```

j=randsample(nVar,nmu);

y=x;
y(j)=1-x(j);

end

% Reference: lectures from matlabsite.com

- NonDominatedSorting.m

function [pop F]=NonDominatedSorting(pop)

nPop=numel(pop);

for i=1:nPop
    pop(i).DominationSet=[];
    pop(i).DominatedCount=0;
end

F{1}=[];

for i=1:nPop
    for j=i+1:nPop
        p=pop(i);
        q=pop(j);

        if Dominates(p,q)
            p.DominationSet=[p.DominationSet j];
            q.DominatedCount=q.DominatedCount+1;
        end

        if Dominates(q.Cost,p.Cost)
            q.DominationSet=[q.DominationSet i];
            p.DominatedCount=p.DominatedCount+1;
        end

        pop(i)=p;
        pop(j)=q;
    end

    if pop(i).DominatedCount==0
        F{1}=[F{1} i];
        pop(i).Rank=1;
    end
end

```

```

end

k=1;

while true

    Q=[];

    for i=F{k}
        p=pop(i);

        for j=p.DominationSet
            q=pop(j);

            q.DominatedCount=q.DominatedCount-1;

            if q.DominatedCount==0
                Q=[Q j];
                q.Rank=k+1;
            end

            pop(j)=q;
        end
    end

    if isempty(Q)
        break;
    end

    F{k+1}=Q;

    k=k+1;

end

end

% Reference: lectures from matlabsite.com

- Normalize_Fcn.m

function xN = Normalize_Fcn(x,MinX,MaxX)

xN = (x - MinX) / (MaxX - MinX) * 2 - 1;

```

```
end
```

- **Normalize\_Fcn2.m**

```
function xN2 = Normalize_Fcn2(x2,MinX2,MaxX2)
xN2 = (x2 - MinX2) / (MaxX2 - MinX2) * 2 - 1;
end
```

- **PlotCosts.m**

```
function PlotCosts(pop)
    Costs=[pop.Cost];
    plot(Costs(1,:),Costs(2:,:), 'r*', 'MarkerSize',8);
    xlabel('n_f');
    ylabel('E');
    grid on;
```

```
end
```

```
% Reference: lectures from matlabsite.com
```

- **RouletteWheelSelection.m**

```
function i=RouletteWheelSelection(P)
    r=rand;
    c=cumsum(P);
    i=find(r<=c,1,'first');
```

```
end
```

```
% Reference: lectures from matlabsite.com
```

- **SinglePointCrossover.m**

```
function [y1, y2]=SinglePointCrossover(x1,x2)
    nVar=numel(x1);
```

```

    c=randi([1 nVar-1]);

    y1=[x1(1:c) x2(c+1:end)];
    y2=[x2(1:c) x1(c+1:end)];

end

% Reference: lectures from matlabsite.com

- SortPopulation.m

function [pop F]=SortPopulation(pop)

    % Sort Based on Crowding Distance
    [~, CDSO]=sort([pop.CrowdingDistance], 'descend');
    pop=pop(CDSO);

    % Sort Based on Rank
    [~, RSO]=sort([pop.Rank]);
    pop=pop(RSO);

    % Update Fronts
    Ranks=[pop.Rank];
    MaxRank=max(Ranks);
    F=cell(MaxRank,1);
    for r=1:MaxRank
        F{r}=find(Ranks==r);
    end

end

% Reference: lectures from matlabsite.com

- subplot_tight.m

% This function is used to make figures of the features kept
together:

function varargout=subplot_tight(m, n, p, margins, varargin)

%% Default params
isWrapper=false;
if (nargin<4) || isempty(margins)
    margins=[0.04,0.04]; % default margins value- 4% of figure

```

```

end
if length(margins)==1
    margins(2)=margins;
end

%note n and m are switched as Matlab indexing is column-wise,
while subplot indexing is row-wise :(
[subplot_col,subplot_row]=ind2sub([n,m],p);

height=(1-(m+1)*margins(1))/m; % single subplot height
width=(1-(n+1)*margins(2))/n; % single subplot width

% note subplot supports vector p inputs- so a merged subplot of
higher dimensions will be created
subplot_cols=1+max(subplot_col)-min(subplot_col); % number of
column elements in merged subplot
subplot_rows=1+max(subplot_row)-min(subplot_row); % number of
row elements in merged subplot

merged_height=subplot_rows*( height+margins(1) )- margins(1);
% merged subplot height
merged_width= subplot_cols*( width +margins(2) )- margins(2);
% merged subplot width

merged_bottom=(m-max(subplot_row))*(height+margins(1))
+margins(1); % merged subplot bottom position
merged_left=min(subplot_col)*(width+margins(2))-width;
% merged subplot left position
pos=[merged_left, merged_bottom, merged_width, merged_height];

if isWrapper
    h=subplot(m, n, p, varargin{:}, 'Units', 'Normalized',
'Position', pos);
else
    h=axes('Position', pos, varargin{:});
end

if nargout==1
    varargout=h;
end

```

```
function [y1, y2]=UniformCrossover(x1,x2)

    alpha=randi([0 1],size(x1));

    y1=alpha.*x1+(1-alpha).*x2;
    y2=alpha.*x2+(1-alpha).*x1;

end
```

- **whitenRows.m**

```
function [Zw, T] = whitenRows(Z)
% Syntax:      [Zw, T] = whitenRows(Z);
% Inputs:     Z is an (d x n) matrix containing n samples of a
%            d-dimensional random vector
% Outputs:    Zw is the whitened version of Z
%            T is the (d x d) whitening transformation of Z
% Description: Returns the whitened (identity covariance)
version of the
%            input data
% Notes:      (a) Must have n >= d to fully whitenRows Z
%            (b)  $Z = T \setminus Z_{cw}$ 
% Author:     Brian Moore
%            brimoor@umich.edu
% Date:       November 1, 2016
% Compute sample covariance
R = cov(Z');

% Whiten data
[U, S, ~] = svd(R,'econ');
T = U * diag(1 ./ sqrt(diag(S))) * U';
Zw = T * Z;
```

## APPENDIX B

### 2D SPECTRAL FEATURE SELECTION: MATLAB CODE EVALUATION

As an experiment, we simulated and evaluated the SFSS method on 2D feature selection from photos that bear some latent features need to be extracted to rebuild a hidden face of a cat mixed with two human faces. Compared to traditional ANN, our SFSS algorithm was able to learn better from limited pixel samples (similar to prior geological information from borehole samples), and evaluations show that the SFSS can reconstruct a much more visible model of the hidden face of the cat.

The input of the SFSS algorithm consists of three images that contain mixed forms of latent features (two human faces and one cat face in Figure B.1). The problem can be formulated as separation of cat's face from mixed images with limited access to the data from the original cat's face (targets to be predicted). The targets are sampled in two horizontal and vertical directions (red lines in Figure B.1). This 2D imaging system is equivalent to the 3D physical properties with latent geological features and several boreholes with sampled geological targets. This simulation helps us to evaluate the performance of the SFSS before implementation of a more complex 3D version of it. The task is to let the SFSS learn the variations in the target to predict the target values in places with no access to sampled pixels.

A preliminary blind source separation with Fast-ICA could separate the latent features inside the mixed images. The results are shown in Figure B.2, in the form of three negentropy maximized independent components.

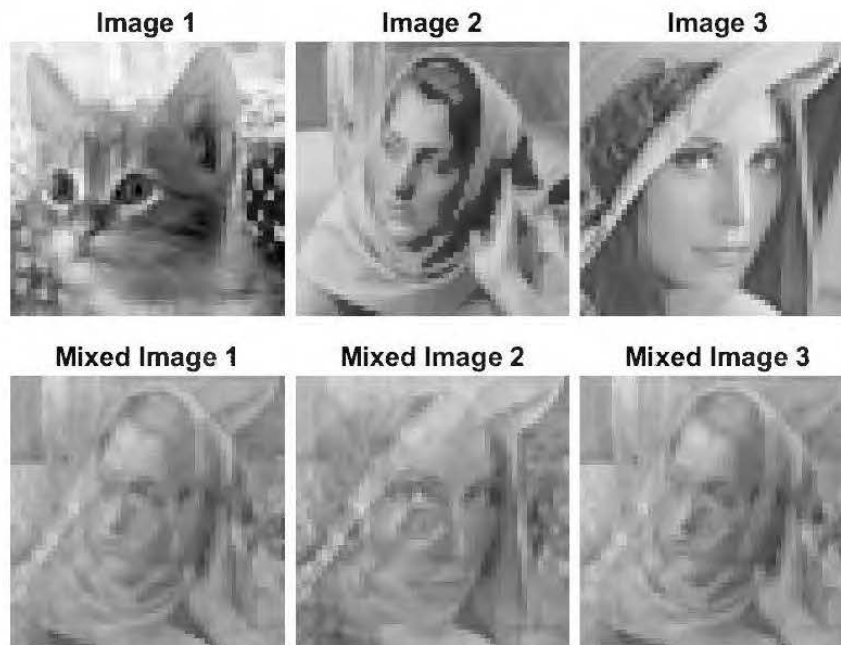


**Figure B.1** Simulation of a 2D imaging system containing several latent features (faces). The red traverse lines are indicating the sampled pixels that form the targets of the SFSS algorithm.

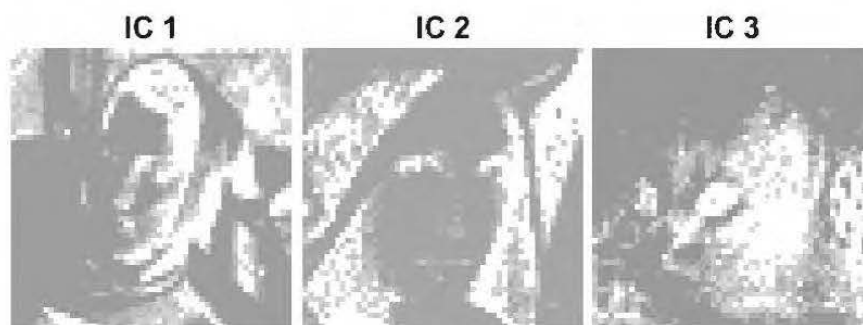


**Figure B.2** Three independent components (ICs) of the mixed image calculated from negentropy maximization of input mixed images.

The next step is to decompose these independent components to form a set of raw spectral features through a continuous wavelet transform. We calculated the 2D wavelet coefficients for 20 scales in four directions ( $0^\circ$ ,  $90^\circ$ ,  $180^\circ$ ,  $270^\circ$ ). However, the



algorithm allows choosing any number of scales and directions as long as the computer hardware allows. The spectral decomposition is iterated for three initial independent components and thus produces 240 raw features containing several frequency-dependent raw features need to be extracted (Figure B.3).

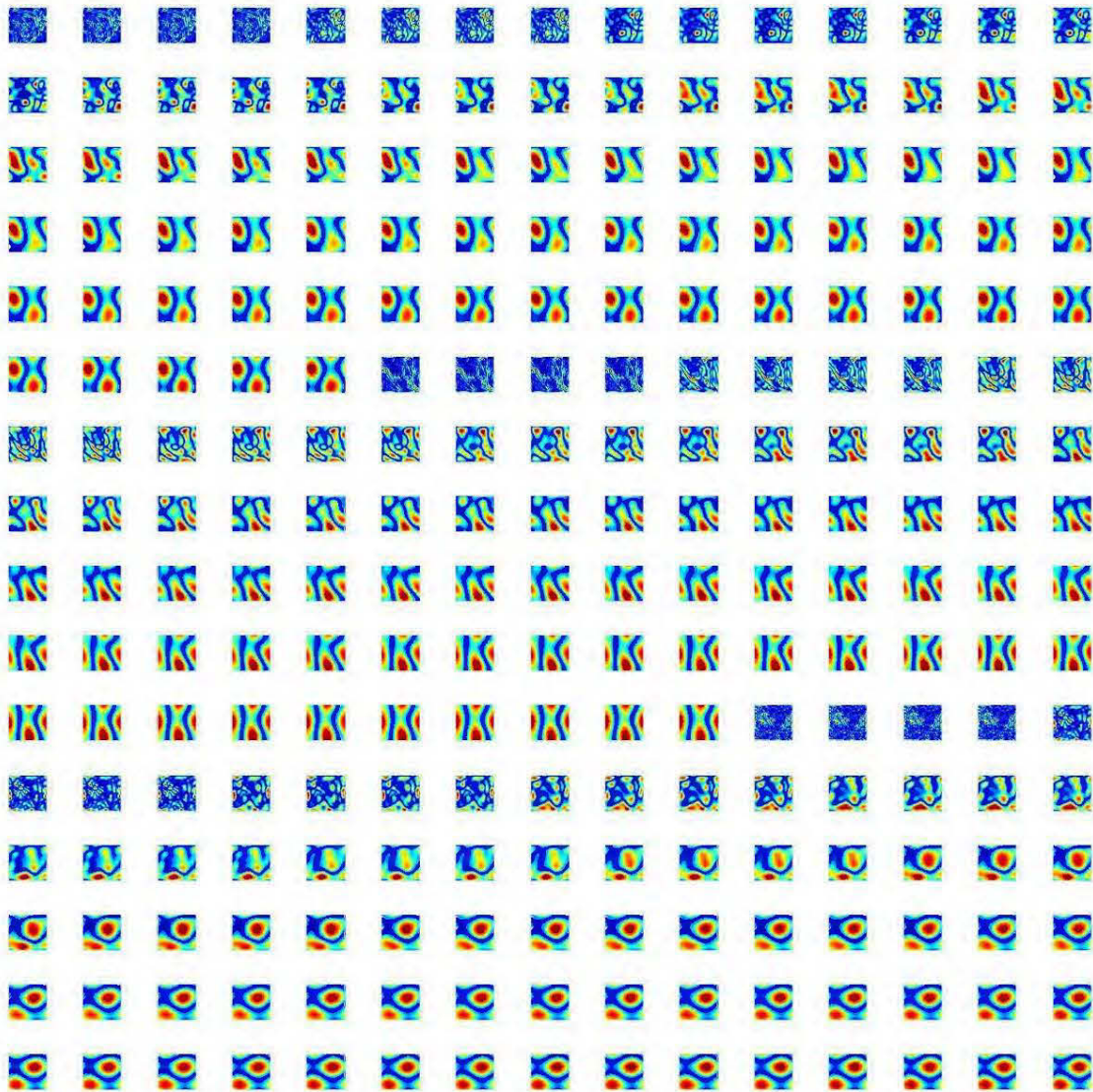


**Figure B.3** 240 raw spectral features produce by CWT with 20 scales in four directions ( $0^\circ$ ,  $90^\circ$ ,  $180^\circ$ ,  $270^\circ$ ).

We used Fast-ICA through negentropy maximization to separate these 240 raw features to produce the spectral inputs necessary for feature selection. The Fast-ICA algorithm here is also able to reduce the dimensionality of the raw features. This is important in cases where we produce a large number of raw features through CWT in a way that our computational hardware resources are not enough for handling the inevitable high dimensionality. Here, we reduce the dimensionality of the raw spectral features and thus produce 120 features to be fed into to SFSS algorithm (Figure B.4).

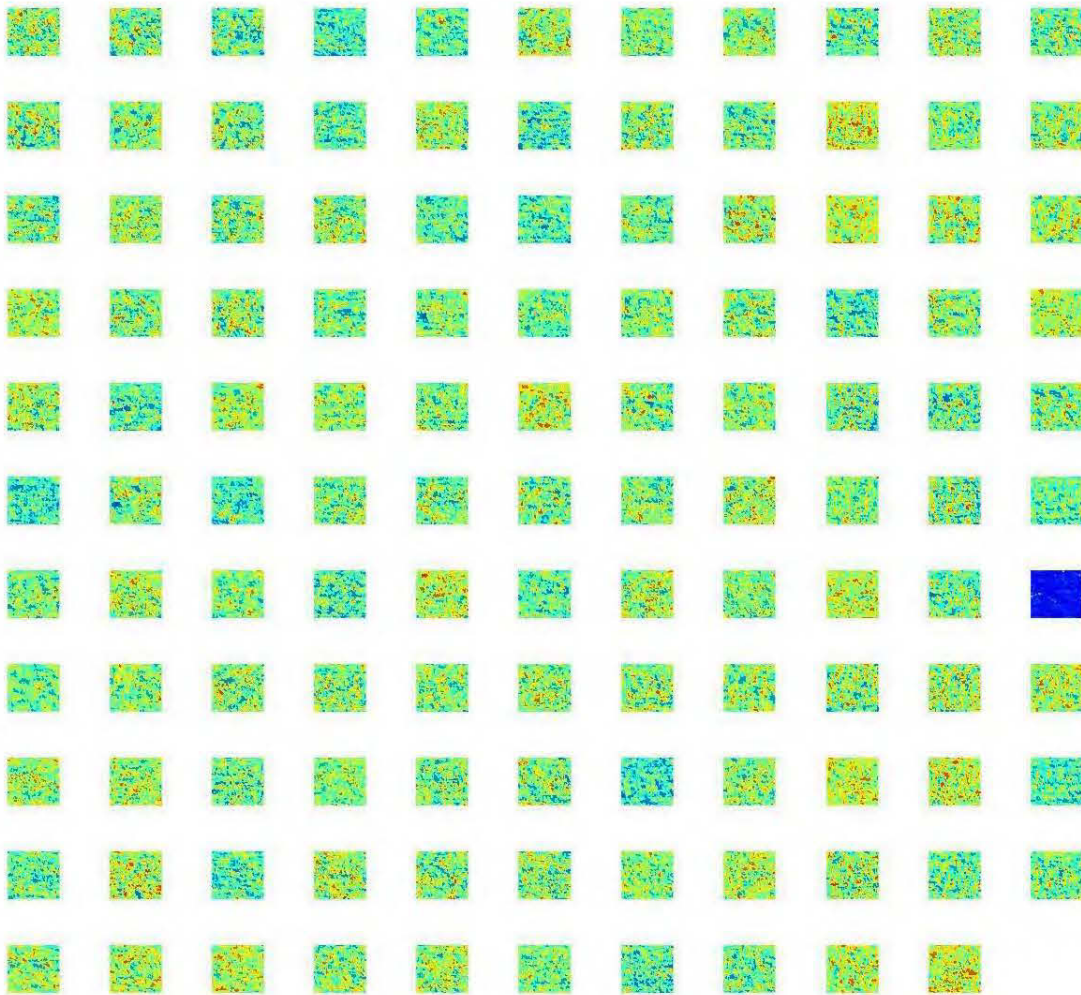


**Figure B.4** 120 separated spectral features after Fast-ICA dimensionality reduction.

For feature selection, we used an MLP network with 120 spectral features inputs, ten neurons in the hidden layer, maximum of ten iterations, and one output. 70% of the targets are used for training, and the rest of it is set to be used for testing and evaluation. The GA is iterated in 5 generation with ten population, 70% crossover, 40% of mutation and mutation rate of 0.1 (parameters in Appendix A).

The overall performance of both conventional ANN optimized with the Levenberg-Marquardt method, as well as the SFSS algorithm optimized with GA are compared in Figure B.5. The SFSS algorithm gives a better testing result with 91% correlation coefficients between the predicted results compared to the target values.

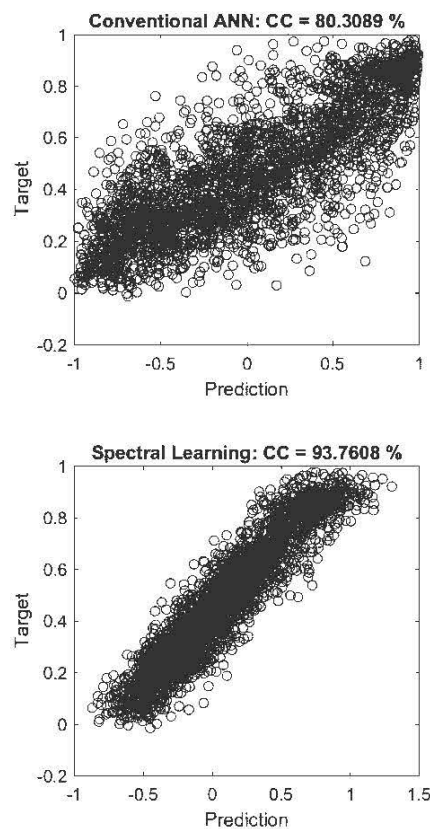


**Figure B.5** Evaluation of ANN and spectral learning algorithms in target prediction.



The error landscape of the SFSS is also shown in Figure B.6. As can be seen, the best results (least global error indicated by blue color) come with the last generations of GA that selects 54 features for spectral learning (Figure B.7). As can be seen, the SFSS is able to recover a more visible face of the cat that was originally mixed with two other faces. The SFSS selected 54 out of 120, which means 66 spectral features were extremely redundant in the reconstruction of the cat's face.

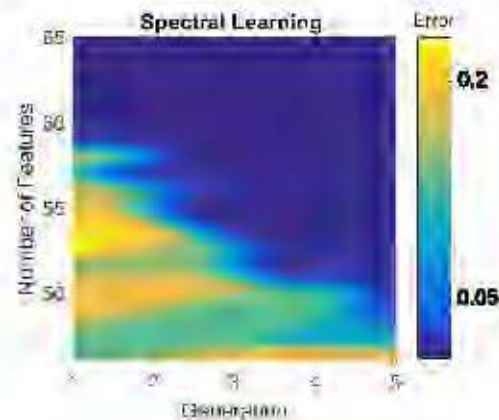


**Figure B.6** The bi-objective error landscape of SFSS algorithm.

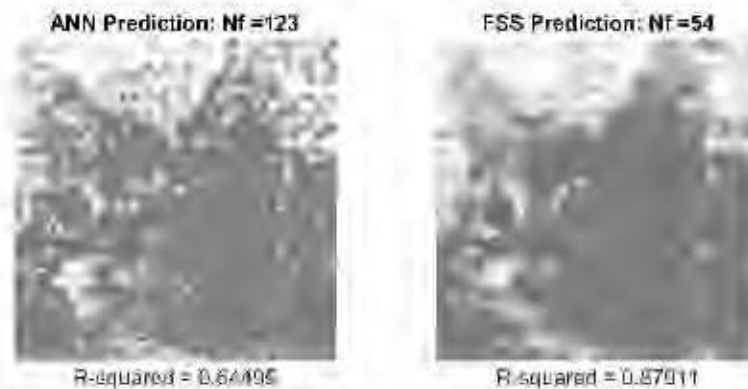


**Figure B.7** Results of 2D ANN predictions (left) versus 2D SFSS predictions (right). SFSS resulted in the better reconstruction of cat's face with less number of spectral features (right).

## GENERAL REFERENCES

- Abbassi, B., L. Z., Cheng, J., Richards, J., Hübert, J., Legault, M., Rebagliati, K., Witherly, 2018a, 3D cooperative inversion of magnetic and DC/IP data over Newton epithermal Au-Ag deposit in British Columbia, Canada: Geophysics (submitted / under review).
- Abbassi, B., L. Z., Cheng, J., Richards, J., Hübert, J., Legault, M., Rebagliati, K., Witherly, 2018b, Geophysical properties of an epithermal Au-Ag deposit in British Columbia: Interpretation, **6**, 4, T907-T918.
- Allis, R.G., 1990, Geophysical anomalies over epithermal systems: Journal of Geochemical Exploration, **36**, 339-374.
- Amato, U., A. Antoniadis, V. Cuomo, L. Cutillo, M. Franzese, L. Murino, and C. Serio, 2008, Statistical cloud detection from SEVIRI multispectral images: Remote Sens. Environ., **112**, 3, 750-766.
- Barnett, C. and P., Williams, 2006, Mineral Exploration Using Modern Data Mining Techniques: First Break, **24**, 7, 295-310.
- Barnie, T., and C. Oppenheimer, 2015, Extracting high-temperature event radiance from satellite images and correcting for saturation using Independent Component Analysis: Remote Sens. Environ., **158**, 56-68.
- Bayliss, J. D., J. A. Gualtieri, and R. F. Crompt, 1998, Analyzing hyperspectral data with independent component analysis, in 26th AIPR Workshop: Exploiting New Image Sources and Sensors, pp. 133-143, International Society for Optics and Photonics.
- Beckmann, C. F., and S. M. Smith, 2004, Probabilistic independent component analysis for functional magnetic resonance imaging: IEEE Trans. Med. Imaging, **23**, 2, 137-152.
- Benitez, J.M., 1997, Are artificial neural networks black boxes? Neural Networks, IEEE Transac, **8**, 5, 1156-1164.
- Bishop, C.M., 1995: Neural Networks for Pattern Recognition, Clarendon Press.

- Bliss, J.D., 1992, Developments in mineral deposit modeling: U.S. Geological Survey Bulletin, 168p.
- Brown, A. R., 1996, Seismic attributes and their classification: *The Leading Edge*, 15, 10.
- Brown, G.D., S. Yamada, T.J. Sejnowski, 2001, Independent component analysis at the neural cocktail party: *Trends in Neurosciences*, 24, 1.
- Castagna, J.P., S., Sun, 2006, Comparison of spectral decomposition methods: *First Break* 24, 3, 75-79.
- Chen, J., and G. M. Hoversten, 2012, Joint inversion of marine seismic AVA and CSEM data using statistical rock - physics models and Markov random fields: *Geophysics*, 77, 1, R65-R80.
- Chen, Q., and S. Sidney, 1997, Seismic attribute technology for reservoir forecasting and monitoring: *The Leading Edge*, 16, 445-456.
- Chen, Q., Y., Chen, W., Jiang, 2016, Genetic particle swarm optimization-based feature selection for very-high-resolution remotely sensed imagery object change detection: *Sensors*, 16, 8, 1204, 1-20.
- Cherry, E.C., 1953, Some experiments on the recognition of speech, with one and with two ears: *J Acoust. Soc. Am.*, 25, 975-979.
- Chopra, S., and D. Pruden, 2003, Multiattribute seismic analysis on AVO-derived parameters: *The Leading Edge*, 22, 998-1002.
- Chopra, S., and K. J. Marfurt, 2008, Emerging and future trends in seismic attributes: *Geophysics*, 27, 298-318.
- Choudrey, R., S. Roberts, 2002, Variational mixture of Bayesian independent component analyzers: *Neural Comput.*, 15, 1, 213-252.
- Claerbout, J.F. and F. Muir, 1973, Robust modeling with erratic data: *Geophysics*, 38, 826-844.
- Clark, D.A., 2014, Magnetic effects of hydrothermal alteration in porphyry copper and iron-oxide copper-gold systems: A review: *Tectonophysics*, 624 & 625, 46-65.

- Clerc, M., 2013, Particle Swarm Optimization: Wiley-ISTE.
- Comon, P., 1994, Independent component analysis: A new concept, *Signal Process.*, 36, 3, 287-314.
- Dentith, M., and S. T. Mudge, 2014, *Geophysics for the Mineral Exploration Geoscientist*: Cambridge University Press.
- Doetsch, J., N. Linde, I. Coscia, S. Greenhalgh, and A. Green, 2010, Zonation for 3D aquifer characterization based on joint inversion of multimethod cross-hole geophysical data: *Geophysics*, 75, 6, G53-G64.
- Dorigo, M., Stützle, T., 2004, *Ant Colony Optimization*: A Bradford Book.
- Ellis, R. G., B. de Wet, I. N. MacLeod, 2012, Inversion of magnetic data for remanent and induced sources: 22th International Geophysical Conference and Exhibition, ASEG, Extended Abstracts, 1-4.
- Encom Technology Pty Ltd, 2009, Noddy structural and geological modeling: Reference manual, TecTask, [http://www.tectonique.net/tectask/index.php?option=com\\_content&view=article&id=23](http://www.tectonique.net/tectask/index.php?option=com_content&view=article&id=23), accessed 23 April 2018.
- Feebreyf, A.F., H. Hishida, K. Yoshioka, and K. Nakayama, 1998, Geophysical Expression of Low Sulphidation Epithermal, Au-Ag Deposits and Exploration Implications - Examples from the Hokusatsu Region of SW Kyushu, Japan: *Resource Geology*, 48, 75-86.
- Fullagar, P. K., N. A. Hughes, and J. Pain, 2000, Drilling constrained 3D gravity inversion: *Exploration Geophysics*, 31, 1/2, 17-23.
- Gallardo, L. A., S. L. Fontes, M. A. Meju, M. P. Buonora, and P. de Lugao, 2012, Robust geophysical integration through structure - coupled joint inversion and multispectral fusion of seismic reflection, magnetotelluric, magnetic and gravity images: Example from Santos Basin, offshore Brazil: *Geophysics*, 77, 5, B237-B251.
- Gen, M., Cheng, R., 1997, *Genetic Algorithms and Engineering Design*: John Wiley & Sons.

- Geosoft Inc, 2012, Sharpening using Iterative Reweighting Inversion: Oasis montaj Best Practice Guide, [http://updates.geosoft.com/downloads/files/how-to-guides/Best-Practice-Guide\\_Sharpening\\_using\\_IRI.pdf](http://updates.geosoft.com/downloads/files/how-to-guides/Best-Practice-Guide_Sharpening_using_IRI.pdf), accessed 27 Feb 2013.
- Geosoft Inc, 2018, VOXI Earth Modelling - Running a Forward Model: Oasis Montaj Best Practice Guide: [http://updates.geosoft.com/downloads/files/how-to-guides/VOXI-How-To\\_Run\\_a\\_Forward\\_Model.pdf](http://updates.geosoft.com/downloads/files/how-to-guides/VOXI-How-To_Run_a_Forward_Model.pdf), accessed 8 Oct 2018.
- Geotech Ltd., 2010, Report on a helicopter-borne Z-axis tipper electromagnetic (ZTEM) and aeromagnetic geophysical survey: Technical Report, Geotech Ltd., Canada, Projects 10005, 10010 and 10016.
- Griffanti, L., G. Salimi-Khorshidi, C.F. Beckmann, E.J. Auerbach, G. Douaud, C.E. Sexton, E. Zsoldos, K.P. Ebmeier, N. Filippini, C.E. Mackay, 2014, ICA-based artifact removal and accelerated fMRI acquisition for improved resting state network imaging: *NeuroImage*, 95, 232-247.
- Haber, E., and D. Oldenburg, 1997, Joint inversion: A structural approach: *Inverse Problems*, 13, 63-77.
- Haber, E., and M. H. Gazit (2013), Model fusion and joint inversion: *Surv. Geophys.*, 34, 675-695.
- Hall, M., 2016, White magic: Calibrating seismic attributes: <http://www.agilegeoscience.com/blog/2016/1/25/white-magic-calibrating-seismicattributes>, accessed 10 October 2017.
- Haupt, R.L., 2004, *Practical Genetic Algorithms*: Wiley-Interscience, 2nd edition.
- Haupt, S. E., 2006, Nonlinear empirical models of dynamical systems: *Computers and Mathematics with Applications*, 51, 431-440.
- Haupt, S.E., Marzban, C., Pasini, A., 2009, *Artificial Intelligence Methods in the Environmental Sciences*: Springer.
- Honório, B. C. Z., A. C., Sanchetta, E. P. Leite, and A. C., Vidal, 2014, Independent component spectral analysis: *Interpretation*, 2, 1, SA21-SA29.
- Huang, C.L., C.J., Wang, 2006, A GA-based feature selection and parameters optimization for support vector machines: *Expert Syst. Appl.* 31, 2, 231-240.



- Hübert, J., B.M. Lee, L. Liu, M. J. Unsworth, J. P. Richards, B. Abbassi, L.Z. Cheng, D.W. Oldenburg, J. M. Legault, and M. Rebagliati, 2015, Three-dimensional imaging of a Ag-Au-rich epithermal system in British Columbia, Canada, using airborne z-axis tipper electromagnetic and ground-based magnetotelluric data: *Geophysics*, 81, B1-B12.
- Hyvärinen, A., 2013, Independent component analysis: Recent advances: *Phil. Trans. R. Soc. A*, 371,
- Hyvärinen, A., and E. Oja, 1997, A fast fixed-point algorithm for ICA, *Neural Comput.*, 9, 1483-1492.
- Hyvärinen, A., and E. Oja, 2000, Independent component analysis: algorithms and applications: *Neural Networks* 13, 411-430.
- Hyvärinen, A., J., Karhunen, E., Oja, 2002, Independent component analysis: Wiley Interscience Publication, Wiley, inc, New York.
- Hyvärinen, A., J.Karhunen, and E. Oja, 2001, Independent component analysis, in S. Haykin, ed., *Adaptive and learning systems for signal processing, communications, and control*: John Wiley & Sons, Inc.
- Irvine, R.J., and M.J. Smith, 1990, Geophysical Exploration for Epithermal Gold Deposits: *Journal of Geochemical Exploration*, 36, 1-3, 375-412
- Jenssen, R., and T. Eltoft, 2003, Independent component analysis for texture segmentation: *Pattern Recognition* 36, 10, 2301-2315.
- Kalnay, E., 2003, *Atmospheric modeling, data assimilation, and predictability*: Cambridge University Press.
- Kumar, P., E., Foufoula-Georgio, 1997, Wavelet analysis for geophysical applications: *Reviews of Geophysics*, 35, 4, 385-412.
- Legault, J.M., J., Niemi, J.S., Brett, S., Zhao, Z., Han, and G.C., Plastow, 2016, Passive Airborne EM and ground IP resistivity results over the Romero intermediate sulfidation epithermal gold deposits, Dominican Republic: *Exploration Geophysics*, 47, 3, 191-200.

- Lelièvre P.G. and D.W. Oldenburg, 2009, A 3D total magnetization inversion applicable when significant, complicated remanence is present: *Geophysics*, 74, L21-L30.
- Lelièvre, P. G., 2009, Integrating geologic and geophysical data through advanced constrained inversions: Ph.D. thesis, Department of Earth and Ocean Sciences, The University of British Columbia, Vancouver, British Columbia, Canada.
- Lelièvre, P. G., and C. G. Farquharson, 2016, Integrated Imaging for Mineral Exploration, in Moorkamp, M., ed., *Integrated Imaging of the Earth: Theory and Applications*, Geophysical Monograph 218, First Edition, Wiley Online Library, 61-95.
- Lelièvre, P. G., D. W. Oldenburg, and N. C. Williams, 2009, Integrating geologic and geophysical data through advanced constrained inversions: *Exploration Geophysics*, 40, 4, 334-341.
- Li, S., C. Liao, and J. T. Kwok, 2006, Wavelet-based feature extraction for microarray data classification, in *Proceedings of the International Joint Conference on Neural Networks*, Vancouver, Canada, 5028-5033.
- Li, Y., and D. W. Oldenburg, 2000, 3D inversion of induced polarization data: *Geophysics*, 65, 1931-1945.
- Li, Y., and D.W. Oldenburg, 1997, 3D inversion of magnetic data: *Geophysics*, 61, 394-408.
- Lindseth, R. O., 2005, Seismic attributes — Some recollections: *Canadian Society of Exploration Geophysicists Recorder*, 30, 3, 16-17.
- Lines, L. R., A. K. Schultz, and S. Treitel, 1988, Cooperative inversion of geophysical data: *Geophysics*, 53, 1, 8-20.
- Liu, B., W. Dai, W. Peng, and X. Meng, 2015, Spatiotemporal analysis of GPS time series in vertical direction using independent component analysis: *Earth Planets Space*, 67, 189, 1-10.
- Liu, H., H. Motoda, 2012, *Feature selection for knowledge discovery and data mining*: Springer Science & Business Media, Boston.

- Liu, L., J. P. Richards, A. DuFrane, and M. Rebagliati, 2015, Geochemistry, geochronology, and fluid inclusion study of the Late Cretaceous Newton epithermal gold deposit, British Columbia: *Canadian Journal of Earth Sciences*, 53, 1, 10-33.
- Liu, Y., 2009, Wavelet feature extraction for high-dimensional microarray data: *Neurocomputing*, 72, 4-6, 985-990.
- Loke, M.H., 2015, Tutorial: 2D and 3D electrical imaging surveys: Geotomo Software, <http://www.geotomosoft.com/downloads.php>, accessed 26 June 2016.
- Loke, M.H., I. Acworth, and T., Dahlin, 2003, A comparison of smooth and blocky inversion methods in 2D electrical imaging surveys: *Exploration Geophysics*, 34, 182-187.
- Mackenzie, D., I. Daubechies, D., Kleppner, S., Mallat, Y., Meyer, M.B., Ruskai, G., Weiss, 2001, Wavelets: Seeing the Forest and the Trees, *Beyond Discovery: National Academy of Sciences*, December 2001, available online at <http://www.beyonddiscovery.org>.
- Marquardt, D., 1963, an Algorithm for Least-Squares Estimation of Nonlinear Parameters: *SIAM Journal on Applied Mathematics*, 11, 2, 431-441.
- Martens, D., De Backer, M., Haesen, R., Vanthienen, J., Snoeck, M., Baesens, B., 2007, Classification with Ant Colony Optimization: *IEEE Transactions on Evolutionary Computation*, 11, 5, 651-665.
- Massey, N.W.D., D.G. MacIntyre, P.J. Desjardins, and R.T. Cooney, 2005, Digital Geology Map of British Columbia: B.C. Ministry of Energy and Mines, Open File 2005-2, DVD.
- Matthews, K. B., 2001, Applying Genetic Algorithms to Multi-Objective Land-Use Planning: Ph.D. Thesis, The Robert Gordon University.
- McClenaghan, L., 2013, Geology and genesis of the Newton bulk-tonnage gold-silver deposit, central British Columbia: M.S. thesis, University of British Columbia.
- McMillan, M.S., and D. W., Oldenburg, 2014, Cooperative constrained inversion of multiple electromagnetic datasets: *Geophysics*, 79, 4, B173-B185.

- McMillan, W., J. Thompson, C. Hart, and S. Johnston, 1995, Regional geological and tectonic setting of porphyry deposits in British Columbia and Yukon Territory: Porphyry deposits of the northwestern Cordillera of North America: Canadian Institute of Mining, Metallurgy and Petroleum.
- Moorkamp, M., P. G., Lelièvre, N., Linde, A., Khan, 2016, Integrated Imaging of the Earth: Theory and Applications: American Geophysical Union and John Wiley and Sons, Inc.
- Moreau, F., D. Gibert, M. Holschneider, and G. Saracco, 1997, Wavelet analysis of potential fields: *Inverse Problems*, 13, 1, 165-178.
- Morrell, A.E., C.A. Locke, J., Cassidy and J., Mauk, 2011, Geophysical characteristics of adularia-sericite epithermal gold-silver deposits in the Waihi-Waitekauri region, New Zealand: *Economic Geology*, 106, 1031-1041.
- Murakami, H., 2008, Variations in Chemical Composition of Clay Minerals and Magnetic Susceptibility of Hydrothermally Altered Rocks in the Hishikari Epithermal Gold Deposit, SW Kyushu, Japan: *Resource Geology*, 58, 1-24.
- Murakami, H., 2008, Variations in Chemical Composition of Clay Minerals and Magnetic Susceptibility of Hydrothermally Altered Rocks in the Hishikari Epithermal Gold Deposit, SW Kyushu, Japan: *Resource Geology*, 58, 1, 1-24.
- Murtaugh, F., J.L., Starck, M.W., Berry, 2000, Overcoming the curse of dimensionality in clustering by means of the wavelet transform: *Computer Journal*, 43, 2, 107-120.
- Naseer, M.T., S., Asim, 2017, Detection of cretaceous incised-valley shale for resource play, Miano gas field, SW Pakistan: Spectral decomposition using continuous wavelet transform: *Journal of Asian Earth Sciences*, 147, 358-377.
- Nelson, P.H., and G.D. Van Voorhis, 1983, Estimation of sulfide content from induced polarization data: *Geophysics*, 48, 1, 62-75.
- Nocedal J., Wright, S. J., 2006, Numerical Optimization, Second Edition: Springer.
- Oldenburg, D. W., and R. G. Ellis, 1991, Inversion of Geophysical Data Using an Approximate Inverse Mapping: *Geophysical Journal International*, 105, 2, 325-353.

- Oldenburg, D.W., and Y. Li, 1994, Inversion of induced polarization data: *Geophysics*, 59, 1327-1341.
- Oldenburg, D.W., Y. Li, and R. G. Ellis, 1997, Inversion of geophysical data over a copper-gold porphyry deposit: A case history for Mt. Milligan: *Geophysics*, 62, 1419-1431.
- Oldenburg, D.W., Y. Li, and R. G. Ellis, 1997, Inversion of geophysical data over a copper-gold porphyry deposit: A case history for Mt. Milligan: *Geophysics*, 62, 5, 1419-1431.
- Paasche, H., and J. Tronicke, 2007, Cooperative inversion of 2D geophysical data sets: A zonal approach based on fuzzy c - means cluster analysis: *Geophysics*, 72, 3, A35-A39.
- Pirajno, F., 2009, *Hydrothermal Processes and Mineral Systems*: Springer.
- Portniaguine, O., and M. S., Zhdanov, 2002, 3-D magnetic inversion with data compression and image focusing: *Geophysics*, 67, 5, 1532-1541.
- Pressacco, R., 2012, Initial resource estimate for the Newton project, central British Columbia, Canada: Technical Report, NI43-101.
- Rosenblatt F., 1962, *Principles of neurodynamics: Perceptrons and the theory of brain mechanisms*, Washington: Spartan Books.
- Shapiro, A., 2002, The merging of neural networks, fuzzy logic, and genetic algorithms, *Insurance: Mathematics and Economics*, 31, 1, 115-131.
- Shives, R.B.K., P.B., Holman and L. Rebolledo, 1995, Airborne geophysical survey, Fish Lake, British Columbia: Geological Survey of Canada, Open File 2800. <http://www.empr.gov.bc.ca/MINING/GEOSCIENCE/PUBLICATIONSCATALOGUE/OPENFILES/2005/Pages/2005-10.aspx>.
- Siddique, N., Adeli, H., 2013, *Computational Intelligence: Synergies of Fuzzy Logic: Neural Networks and Evolutionary Computing*: Wiley.
- Sillitoe, R. H., 2010, Porphyry copper systems: *Economic Geology*, 105, 1, 3-41.
- Sillitoe, R.H., 2015, Epithermal paleosurfaces: *Mineralium Deposita*, 50, 7, 767-793.

- Sillitoe, R.H., J.W., Hedenquist, 2003, Linkages between volcanotectonic settings, ore-fluid compositions, and epithermal precious metal deposits: Special Publication-Society of Economic Geologists, 10, 315-343.
- Simmons, S.F., N.C., White., D. A., John, 2005, Geological characteristics of epithermal precious and base metal deposits. In: Hedenquist, J.W., Thompson, J.F.H., Goldfarb, R.J., Richards, J.P. (Eds.), 100th Anniversary Volume: Economic Geology, Society of Economic Geologists, 485-522.
- Sinha, S., P.S., Routh, P.D., Anno, J.P., Castagna, 2005, Spectral decomposition of seismic data with continuous-wavelet transform: Geophysics, 70, 6, P19-P25.
- Srinivas, N., and K., Deb, 1995, Multiobjective optimization using nondominated sorting in genetic algorithms: Evolutionary Computation, 2, 30, 221-248.
- Sumner, J. S., 1976, Principles of induced polarization for geophysical prospecting: Elsevier.
- Tahmasebi, P., Hezarkhani, A., 2012, A hybrid neural networks-fuzzy logic-genetic algorithm for grade estimation: Computers & Geosciences, 42, 18-27.
- Taylor, B.E., 2007, Epithermal gold deposits: Mineral Deposits of Canada: A Synthesis of Major Deposit-Types, District Metallogeny, the Evolution of Geological Provinces, and Exploration Methods: Geological Association of Canada, Mineral Deposits Division, Special Publication, 5, 113-139.
- Trauth, M.H., 2015, MATLAB® Recipes for Earth Sciences, Fourth Edition: Springer.
- Tsuzuki, M., Martins, T.C., 2014, Simulated Annealing: Strategies, Potential Uses and Advantages: Nova Science Pub Inc.
- Van Coillie, F.M.B., L.P.C., Verbeke, R.R., De Wulf, 2007, Feature selection by genetic algorithms in object-based classification of IKONOS imagery for forest mapping in Flanders, Belgium: Remote Sensing of Environment, 110, 476-487.
- Van der Baan, M., 2006, PP/PS Wavefield separation by independent component analysis: Geophys. J. Int., 166, 339-348.
- Von der Malsburg, C. and W., Schneider, 1986, A neural cocktail-party processor: Biol. Cybern. 54, 29-40.

- Weng, H.Y., and K.M., Lau, 1994, Wavelet, period-doubling and time-frequency localization with application to satellite data analysis: *J. Atmos. Sci.*, 51, 2523-2541.
- Wisén, R., and A. V. Christiansen, 2005, Laterally and mutually constrained inversion of surface wave seismic data and resistivity data: *J. Environ. Eng. Geophys.*, 10, 3, 251-262.
- Xu, Q., Chen, Q., Li, W., 2011, Application of genetic programming to modeling pipe failures in water distribution systems: *J Hydroinformatics*, 13, 3, 419-428.
- Zhang, G.P., 2007, Avoiding Pitfalls in Neural Network Research: *Systems, Man and Cybernetics*, 37, 1, 3-16.
- Zhao, Z.A., H., Liu, 2011, *Spectral Feature Selection for Data Mining*: CRC Press.
- Zou, W., Y., Li, K. C., Lo and Z., Chi, 2006, Improvement of image classification with Wavelet and Independent Component Analysis (ICA) based on Structured Neural Networks, *IEEE: International Conference on Neural Networks*, 3949-3954.